

December 2013

Superhydrophobicity and Underwater Superoleophobicity of Oxidized Surfaces of Some Copper Alloys

Aniedi Effiong Nyong
University of Wisconsin-Milwaukee

Follow this and additional works at: <https://dc.uwm.edu/etd>

 Part of the [Engineering Commons](#)

Recommended Citation

Nyong, Aniedi Effiong, "Superhydrophobicity and Underwater Superoleophobicity of Oxidized Surfaces of Some Copper Alloys" (2013). *Theses and Dissertations*. 741.
<https://dc.uwm.edu/etd/741>

This Dissertation is brought to you for free and open access by UWM Digital Commons. It has been accepted for inclusion in Theses and Dissertations by an authorized administrator of UWM Digital Commons. For more information, please contact open-access@uwm.edu.

SUPERHYDROPHOBICITY AND UNDERWATER SUPEROLEOPHOBICITY OF
OXIDIZED SURFACES OF SOME COPPER ALLOYS

by

Aniedi E. Nyong

A Dissertation Submitted in

Partial Fulfillment of the

Requirements for the Degree of

Doctor of Philosophy

in Engineering

at

The University of Wisconsin-Milwaukee

December 2013

ABSTRACT

SUPERHYDROPHOBICITY AND UNDERWATER SUPEROLEOPHOBICITY OF OXIDIZED SURFACES OF SOME COPPER ALLOYS

by

Aniedi E. Nyong

The University of Wisconsin-Milwaukee, 2013
Under the Supervision of Professor Pradeep K. Rohatgi

Thermal oxidation and chemical oxidation of C36000 and C84400 copper alloys in different oxidizing N_2 - O_2 mixtures and in different concentrations of stearic acid (STA) and arachidic acid (ARA) generated surface morphologies that affected the wetting of the copper alloys. XRD and EDX analyses of the thermally oxidized surface layers of the C36000 copper alloys confirmed the formation of ZnO and PbO with the nanowires formed consisting of ZnO in terms of the chemical composition. Equally, the XRD analyses of the oxidized surface layer of the C84400 copper alloy at the different oxidizing temperatures (550 °C and 650 °C) showed that a mixture of ZnO, PbO and CuO were formed. In the thermally oxidized C36000 copper alloy, the growth of the ZnO nanowires on the convoluted oxide layers sufficiently altered the contact angle behaviour of water as the surfaces on which the ZnO nanowires grew were anti-wetting to water. The calculated values of the f_{sl} , for the surfaces of the thermally oxidized C36000 substrates with ZnO nanowires, ranged from 0.002 to 0.004. A stable Cassie-Baxter wetting state, with contact angle up 142 ° for water, was generated due to a combination of water trapped in the convoluted oxide layer and the low f_{sl} . However, surfaces that showed high water contact angle, > 130 °, were oleophilic under water to oil drops. Superoleophobicity was achieved through a porosity driven mechanism that was

dependent on the thickness of the oxide layer in the thermally oxidized samples of the C84400 copper alloys. The measured under water oil contact angles increased with the oxide layer thickness, as the porosity of the oxide layer increased due to the irregular packing of oxide grains. At a peak oxide layer thickness of $25.69 \pm 9.14 \mu\text{m}$, oil contact angle of 154.4 ± 1.2 confirming underwater superoleophobicity was achieved. The oxide granule morphologies changed with the amount of oxygen in the oxidizing $\text{N}_2\text{-O}_2$ gas mixture used. In $\text{N}_2\text{-}0.75 \text{ wt.-% O}_2$ gas mixture, the granules were larger and showed lateral growth. However, the kinetics of the thermal oxidation processes showed that the growth of the oxide layer followed the parabolic law. A combination of the thermal oxidation and reaction of the oxide formed with STA and ARA created superhydrophobic surfaces made of varying forms of nanostructures. Superhydrophobicity was achieved with the maximum water contact angles of $150.2^\circ \pm 1.5^\circ$ and $153.8^\circ \pm 3.5^\circ$ for the C36000 as well as $150.5^\circ \pm 1.5^\circ$ and $152.9^\circ \pm 2.1^\circ$ for the C84400 copper alloys that were processed through this method. However the hierarchical rough surface degraded and the superhydrophobicity of the surfaces cease after 18 hours of the process. FT-IR and XRD of the surfaces confirmed the oxides reacted to form the stearates and arachidates of Zn, Cu and Pb. Similar anti-wetting, superhydrophobic behaviour was achieved through the direct chemical oxidation process in different concentrations of STA and in 0.005M ARA at 30 °C and 40 °C process temperature. The nano-features formed at 40 °C were thicker than those at 30 °C. The XRD studies on the sample surfaces after 5 days of chemical oxidation in 0.005M STA confirmed the formation of zinc stearate and zinc arachidate superhydrophobic coatings.

© Copyright by Aniedi Nyong, 2013
All rights reserved

I dedicate this research work firstly to the Almighty God who makes all things possible in His own time. And secondly to his Excellency, Obong Victor Attah - the Governor of Akwa Ibom State, Nigeria [1999-2007] - for awarding me a post graduate scholarship

TABLE OF CONTENTS

Chapter	Page
1	Introduction..... 1
1.0	Definition of self cleaning and anti-wetting surfaces 1
1.1	Concepts and theories of lotus effect in self cleaning materials 3
1.2	The Wenzel and Cassie-Baxter models 4
1.2.1	The Wenzel model 4
1.2.1	The Cassie-Baxter model 5
1.3	Thermal oxidation and the formation of metal oxide nanostructures 7
1.4	Thermal Oxidation: Thermodynamic considerations 9
1.5	Chemical Oxidation Process 11
2	Research Objectives 14
3	Literature Review..... 16
4	Materials and Method 25
4.1	Materials 25
4.2	Research Methods 29
4.2.1	Thermal Oxidation method 29
4.2.2	Chemical oxidation method 30
4.2.3	Thermo-chemical reaction method 31
4.2.4	Combination of mechanical abrasion and chemical oxidation 31
4.3	Surface characterization methods 32
5	Underwater oleophobic behavior and wetting transition on mechanically abraded surfaces of C36000 and C84400 copper alloys 35
5.0	Introduction 35
5.1	Characterization of mechanically abraded surfaces of C36000 and C84400 copper alloys 35
5.1.1	Surface morphology study of the mechanically abrades surfaces of C36000 and C84400 copper alloys 35
5.2	Surface roughness and underwater oil contact angle evaluation and wetting transition 37
6	Wetting behavior of water on thermally oxidized surfaces of C36000 copper alloys 46
6.0	Introduction 46
6.1	Experiment 47
6.2	Characterization 48
6.3	Results and discussion 48
6.3.1	Identification of phases on the surfaces of the oxidized samples of C36000 copper alloy 49

6.3.2	Surface morphology examination with the scanning electron microscope	51
6.3.2a	Surface morphology of oxide layer after thermal oxidation at 550° C and 650° C in air	51
6.3.2b	Surface morphology of oxide layer after thermal oxidation at 550° C and 650° C in N ₂ -0.75 Wt. % O ₂ , N ₂ -5 Wt. % O ₂ and N ₂ -12 Wt% O ₂ gas mixtures.....	52
6.4	Chemical composition of the oxide nanowires.....	57
6.5	Mechanism of growth of ZnO nanowires and the oxide layer.....	58
6.6	Water Contact angle and surface roughness evaluation	64
7	Superoleophobic behavior of thermally oxidized surfaces of C844000 copper alloy.....	73
7.0	Introduction.....	73
7.1	Experiment.....	74
7.2	Characterization	75
7.3	Result and Discussion	76
7.3.1	Surface morphology evaluation with the scanning electron microscope	76
7.3.2	Oxide layer thickness and mechanism of growth	81
7.3.3	Phase identification of the oxides on the surfaces of the thermally oxidized C84400 copper alloy	85
7.4	Underwater oil contact angle and surfaces roughness evaluation	88
8	Superhydrophobicity of C36000 and C84400 generated by the Thermo-chemical treatment with stearic and arachidic acids.....	96
8.0	Introduction.....	96
8.1	Experimental approach	96
8.1.1	Materials	96
8.1.2	Preparation of superhydrophobic surface	96
8.1.3	Surface characterization.....	97
8.2	Results and discussion	98
8.2.1	Surface morphology characterization using the Scanning electron microscope	98
8.2.2	Chemical Composition of superhydrophobic surfaces formed by the thermo-chemical treatment of C36000 and C84400 copper alloys	102
8.2.2 i	Energy Dispersive X-ray analysis.....	102
8.2.2 ii	Infra-red spectroscopic analysis of surface of samples	104
8.2.2 ii a	FT-IR spectroscopic analysis of thermo-chemically treated (12hrs) C36000 sample in 0.005M STA	104
8.2.2 ii b	FT-IR spectroscopic analysis of thermo-chemically treated (12hrs) C84400 sample in 0-005M STA	105
8.2.2 ii c	FT-IR spectroscopic analysis of thermo-chemically treated (12hrs) C36000 sample in 0.005M ARA	106

8.2.2 ii d	FT-IR spectroscopic analysis of thermo-chemically treated (12hrs) C84400 sample in 0.005M ARA	106
8.2.2 iii a	X-ray diffraction studies of the thermally oxidized C36000 copper alloy treated with 0.005M STA in a thermo-chemical process	108
8.2.2 iii b	X-ray diffraction studies of the thermally oxidized C84000 copper alloy treated with 0.005M STA in a thermo-chemical process	111
8.2.2 iii c	X-ray diffraction studies of the thermally oxidized C36000 copper alloy treated with 0.005M STA in a thermo-chemical process	113
8.2.2 iii d	X-ray diffraction analysis of thermally oxidized C84400 copper alloy treated with 0.005M ARA in a thermo-chemical process.....	114
8.3	Contact angle of water and surface roughness evaluation	116
9	Superhydrophobicity of C36000 and C84400 copper alloys by direct chemical oxidation using stearic and arachidic acids.....	121
9.0	Introduction.....	121
9.1	Experimental.....	121
9.1.1	Materials	121
9.1.2	Method.....	121
9.2	Characterization	122
9.3	Result and discussion.....	122
9.3.1	Characterization of surface morphology of the C36000 and C84400 copper alloys directly oxidized in STA at room temperature and in ARA at 30 °C and at 40 °C	122
9.3.1 a	Surface morphologies of samples treated in 0.005M STA at room temperature	122
9.3.1 b	Surface morphologies of samples treated in 0.005M ARA at 30 °C and at 40 °C	125
9.4	Energy Dispersive X-ray analysis of the surfaces	128
9.5	X-ray diffraction analysis of chemically oxidized C36000 treated with 0.005M STA and ARA	129
9.6	Contact angle of water on C36000 and C84400 copper alloys after chemical oxidation in different concentrations of STA and in ARA at different temperatures	131
10	Conclusion	143
	References.....	148
	Appendices.....	155

LIST OF FIGURES

Figure		Page
1	Contact angle for Young's equation.	3
2	Wenzel model	4
3	Cassie-Baxter model	5
4	Carboxylic acid structure	11
5	Thermal oxidation furnace.....	28
6	Electric furnace	28
7	Parr Pressure reaction apparatus, model 4601Q	28
8	Taylor Hobson 2-D precision profilometer.....	32
9	Rame Hart 250 model goniometer	33
10	S-4800 Hitachi scanning electron microscope.....	34
11	Atomic Force Microscope (AFM)	34
12	Surface morphology and contact angles of oil on mechanically abraded surfaces of C36000 copper alloy.....	36
13	Surface morphology and contact angles of oil on mechanically abraded surfaces of C84400 copper alloy.....	36
14	Plot of underwater oil contact angle against time of mechanical abrasion under varied applied forces	40-41
15	Graph of wetting regimes of oil drop on C84400 copper alloy surface in air and water and water drop on C84400 surface in air	42
16	Graph of wetting regimes of oil drop on C36000 copper alloy surface in air and water and water drop on C36000 surface in air	42
17	Contact angle of oil under water on mechanically abraded surfaces of C36000 and C84400 copper alloys showing the Cassie-Baxter and Wenzel wetting regimes as a function of average surface roughness, R_a	45
18	Optical and SEM micrographs of the microstructure of C36000 copper alloy ...	46
19	EDX spectrum and elemental map showing percentage and distribution of the alloying elements in the microstructure of C36000 copper alloy sample	47

20	X-ray diffraction pattern of C36000 copper alloy thermally oxidized in N ₂ -0.75 Wt. % O ₂	49
21	X-ray diffraction pattern of C36000 copper alloy thermally oxidized in N ₂ -5 Wt. % O ₂	50
22	X-ray diffraction pattern of C36000 copper alloy thermally oxidized in N ₂ -12 Wt. % O ₂	50
23	Figure [23]: SEM of thermally oxidized C36000 for 4hours at 550 °C and 650 °C in air. [a and b] 550 °C [c and d] 650 C°	52
24	SEM images of thermally oxidized samples in N ₂ -0.75 Wt. % O ₂ showing oxide layer convolution and ZnO nanowire growth at 650 °C. (1) SEM for 1 hour in N ₂ -0.75 Wt. % O ₂ (2) SEM for 2 hours in N ₂ -0.75 Wt. % O ₂ (3) SEM for 3 hours in N ₂ -0.75 Wt. % O ₂ . Images 1, 2, 3 are at 10 000x and 1a, 2a, 3a are at 50 000x.....	54
25	SEM images of thermally oxidized samples in N ₂ -5 Wt. % O ₂ showing oxide layer convolution and ZnO nanowire growth at 650 °C. (1) SEM for 1 hour in N ₂ -5 Wt. % O ₂ (2) SEM for 2 hours in N ₂ -5 Wt. % O ₂ (3) SEM for 3 hours in N ₂ -12 Wt. % O ₂ . Images 1, 2, 3 are at 10 000x and 1a, 2a, 3a are at 50 000x.....	55
26	SEM images of thermally oxidized C36000 copper alloy samples in N ₂ -12Wt. %O ₂ showing oxide layer convolution and ZnO nanowire growth at 650 °C (1) SEM for 1 hour in N ₂ -12 Wt. % O ₂ (2) SEM for 2 hours in N ₂ -12 Wt. % O ₂ . (3) SEM for 3 hours in N ₂ -12 Wt. % O ₂ . Images 1, 2, 3 are at 10 000x and 1a, 2a, 3a are at 50 000x	56
27	EDX spectrum showing the chemical composition of oxide nanowire	58
28	A cross-section showing the thickness of the oxide layer (a) 1 hour in N ₂ -0.75 wt.% O ₂ (b) 2 hours in N ₂ -0.75 wt. % O ₂ (c) 3 hours in N ₂ -0.75 wt. % O ₂ (d) 1 hours in N ₂ -5 wt. % O ₂ (e) 2 hours in N ₂ -5 wt. % O ₂ (f) 3 hours in N ₂ -5 wt. % O ₂ . (g) 1 hour in N ₂ -12 wt. % O ₂ (h) 2 hours in N ₂ -12 wt. % O ₂ (i) 3 hours in N ₂ -12 wt. % O ₂ (j) 1 hour in air (k) 2 hours in air (l) 3 hours in air.	60
29	Plot of the oxide layer thickness against the square root of the oxidation time. 61	
30	Plot of the contact angle of water and oil after thermal oxidation in air at 450 C and 550 C	65

31	ZnO nanowire growing from a plane of projection of an oxide layer	68
32	Plot of cosine of the contact angle of water as a function of the thermal oxidation time.....	70
33	Plot of cosine of the contact angle of oil as a function of the thermal oxidation time.....	71
34	Optical (a) and SEM (b) micrographs of the microstructure of C84400 copper alloy.....	73
35	Energy dispersive plot (a) and the elemental mapping (b) of the microstructure of C84400 copper alloy showing elemental composition and distribution.....	74
36	Set-up for the measurement of oil drop contact angle underwater	75
37	SEM images of thermally oxidized C84400 in N ₂ -0.75 Wt. % O ₂ for 1 hour at 650 °C. Insert is oil contact angles under water.....	77
38	SEM images of thermally oxidized C84400 copper alloy in N ₂ -0.75 Wt. % O ₂ for 2 hours at 650 °C. Insert is oil contact angles under water	78
39	SEM images of thermally oxidized C84400 copper alloy in N ₂ -0.75 Wt. % O ₂ for 3 hours at 650 °C. Insert is oil contact angles under water	78
40	SEM images of thermally oxidized C84400 copper alloy in different oxidizing atmospheres viz: a, b, c in N ₂ -5 Wt. % O ₂ at 650 °C. Insert is oil contact angles under water.....	79
41	SEM images of thermally oxidized C84400 copper alloy in different oxidizing atmospheres viz: a, b, c in N ₂ -12 Wt. % O ₂ at 650 °C. Insert is oil contact angles under water.....	79
42	SEM images of thermally oxidized C84400 in different oxidizing atmospheres viz: a, b, c in air at 650 °C. Insert is oil contact angles under water	79
43	Plot of granule size of oxide against the -Log. of the weight fraction of oxygen used in the thermal oxidation of C84400 copper alloys.....	80
44	SEM of cross-sectional thickness of oxide layers on the thermally oxidized C84400 copper alloy at 650 °C viz: a, b, c in N ₂ -0.75 Wt. % O ₂	81
45	SEM of cross-sectional thickness of oxide layers on the thermally oxidized C84400 at 650 °C viz: a, b, c in N ₂ -5 Wt. % O ₂	82

46	SEM of cross-sectional thickness of oxide layers on the thermally oxidized C84400 copper alloy at 650 °C viz: a, b, c in N ₂ -12Wt. % O ₂	82
47	SEM of cross-sectional thickness of oxide layers on the thermally oxidized C84400 copper alloy at 650 °C viz: a, b, c in air	82
48	Parabolic plots for the determination of the rate constant, K _p , for the thermal oxidation of C84400 copper alloy samples in (a) N ₂ -0.75 Wt. % O ₂ (b) N ₂ -5 Wt. % O ₂ (C) N ₂ -12Wt. % O ₂ (d) air	84
49	Plot of the oxide layer thickness against the time for thermal oxidation.....	86
50	X-ray diffraction pattern of oxidized C84400 copper alloy in air at 550°C	86
51	X-ray diffraction pattern of oxidized C84400 copper alloy in air at 650°C	87
52	X-ray diffraction pattern of oxidized C84400 copper alloy in N ₂ -0.75 Wt. % O ₂ , N ₂ -5 Wt. % O ₂ and N ₂ -12 Wt. % O ₂ oxidizing gas mixtures at 550 °C and 650 °C	87
53	The variation of the average surface roughness with the thermal oxidation time at 650 °C	87
54	Processed surface images of thermally oxidized C84400 copper alloy thermally oxidized in N ₂ -5Wt. % O ₂ at 650 °C (a. 1 hour, b. 2hours. c. 3hours)	91
55	Processed surface images of thermally oxidized C84400 copper alloy thermally oxidized in N ₂ -12Wt. % O ₂ at 650 °C (a. 1 hour, b. 2hours. c. 3hours).	92
56	Plot of the oxide layer thickness and the estimated pore volume against the oxidation time (hours)	93
57	Plot of the underwater oil contact angle against the oxidation time (hours)	94
58	Plot of the underwater oil contact angle and the estimated pore volume against the oxidation time	95
59	Polished and thermally oxidized surfaces C36000 copper alloy after thermal oxidation in air for 4 hours (insert is the contact angle of water on the surface)	96
60	Polished and thermally oxidized surfaces C84400 copper alloy after thermal oxidation in air for 4 hours (insert is the contact angle of water on the surface)	99
61	SEM images of C36000 and C84400 after thermo-chemical modification in 0.005M STA; (a) C36000 after 6 hours thermo-chemical modification (b)	

	C36000 after 12 hours thermo-chemical modification (d) C84400 after 6 hours thermo-chemical modification (e) C84400 after 12 hours thermo-chemical modification (f) C84400 after 18 hours of thermo-chemical modification	100
62	SEM images of C36000 and C84400 after thermo-chemical modification in 0.005M ARA; (a) C36000 after 6 hours thermo-chemical modification (b) C36000 after 12 hours thermo-chemical modification (c) C36000 after 18 hours thermo-chemical modification (d) C84400 after 6 hours thermo-chemical modification (e) C84400 after 12 hours thermo-chemical modification (f) C84400 after 18 hours of thermo-chemical modification	101
63	EDX elemental mapping and surface composition of thermally oxidized C36000 copper alloy after reaction with 0.005M STA for 12 hours.....	102
64	EDX elemental mapping and surface composition of thermally oxidized C84400 copper alloy after reaction with 0.005M STA for 12 hours.....	103
65	EDX elemental mapping and surface composition of thermally oxidized C84400 copper alloy after reaction with 0.005M ARA for 12 hours.....	103
66	FT-IR spectrum of thermally oxidized C36000 after reaction with 0.005M STA for 12 hours	105
67	FT-IR spectrum of thermally oxidized C84400 after reaction with 0.005M STA for 12 hours.....	106
68	FT-IR spectrum of thermally oxidized C36000 after reaction with 0.005M ARA for 12 hours	106
69	FT-IR spectrum of thermally oxidized C84400 after reaction with 0.005M ARA for 12 hours.....	107
70	X-ray diffraction pattern of C36000 brass sample after thermal oxidation in air for 4 hours	108
71	X-ray diffraction pattern of zinc stearate powder and superhydrophobic C36000 Brass sample surface after its reaction with stearic acid for 2θ angles between 18° and 60°	110
72	X-ray diffraction pattern of superhydrophobic C36000 Brass sample surface after reaction with stearic acid and zinc stearate for 2θ angles between 2.5° and 18°	111
73	X-ray diffraction pattern of superhydrophobic C84400 Brass sample surface after reaction with stearic acid for 2θ angles between 2° and 18°	111

74	X-ray diffraction pattern of superhydrophobic C84400 Brass sample surface after reaction with stearic acid at 2Θ angles between 18° and 70°	111
75	X-ray diffraction pattern of superhydrophobic C36000 Brass sample surface after reaction with arachidic acid at 2Θ angles between 2° and 18°	113
76	X-ray diffraction pattern of superhydrophobic C36000 Brass sample surface after reaction with arachidic acid at 2Θ angles between 18° and 60°	114
77	X-ray diffraction pattern of superhydrophobic C84400 Brass sample surface after reaction with arachidic acid at 2Θ angles between 2.5° and 20°	115
78	X-ray diffraction pattern of superhydrophobic C84400 Brass sample surface after reaction with arachidic acid at 2Θ angles between 18° and 60°	115
79	Plot average surface roughness of copper alloy samples polished, thermally oxidized and reacted with (a) 0.005M STA and (b) 0.005M ARA with time	119
80	Plot of $\cos \Theta$ against the fractional surface area (f_{sw}) of contact with water drop	120
81	SEM images of C36000 after chemical oxidative surface modification in 0.005M STA at room temp. 1, 2, 3, 4, 5- for 1-5 days in 0.005M STA	120
82	SEM images of C84400 after chemical oxidative surface modification in 0.005M STA at room temp. 1, 2, 3, 4, 5- for 1-5 days in 0.005M STA	124
83	SEM of C36000 copper alloy after chemical oxidative surface modification in 0.005M ARA at 30°C . 1, 2, 3, 4, 5- for 1-5 days in 0.005M ARA.....	124
84	SEM of C84400 copper alloy after chemical oxidative surface modification in 0.005M ARA at 30°C . 1, 2, 3, 4, 5- for 1-5 days in 0.005M ARA.....	126
85	SEM images of C36000 copper alloy after chemical oxidative surface modification in 0.005M ARA at 40°C . 1, 2, 3, 4, 5- for 1-5 days in 0.005M ARA	127
86	SEM images of C84400 after chemical oxidative surface modification in 0.005M ARA AT 40°C . 1, 2, 3, 4, 5- after 1-5 days in 0.005M ARA	127
87	Elemental composition of surfaces of (1) C36000 copper alloy oxidized in 0.005M STA for 5 days (2) C84400 copper alloy chemically oxidized in 0.005M	

	STA for 5 days (3) C36000 copper alloy oxidized in 0.005M ARA for 5 days (4) C84400 copper alloy chemically oxidized in 0.005M STA for 5 days (3) C36000 copper alloy oxidized in 0.005M ARA for 5 days.....	128
88	X-ray diffraction pattern of C36000 and C84400 copper alloys after treatment in 0.005M STA for 5 days	129
89	X-ray diffraction pattern of C36000 and C84400 copper alloy after treatment in 0.005M ARA for 5 days at 40 °C	130
90	Plot showing the relationship of contact angle of water with time on C36000 copper alloy treated in various concentrations of STA at room temperature	133
91	Plot showing the relationship of contact angle of water with time on C84400 copper alloy treated in various concentrations of STA at room temperature	133
92	Plot showing the relationship of contact angle of water with time in various concentrations of STA [1] C36000 in 0.005M ARA at 30 °C and 40 °C [2] C84400 in 0.005M ARA at 30 °C and at 40 °C.....	136
93	Plot of the variation of Ds with the time of chemical oxidation of copper alloys in 0.005M ARA.....	137

LIST OF TABLES

Table		Page
1	Table for the chemical composition of C36000 copper alloys	25
2	Table for the chemical composition of C84400 copper alloys.....	25
3	Grit size and average diameter of SiC paper used in mechanical abrasion of samples	37
4	Underwater oil contact angles on mechanically abraded surfaces of C36000 and C84400 copper alloys	37
5	Underwater oil contact angle on C36000 and C84400 mechanically abraded with 50 grit SiC paper under controlled applied force and time	38
6	Underwater oil contact angle on C36000 and C84400 mechanically abraded With 180 grit SiC paper under controlled applied force and time	38
7	Underwater oil contact angle on C36000 and C84400 mechanically abraded with 320 grit SiC paper under controlled applied force and time	39
8	Table of the slope of contact angle of oil in underwater condition as a function of the applied force, F_a and time (minutes.) during mechanical abrasion with different grit sizes of SiC paper	40
9	Elemental composition of C36000 copper alloy from EDX analysis	47
10	Dimensions of thickness of oxide layer of C36000 thermally oxidized in N_2 -5 Wt. % O_2 and N_2 -12 Wt. % O_2 and air at $650^\circ C$	61
11	Dimensions of ZnO nanowires grown on the surfaces of C36000 thermally oxidized in N_2 -0.75 Wt. % O_2 , N_2 -5 Wt. % O_2 and N_2 -12 Wt% O_2 at $650^\circ C$	63
12	Contact angles of water on thermally oxidized surfaces of C36000 in air at $450^\circ C$, $550^\circ C$ and $650^\circ C$	64
13	Contact angles of water on thermally oxidized surfaces of C36000 in N_2 - 0.75 Wt. % O_2 gas mixtures at $550^\circ C$ and $650^\circ C$	64

14	Contact angles of water on thermally oxidized surfaces of C36000 in N ₂ -5 Wt. % O ₂ gas mixtures at 550 °C and 650 °C.....	64
15	Contact angles of water on thermally oxidized surfaces of C36000 in N ₂ -12 Wt. % O ₂ gas mixtures at 550 °C and 650 °C.....	65
16	f _{sl} , aspect ratio and Ra of C36000 thermally oxidized in N ₂ -5wt % O ₂ and N ₂ -12 Wt. % O ₂ at 650 °C	67
17	Elemental composition of C84400 copper alloy	74
18	Measured sizes of oxides grains on surfaces of thermally oxidized C84400 copper alloy.....	80
19	Oxide layer thickness due to the thermal oxidation of C84400 copper alloy in the different Nitrogen-oxygen gas mixtures	83
20	Rate constants for the formation of the oxide layer using the Parabolic law	84
21	Average surface roughness and underwater oil contact angle on surfaces of C84400 copper alloy thermally oxidized at 550 °C	89
22	Average surface roughness, R _a ; fractional surface area wetted by oil, f _{so} and the average contact angle of oil underwater, Θ _{av}	90
23	Oxide layer thickness, λ; pore size, D and estimated pore volume of C84400 copper alloy samples oxidized in N ₂ -5Wt. % O ₂ and N ₂ -12Wt. % O ₂ gas mixtures	93
24	Elemental composition of surfaces of thermally oxidized C36000 and C84400 copper alloys after reactions with 0.005M STA	104
25	Elemental composition of surfaces of thermally oxidized C36000 and C84400 copper alloys after reactions with 0.005M ARA	104
26	Table of the average surface roughness, R _a and contact angle of water on C36000 and C84400 copper alloys that have been polished, thermally oxidized and chemically reacted with 0.005M STA and 0.005 ARA.....	117
27	Size distribution and calculated fractional surface area for wetting of surface with water drops.....	120
28	Contact angles of water on copper alloys immersed in 0.005M STA for different time duration	132
29	Contact angles of water on copper alloys immersed in 0.010M STA for different	

	time duration	133
30	Contact angles of water on copper alloys immersed in 0.015M STA for different time duration	133
31	Contact angles of water on copper alloys immersed in 0.005M ARA for different time duration at 30 °C	135
32	Contact angles of water on copper alloys immersed in 0.005M ARA for different time duration at 40 °C	136
33	Contact angles of water on abraded Copper alloys immersed in 0.015M STA for different time durations.....	136

List of symbols

Θ_{ow}	Contact angle of oil under water
Θ_{aw}	Water contact angle in air
Θ_{oa}	Oil contact angle in air
R_a	Average surface roughness
Θ_{CB}	Cassie-Baxter contact angle
Θ_w	Wenzel contact angle
f_1	Fraction of solid (in Cassie-Baxter equation)
f_2	Fraction of air (in Cassie-Baxter equation)
Θ_{cr}	Critical intrinsic contact angle
f_{sl}	Fractional surface area in contact with liquid
f_{so}	Fractional surface area in contact with oil
V_p	Estimated pore volume
λ	Oxide layer thickness
D	Estimated pore size

ACKNOWLEDGEMENTS

In the course of doing this research I have had cause to interact with a lot of people whose goodwill, help, advice and directives have been very helpful. It is in this regards that I want to acknowledge my research advisor, the indefatigable Professor Pradeep Rohatgi, who has been pivotal to the completion of this work. I will not fail to mention Dr JB Ferguson and Dr Ben Schultz. These two Gentlemen were always willing to answer my questions, give advice and comment on my work at various times. At this point, I need to recognize Professor Michael Nosonovsky, a leading light in the area of self- cleaning materials and biomimetics. His insights and suggestions have been quite helpful.

Also worth acknowledging are members of my family that have always stood by me in all my endeavours. They include my late father, Elder E.T. Nyong; my mother, Mrs I. E. Nyong; my sisters, Nneka and Idongesit; my brother in-law, Mr. I. F. Ekpo and my wife, Mfoniso. In the course of my studies I have had friends and colleagues whose encouragement added value to the research. As such, I am grateful to such friends and colleagues like Pemba, Beyauna, Chiso, Afsaneh, Emad, Meysam, Shobit and Professor Emmanuel Worniyoh. I indeed owe all of you a world of gratitude and for this I say thank you.

CHAPTER ONE

INTRODUCTION

1.0 Definition of self-cleaning and anti-wetting surfaces:

A lot of attention has been given to self-cleaning and anti-wetting materials in the last few decades. The concept of self-cleaning was first thought of by Wilhelm Barloff after observing the water repellency of the lotus plant, *Nelumbo nucifera*¹. Barloff observed that water rolled off on the lotus leaf without sticking and therefore carried off the dirt on the surface of the leaf. It is this ability of the lotus leaf that is described as self-cleaning and the materials that exhibit this property are known as self-cleaning materials.

This high water repellency is also often referred to as the lotus effect². This term has also been extended to surfaces that are artificial and are exhibiting water repellency. In terms of contact angles of water on such a surface, the angle of 150° or greater characterizes a superhydrophobic, self-cleaning surface exhibiting the lotus effect³.

Lotus effect as applied in self-cleaning materials has a lot of importance in terms of the practical applications they can be put to. Already, several products exist now which uses the lotus effect as the basis. Some of these products include fabrics that are water and stain repellent as well as self cleaning paints and panels.

Due to such importance, there has been intense research into production of self-cleaning surfaces in materials and most of these research procedures involved expensive multistep reagents and equipments and are sometimes only applicable to specific materials⁴.

Some of the methods that have been used in producing self cleaning surfaces on materials are lithography, etching, deformation, deposition and transfer methods⁵.

[i] Lithography: Lithography is a very well-known method used for creating large area of periodic micro/nanopatterns. This method includes photo, e-beam, x-ray and soft lithography⁶. This method has been applied extensively in patterning wafers to create various micro and nanopatterns for superhydrophobic and self-cleaning behavior.

[ii] Etching: The etching technique is an effective method of making surface roughness and includes approaches such as plasma etching, laser etching, chemical etching and electrochemical etching⁷. The etching technique is a fast technique though the control of the process is poor and the possibility of chemical contamination is high.

[iii] Deposition: The deposition technique is equally aimed at increasing surface roughness and reducing the surface energy by depositing materials. The methods of deposition include the following: adsorption, dip coating, electro-spinning, anodization, electrochemical, evaporation, chemical vapour deposition and plasma deposition.

[iv] Transfer: The transfer method includes casting and nano-imprinting methods. This method of transfer is quite close to the lithographic technique. Polymethylsiloxane [PDMS] is often used to copy or transfer small patterns due to its flow characteristics and ease of mold removal. The technique is known as nano-imprinting⁸. However, it is still a challenge to transfer natural superhydrophobic features less than 5nm using this method⁹. The lotus effect and self-cleaning behaviour of most materials found in nature are related to the topology of the surface¹⁰. Scanning electron microscopic studies of self-cleaning biological surfaces have revealed large microstructural diversity of such surfaces. A lot of these surfaces minimize the contact area with anything that comes in

contact with them. Beyond the roughness, the presence of waxy surface cell in these materials equally advances self-cleaning behavior.

Based on the above, two main requirements for a self-cleaning surface are that the surface should be rough and should have low energy. These are the two main factors that form the basis of producing a self-cleaning surface.

1.1 Concepts and theories of lotus effect in self-cleaning materials:

The hydrophobicity of a surface of a material can be determined by the measurement of the contact angle of a small droplet of fluid on a leveled surface ¹¹. The contact angle therefore is a representation of how repellent the surface is to water and other fluids such as oils.

The Young's equation, stated in equation 1, expresses the contact angle value with surface property of interfacial energy and serves as the fundamental equation for relating the contact angle of fluids to the surface property. The Young's equation, for a flat surface, as represented in figure 1 is expressed as:

$$\cos \theta_c = (\gamma_{sg} - \gamma_{sl}) / \gamma_{lg} \quad [1]$$

where γ_{sg} , γ_{sl} and γ_{lg} are the interfacial energies per unit area of the solid-liquid, solid-gas interface.

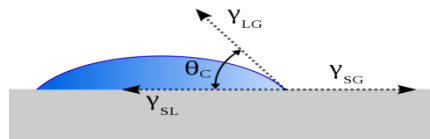


Figure 1: Contact angle for Young's equation

The Young's equation can be effectively applied to smooth and flat surfaces. This implies that for rough surfaces, there is a need for modification of the Young's equation to accommodate the roughness of the surfaces. The modification of the Young's equation to accommodate roughness and heterogeneity of the surface has resulted in the use of the Wenzel and the Cassie-Baxter models to evaluate the contact angles of liquids on surfaces.

1.2 The Wenzel and Cassie-Baxter Models:

These models attempt to explain the contact angles of fluids on surfaces that are rough and have been used extensively by various researchers.

1.2.1 The Wenzel Model:

This equation 2 relates the contact angle of a water droplet on a rough surface, Θ , with that on a smooth surface, Θ_o as shown in figure 2. The ratio of the surface area of the rough surface to that of the smooth surface is defined by a non-dimensional roughness factor, R .

$$\cos \Theta_w = (\gamma_{sg} - \gamma_{sl}) / \gamma_{lg} = R \cos \Theta_o \quad [2]$$

$$R = A_{sl} / A_f \quad [3]$$

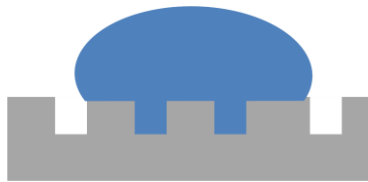


Figure 2: Wenzel model

A_{sl} is the surface area in contact with the liquid and A_f is the smooth projected surface. This model predicts that a hydrophobic surface becomes more hydrophobic with an increase in the roughness factor while a hydrophilic surface becomes more hydrophilic.

This model is applicable on the assumption that there are no air pockets trapped in the rough surface to affect the wetting.

1.2.3 The Cassie- Baxter Model:

This model, as illustrated in figure 3, describes the contact angle of a liquid, Θ , on a surface composed of solid and air (or water, for underwater contact of oils on solid surfaces). This model assumes that air trapped in the grooves of a rough surface, creates smaller liquid-solid interface.

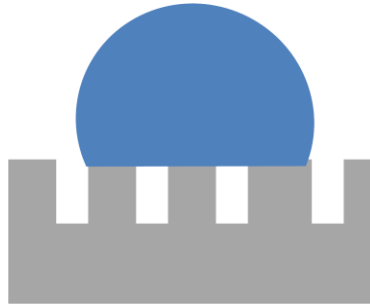


Figure 3: Cassie-Baxter model

The equation that governs the Cassie Baxter model relating to heterogeneous surfaces is given as;

$$\cos\theta_{CB} = f_1 \cos\theta_o - f_2 \quad [4]$$

Cassie and Baxter defined f_1 as the total area of solid under the drop of liquid, with θ_o as the contact angle on a smooth surface of the material. Equation 4 has been further modified by the introduction of the roughness factor, R .

$$\cos\theta_{CB} = R f_1 \cos\theta_o - f_2 \quad [5]$$

f_2 is defined in this case as the fraction of air (or water), where Θ_2 is equal to 180° . The stability criterion of the Wenzel and the Cassie-Baxter models has been established¹².

The relationship that shows the stability criterion is given as:

$$\cos\theta_{cr} = \frac{f-1}{R-f} \quad [6]$$

where θ_{cr} is the critical intrinsic contact angle. Based on [6] if $\theta > \theta_{cr}$, Cassie-Baxter mode or wetting state is favored and if $\theta < \theta_{cr}$, the Wenzel mode or wetting state is favorable instead. For a hydrophilic surface, the contact angle increases with increase in the fraction of the liquid-air interface and at high values of this interfacial fraction, surfaces become hydrophobic¹³.

Copper alloys have found wide applications and belong to the most commonly used alloys in the group of non-ferrous metals¹⁴. This long history of use of copper alloys is due to their mechanical workability, excellent electrical conductivity and ease of soldering and brazing¹⁵. Due also to their enormous use in plumbing fixtures and the like, long standing problems of fouling and corrosion abound¹⁶. It is known that bacteria, fungi, microalgae and their cellular exudates form slime layer on copper containing surfaces thereby fouling them¹⁷.

To this end, there is a need to develop self-cleaning surfaces for water transportation and plumbing. Such self-cleaning surfaces can help prevent or reduce instances of corrosion and bio-fouling of the copper alloys. The specific alloys of interest in this research have uses in plumbing as they are used for plumbing fixtures such as valves, plumbing fitting bearings and specialty parts. They include the leaded brass C36000 and the leaded semi-red brass C84400 copper alloys.

In terms of the microstructure, the C36000 is a leaded brass that exhibits a two phase microstructure containing a small quantity of the β -phase dispersed in α -matrix with some lead precipitates and inclusions. Due to the low solubility of lead in the C36000 Copper alloy, the lead is segregated and conglomerated to form inclusions in the α - β matrix in order to minimize the total free energy of the alloy. The lead content of C36000 copper alloy ranges from 2.5-3.5 per cent, which is consistent with high leaded brasses. The C36000 copper alloy has found good use in the making of valves, plumbing bearings and water pumps.

The C84400 belongs to a group of copper alloys known as the leaded semi-red brass and is also known as 81 metal or 81-3-7-9. It is one of the most common brasses used in plumbing and it contains nominally 7 per cent of lead. The microstructure of the C84400 copper alloy contains discrete lead particles primarily at the grain boundaries or interdendritic regions of the single alpha-solution, where the zinc phase of about 10 per cent, has totally dissolved in.

1.3 Thermal oxidation and the formation of metal oxide nanostructures:

Thermal oxidation is simply a reaction of a substrate with oxygen, controlled by the temperature parameter. When metals and their alloys are involved, metal oxides are formed. These oxides could be bulk or nanosize depending on the growth conditions such as temperature, time, metal catalyst and gas atmosphere¹⁸.

Varying forms of oxides have been formed from thermal oxidation and have shown unique physical and chemical properties. The oxide nanostructures could be in the form of nanowires, nanorods, nanobelts, nanosheets, nanoribbons and nanotube. These sort of

metal oxide structures are gaining attention because of the distinctive and novel properties when compared to the conventional bulk or thin film metal oxide materials ¹⁹.

The formation of oxide nanostructure is caused by the growth stresses built up during the thermal oxidation process ²⁰. The main growth stresses are known to build up from the volume differences between the formed oxide and the consumed metal in the alloy. These differences are described by the Pilling-Bedworth ratio [PBR].

The Pilling-Bedworth ratio gives the behavior of the oxide layer during the oxidation process. It can simply be described by the relationship ²¹:

$$PBR = \frac{\text{Volume of formed oxide}}{\text{volume of consumed metal}} \quad [7]$$

The following holds for the oxide layer behaviour relative to the Pilling-Bedworth Ratio (PBR):

when the PBR is less than one [PBR<1], the oxide coating layer is believed to be too thin and likely to be broken; when PBR is greater than one but less than two [1<PBR<2], a close oxide layer is formed with a certain amount of internal compressive stresses needed to set off the growth of metal oxide nanostructures on the oxide scale and PBR > 2; the oxide layer in this case will spall off.

It is expected that the oxide nanostructures such as wire, flakes and nanowalls will affect the surface roughness on a scale that is sufficient to raise the contact angle of oil and water. Equally, it should provide surface area for modification with low energy materials for superhydrophobicity and for other processes.

1.4 Thermal Oxidation: Thermodynamic considerations.

Oxidation of metal and their alloys is understood from the thermodynamic and kinetic basis of the reaction. Thermodynamics and kinetics provide the background for prediction and explanation of the products from thermal or chemical oxidation processes.

Thermodynamics is an important tool for use in predicting which species tend to oxidize during oxidation. However, the rate of the expected reactions cannot be determined from thermodynamics alone. With kinetics, the degree of oxidation reaction, which is dependent on time, area, mass transfer and the temperature; can be explained. The oxidation of a metal (Me) can be represented as follows in equation 8 ^{22, 23, 24}



The standard free energy of oxide formation, ΔG° is given as in [9]:

$$\Delta G^\circ = -RT \ln K \quad [9]$$

Here, R is the universal gas constant and T is the temperature [in Kelvin]. K is the equilibrium constant for any reversible reaction at equilibrium and is the ratio of the activities of the products to the reactants. The specific case of the reaction, as shown in equation 8 can be stated in terms of the activities of the reacting species as stated in equation 10;

$$K = a_{\text{MeO}}/a_{\text{Me}} \times 1/a_{\text{O}_2}^{1/2} = a_{\text{MeO}} / a_{\text{Me}} \times (\text{P}_{\text{O}_2}/\text{P}_\text{O})^{-1/2} \quad [10]$$

Since the metals and the oxides that are formed during the oxidation are solids and are in their standard states at atmospheric pressure, their activities are assumed to be one.

Hence, equation 10 can be stated alternatively as

$$K = 1/P_{O_2}^{1/2} \quad [11]$$

where P_{O_2} is the partial pressure of oxygen in the oxidation process. Thus, the oxidation of metals is related to the temperature and pressure of the oxidation process. In the real sense, the Gibbs free energy of the oxidation of the various oxides is a function of the pressure and temperature, as in equation 12;

$$\Delta G^\circ = RT \ln P_{O_2} \quad [12]$$

This concept is encapsulated in the Ellingham diagram, on the basis of equation 13.

$$P_{O_2}|_{eq} = \exp \Delta G^\circ / T \quad [13]$$

The equilibrium partial pressure of oxygen is the pressure at which the driving force for the reaction is zero. If the partial pressure of oxygen is greater than this value, the free energy change for the oxidation reaction is negative and there is a driving force for this reaction to take place. Metals or metal alloys will oxidize and the partial oxygen pressure of oxygen will drop to the equilibrium value. Although some details of the dynamics and chemistry, such as how the gas phase environment, especially the partial pressure of oxygen, influences the morphology and configuration of the oxidation product remains unclear, it can be predicted that by varying the parameters of temperature and partial pressure of oxygen, there can be control of the resulting oxides formed²⁵.

Therefore, temperature and partial oxygen pressure affect the kinetics of the oxidation process, the oxidation products, the density of the oxidation products and morphology. The feasibility of these oxides formation is dependent on the Gibbs Free energy which is a function of temperature and oxygen partial pressures.

1.5 Chemical Oxidation Process:

Chemical oxidation uses reagents to produce other chemical compounds. These oxidants work by producing free radicals which then react with the chemical substance being oxidized²⁶. Chemical oxidation of metallic alloys can be initiated by acids, both mineral and organic. Carboxylic acids are compounds containing the carbonyl functional group, -COOH bonded to a hydrogen atom, an alkyl group or an aryl group. These acids can have very long alkyl chains and some are known to occur naturally.

The chemical structure of the carboxylic acid is as shown, in figure 4:

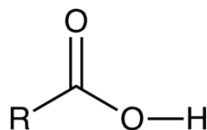
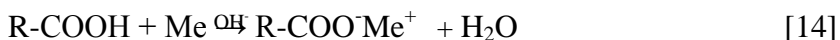


Figure 4: Carboxylic acid structure.

Being a weak acid, it undergoes the typical reactions of acids, some of which include:

[i] Oxidation of metals:

Carboxylic acids react with metals in aqueous solution to form metal salts, known as carboxylates in a chemical oxidation process given by equation 14 below;



The solubility of these carboxylates in water depends on the length of their carbon chains. Metal carboxylates with very long carbon chains, [12-20], are insoluble in water and exhibit hydrophobicity.

[ii] Reaction with metal oxides:

Carboxylic acids equally react with metal oxides in to yield carboxylates, in a slow process that also yields water, as in equation 15.



Some of the carboxylic acids found in nature occur in the form of fatty acids, which include palmitic acid, stearic acid, oleic acid, linoleic acid and arachidonic acid etc. These are essentially long chain carboxylic acids that exhibit hydrophobicity.

It is therefore pertinent to study and to develop newer and more effective methods of generating self-cleaning surfaces on multi-component metal alloys that find use in the water industry. There is also need to develop these self-cleaning surfaces that are durable, chemically and mechanically stable through means that are inexpensive and easy to apply. Therefore, a study of the effect of both thermal and chemical oxidation of the different chemical components found in the C36000 and C84400 copper alloys is necessary.

These thermal and chemical oxidation processes can be used in combination in a thermochemical process. The morphologies of the oxides can be controlled through the parameters of thermal oxidation and the oxides can be involved in different reactions to generate surfaces that can sustain high contact angles for water and oil. These oxidative processes can equally be combined with mechanical abrasion to generate surfaces of different textures. These methods can be applied inexpensively to brasses which are some of the most common metal alloys that are used in the water industry to create self-

cleaning surfaces, thereby solving the problems of fouling on one hand and reducing the incidence of corrosion on the other.

CHAPTER TWO

RESEARCH OBJECTIVES

The basic research objectives of this Dissertation are stated as follows:

[1] To establish the effect of the dimensions of thermally grown oxide nanowires and other metal oxide surface features on the contact angle behavior of water and oil on the surfaces of the C36000 and C84400 copper alloys. The dimensional properties will include the length, diameter and aspect ratios of the nanowire, oxide layer thickness, oxide layer porosity and the oxide nodule sizes; which will be regulated by changing the thermal oxidation parameters of time and partial oxygen pressure.

[2] To study the wetting behavior of oil and water after preliminary surface texturing through the mechanical abrasion of the C36000 and C84400 copper alloys. The behavior of water and oil drops at the solid-air and solid-water interfaces as a function of the surface roughness of the copper alloys will be appraised.

[3] To create anti-wetting and superhydrophobic surfaces on the C36000 and C844000 copper alloys through chemical oxidation with stearic and arachidic acids as well as through a combination of thermal oxidation process with the chemical reaction of the oxides formed with stearic and arachidic acids. The effect of the time of the reaction of the oxides with the stearic and arachidic acid on the contact angle of water will be evaluated. Also, superhydrophobic surfaces will be created through a combination of mechanical abrasion and chemical oxidative processes in modifying the surfaces of the C36000 and C84400 Copper alloys.

[4] To study the contact angle behavior of water on the surfaces on the C36000 and C844000 copper alloys after chemical oxidation treatment with stearic and arachidic acids. Furthermore, a combination of the preliminary mechanical abrasion process with chemical oxidation, using stearic and arachidic acids, will be used to create such surfaces on these selected alloys.

[5] To study the effect of changes in the oxidant concentration, reaction time and the oxidation process temperature on the nature of the surface morphology of the oxidation products formed and on the contact angle behaviour of water.

CHAPTER THREE

LITERATURE REVIEW

Considerable work has been done on the development and creation of nanostructures for various applications. The need for self-cleaning surfaces is providing a new basis for the development of nanostructures on surfaces as well as new techniques for surface modification. This review presents the recent research work that has been done in fabricating metal oxide nanostructures on metal surfaces through thermal oxidation. Focus will also be paid on the generation of nanostructures on metallic alloy surfaces using chemical reaction processes.

Thermal oxidation as a process has been used to produce metal oxide nanostructures on copper and their alloys. These metal oxide nanostructures include ZnO and CuO nanowires and nanoflakes obtained by heating of copper and its alloys^{27, 28, 29}. The structure of the nanowires and nanoflakes were found to be dependent on the temperature and time of the thermal oxidation process.

Beyond copper and copper alloys, other metals have been thermally oxidized to induce the growth of unique forms of metal oxide nanostructures. Following from this, ZnO nanowires have been created on pure zinc and other zinc based substrates through thermal oxidation^{30, 31, 32, 33, 34}. In these studies, the dimension and scale of the ZnO nanostructures were all a function of the thermal oxidation conditions of time, temperature and oxidizing atmosphere used.

Other forms of nanostructures from other metals have been created and reported in literature. These include silicon nanowires generated from direct thermal oxidation of silicon powder in the presence of graphite³⁵; superhydrophobic silicon nanowires³⁶; TiO₂

single-crystalline nanowires by oxidation of titanium substrate in the presence of ethanol vapour³⁷; generation of TiO₂ nanowire through thermal annealing of titanium foils³⁸. The mechanisms of spontaneous formation of oxide nanowires and whiskers from the thermal oxidation of these metals and others have been well established. The growth of these nanowires on the thermal oxidation of copper remain the most representative^{39, 40}. The driving force for the growth of CuO nanowires during the thermal oxidation of copper has been shown to be due to the high compressive stress in the oxide layer which is as a result of the large difference in the molar volumes of the metal and CuO oxide⁴¹.

The effect of temperature on oxide morphology has also been an experimental objective⁴². To this end, the temperature effect on the Cu₂O morphology was investigated by oxidizing Cu (100) thin films within a specific temperature range and at constant oxygen partial pressure. It was demonstrated that dramatically different oxide nanostructures can be achieved by changing the thermal oxidation temperature. The oxidation temperature had effect on the diffusion, surface and interface energies and played great role in the development of different oxide morphology such as pyramids, nanorods, domes or terrace layered structure. Similar results have been observed in other metal systems such as nickel, iron, aluminum, titanium, cobalt, palladium, iridium and tin.

Equally, the effect of oxygen gas pressure has been studied in relationship to the orientation of Cu₂O nuclei formed during the initial oxidation of Cu (100), (110) and (111)⁴³. The study revealed that epitaxial nucleation of oxide could not be maintained for a whole range of the partial oxygen pressure. A transition to non-epitaxial Cu₂O oxide was observed as the oxygen partial pressure increased during the thermal oxidation of Cu (100), (110) and (111) surfaces. The critical oxygen pressures for non-epitaxial

nucleation of the oxide nuclei depended on the surface orientation of the oxidized substrate. The oxygen partial pressure also showed an effect on the morphology of zinc oxide thin films formed during low temperature thermal oxidation⁴⁴. The ZnO thin films were prepared under various oxygen partial pressures at 339 °C and 380 °C. The characterization of the surface oxide films of ZnO showed the presence of whiskers and nanowires as well as cluster-like grains. It was found that the oxide grain size decreased with increasing partial oxygen pressure and thus the ZnO thin films formed at ambient atmosphere exhibited different surface morphology and microstructure when compared to those formed at lower partial oxygen pressure.

These reviewed works clearly show that the morphology of the oxides such as CuO and ZnO have a dependence on the partial oxygen pressures, temperature and time used in initiating the thermal oxidation process. Beyond these parameters stated above, studies on the influence of water vapour on the oxidation of copper at intermediate temperatures have been done⁴⁵. This study involved the thermal oxidation of high purity copper with the oxidation rate measured by means of thermogravimetry within a specific partial oxygen pressure and water vapour pressure ranges at 500 °C respectively.

These studies on the generation of oxide nanowires and other nanostructures through thermal oxidation have been geared towards using these nanostructures for sensors and other applications in the areas of semiconductivity, superconductivity, ferroelectricity and in magnetism. However, such oxide nanostructures can provide a good basis for creating diverse surface morphologies that can cause increase in water and oil contact angles as well as act as a template for chemical modification for inducement of self-cleaning behaviors in metals and their alloys.

To this end, a commercial aluminum alloy has been thermally oxidized in air to create a rough oxide surface of varying morphology on which the wettability of water was studied⁴⁶. The study revealed that the morphological changes occurring during the growth of the Al_2O_3 resulted in the formation of vertical platelets, which conveyed a reduced contact area for water drops which shifted the wetting behavior to Cassie-Baxter state with a contact angle of 128° .

Equally, by applying a thermal oxidation-reduction cycle, superhydrophobicity has been achieved on a pure copper substrate⁴⁷. In this case, morphological changes in the miniature structures of the copper nanowires formed during the thermal oxidation affected the water adhesion behavior effectively producing superhydrophobicity on the copper substrate surface. Through the thermal oxidation of copper substrate, needle-like shaped copper oxide nanowires were formed. Subsequent reduction of the CuO to Cu_2O resulted in superhydrophobicity in water with water contact angle of 160° and hysteresis of 2° .

The wetting behavior of oil droplets for oleophobic/philic surfaces at the water-solid interface has been studied and a model for predicting the contact angle of oil under water based on the surface energy of the oil and the solid surface proposed⁴⁸. On the basis of the model, it was found that for a hydrophilic surface, an oleophobic surface at the oil-water-solid interface can be created if the interfacial energy at the oil and air interface is lower than the interfacial energy at the water-air interface.

Superoleophobic surfaces have many potential applications including underwater antifouling materials among others. High energy oxides have been used to achieve

superoleophobic surfaces which have vast potential application for underwater antifouling application. In this regard, copper oxide coating on copper sheet, achieved through a simple chemical oxidative process in aqueous ammonia solution, has shown underwater superoleophobic behavior⁴⁹. Liu and co-workers further established that the clam shells composed of CaCO_3 are superoleophobic, attributing this phenomenon to the high energy CaCO_3 and the nano-scale roughness of the shells. Some other high energy materials such as nanoclay hydrogels have been coated on metal substrates to induce underwater superoleophobicity⁵⁰. The addition of surfactants has equally been used as a strategy to achieve underwater superoleophobicity at the oil-water interface⁵¹.

However, there has been no attempt to form oxide nanostructures on surfaces of pure metals and their alloys through thermal oxidation for the purpose of studying the underwater contact angles of oil and generating superoleophobic surfaces. The thickness and porosity of the oxide layer can be altered through thermal oxidation. The wetting behavior of oil and water due to such changes has not been studied. The effect of the texture of metallic surfaces on the contact angle behavior of water has been studied in-depth^{52, 53, 54, 55, 56, 57}, but such behavior for oil drops on surfaces under water has not been investigated in detail.

In addition to the thermally induced oxidative process, oxidation can be initiated by simple chemical processes to the extent of creating desired surface features for improve water and oil contact angles. The simple chemical process of oxidation has been achieved through wet chemical reactions^{58, 59, 60}. This has become a straight forward and easy way to make surfaces where there is a need to control the size, shape and dimensionality of the micro and nano-scale structures. This method has been employed in tailoring surface

morphology for self-cleaning. In this regards, superhydrophobic surfaces were fabricated on a copper substrate through a simple chemical oxidative method by immersing in n-tetradecanoic acid solution for about a week without any further surface modification ⁶¹. The n-tetradecanoic acid provided the acidic environment for the copper oxidation reaction. The oxidized copper is believed to be immediately captured by coordination with the n-tetradecanoic acid molecules, forming copper carboxylate nanostructures. This very simple oxidative treatment in a weak long carbon chain organic acid resulted in the formation of surface features that ensured superhydrophobicity.

A combination of chemical oxidation and silanization to create self-cleaning surfaces has been investigated ⁶². The study involved steel, copper and titanium metals. The surfaces were first roughened by $\text{H}_2\text{O}_2/\text{HNO}_3$ etchant, which acted as a powerful oxidant. The etched and roughened metal alloy samples were modified by fluorosilane for superhydrophobicity. Phosphoric acids have also been used to chemically oxidize nickel metal. This resulted in the growth of nano petals on the surface of the nickel. Other workers have used different chemical oxidation routes to generate various morphological features, for modification and subsequent superhydrophobicity and self-cleaning. Aluminium alloy has been reacted in NaOH solution and modified in fluoroalkyl-silane ⁶³; silicon wafers surfaces has been modified with lithographic etching and treated with hydrofluoric acid and silver nitrate solutions to create Si nanowires which are then modified with octadecyltrichlorosilane ⁶⁴.

Other oxidizing agents such as $\text{K}_2\text{S}_2\text{O}_8$ and NaOH have been used to chemically oxidize the copper to form $\text{Cu}(\text{OH})_2$ nanostructures on the surface of the copper substrate. Using this means, CuO micro flower-like protrusions on copper plates have been prepared by

means of surface oxidation ⁶⁵. These surfaces all showed superhydrophobicity and self-cleaning behaviour. CuO ribbons, which showed superhydrophobicity, have been created by oxidizing reaction of copper plates in KOH and $K_2S_2O_8$ through an electrochemical process ⁶⁶. CuO nanosheets on pure copper were formed in a system of NaOH and $[NH_4]_2S_2O_8$ which showed superhydrophobicity when transformed into $Cu[OH]_2$. The reaction process of NaOH and $[NH_4]_2S_2O_8$ with Cu was carefully clarified and the hierarchical structure was that of the flower-like CuO standing on a $Cu(OH)_2$ nanorod resulting in the superhydrophobicity ⁶⁷.

Other workers have used different chemical oxidative routes to generate various morphological features for modification to achieve high contact angles of oil and water for self-cleaning behaviour. For instance, a superhydrophobic MnO_2 nanotube array has been created through a oxidative hydrothermal reaction process using sodium stearate solution ⁶⁸. Water repellent coating has been prepared on ZnO nano particles through reaction with stearic acid to form zinc stearate ⁶⁹; the wear characteristic of the superhydrophobic ZnO nano particles treated with stearic acid to form an overcoat had been earlier evaluated ⁷⁰ and good wear resistance of the superhydrophobic coating was illustrated; an array of ZnO nanorods exhibiting superhydrophobicity has been fabricated. For example, ZnO nanorod has been synthesized on zinc substrate by oxidizing the zinc metal and subsequently modifying it for superhydrophobicity using n-octadecylthiol ⁷¹. Other organic reagents, such as amides, have also been used to induce oxidation for the formation of surface morphological features on metals. The imide- N, N-dimethylformamide solution to oxidize pure zinc substrate to form ZnO nanorods and these nanorods were then modified with stearic acid ⁷². The morphological as well as the

chemical composition changes resulted in the superhydrophobicity of the zinc substrate that was treated. Characterization of the surface showed that the stearic acid assembled on the surface. The superhydrophobicity of the surface so created equally showed good mechanical stability and good tribological properties. Flower-like hierarchical ZnO microspheres have been synthesized via a chemical oxidation route using stearic acid ⁷³. This involved the dispersion of ZnO dry powder in ethanol solution containing octadecanoic acid. The superhydrophobicity was achieved on the ZnO essentially due to the hierarchical roughness of the ZnO microspheres and the low surface energy.

Another approach involving electrochemical deposition and chemical oxidation has been used in achieving superhydrophobicity. This has been applied in creating a superhydrophobic surface on the volatile magnesium substrate ⁷⁴. This method involved electrochemical deposition of copper on the surface of magnesium alloy. The electrochemically deposited copper increased the surface roughness of the magnesium alloy. To achieve superhydrophobicity, the magnesium with the deposited copper was treated with lauric acid in an oxidative process. The substrate exhibited superhydrophobicity with contact angle of water above 150 °. Magnesium substrate has been oxidized in aqueous solution of tetratoxosulphate [VI] acid for a short duration of time and in hydrogen peroxide solution. The oxidized magnesium was the modified further with dilute octadecanoic acid for superhydrophobicity ⁷⁵.

The use of oxidative route to create superhydrophobic surfaces in metals has been restricted to pure metals, implying that no oxidative side reactions of other alloying elements were observed. As seen in the reviewed work above, the superhydrophobicity were achieved by a surface modification of the nanostructures formed on the surfaces as a

product of the oxidation. To this end, no work has been reported on the use of the oxidative approach to create superhydrophobic self-cleaning surfaces in multi-component metal alloys directly without further surface modification. Beyond these, a simple combination of methods for the control of the surface morphology such as thermal oxidation followed by chemical modification or mechanical abrasion followed by chemical oxidation, has not been used before in creating self cleaning superhydrophobic and superoleophobic surfaces in multi-component alloys.

CHAPTER FOUR

MATERIALS AND METHOD

4.1 Materials: The two copper alloys used in the research on the effect of oxidative processes on the contact angles of water and oil are the C36000 and the C84400 copper alloys. The main reasons for the selection of these alloys are because they have huge usage in the water industry where they are used for pipes in water reticulation and other plumbing parts. Baker Manufacturing, situated in Wisconsin, produces these copper alloys and has been interested in finding effective and cheap means of making the alloys self cleaning. Beyond these, these two alloys provide sufficient contrast in the chemical composition. The C36000 copper alloy consist of relatively high weight percentage of zinc compared to the C84400 copper alloy and will therefore behave differently under the different experimental conditions.

The C36000 copper alloy was obtained from Baker Manufacturing, LLC [Evansville, WI] and its chemical composition of the C36000 copper alloy is as shown in Table 1:

Table 1: Table for the chemical composition of C36000 copper alloys.

Element	Cu	Fe	Pb	Zn
Nominal Wt.%	61.5	0.35	3.0	35.4

The C84400 copper alloy was also obtained from Baker Manufacturing, LLC [Evansville, WI], Milwaukee. In terms of the chemical composition of the C84400 copper alloy, the various alloying components are given in Table 2;

Table 2: Table for the chemical composition of C84400 copper alloys.

Element	Cu	Pb	Sn	Zn
Nominal Wt.%	81	7	3	9

The various nitrogen and oxygen gas mixtures used in the thermal oxidation of the C36000 and C84400 copper alloys include the following:

[i] Nitrogen- 0.75 Wt. % Oxygen

[ii] Nitrogen-5 Wt. % Oxygen

[iii] Nitrogen-12 Wt. % Oxygen.

[iv] Air

These gas mixtures were all obtained from Praxair and were used to convey different oxygen partial pressures on the closed furnace during the thermal oxidation process. These partial oxygen pressures corresponded to ---atm, 0.044atm and 0.10 atm in nitrogen-0.75 Wt. % oxygen, nitrogen-5 Wt. % oxygen and nitrogen- 12 Wt. % oxygen gas mixtures respectively; based on the relationship:

Partial Oxygen Pressure = Absolute Pressure [in atm] \times Vol. Percent of O₂ in N₂-O₂ gas mixture.

The chemical reagents that were equally used are listed as follows:

[i] Stearic acid (C₁₈H₃₆O₂): This acid is also referred as octadecanoic acid and was obtained from Sigma-Aldrich Chemicals, Milwaukee. It was 99% purity grade in quality. In terms of the physical property, the density, melting point and solubility in water of the stearic acid are 0.847g/ml, 69.6 °C, and 3mg/l respectively.

[ii] Arachidic acid [C₂₀H₄₀O₂]: This acid is also known as eicosanoic acid and was obtained from Sigma-Aldrich Chemicals in Milwaukee. The grade quality was 99%

purity with the physical properties of density and melting point given as 0.824/ml and 75.5 °C respectively.

[iii] Ethyl Alcohol: Ethyl Alcohol of 98% grade was obtained from Fisher Company for use as the main solvent for the experiments.

[iv] Zinc Stearate [$C_{36}H_{70}O_4Zn$]: This metal salt of zinc and stearic acid was obtained from Sigma-Aldrich Chemicals in Milwaukee, with 99.9% grade quality.

[v] Lead Stearate [$C_{36}H_{70}O_4Pb$]: This was equally obtained from Sigma-Aldrich Chemicals, Milwaukee and was of 99% grade purity.

[vi] Copper Stearate [$C_{36}H_{70}O_4Cu$]: This chemical was obtained from Pfaltz and Bauer, Waterbury, Connecticut and was of 99 % grade purity.

[vii] Copper (II) Oxide, Zinc Oxide and Lead (II) Oxide powders

[viii] Distilled water

Grinding and polishing of the C36000 and C84400 copper alloy samples for different experiments was done using a Buehler polishing machine (Buehler Metaserv 3000 model). Rough mechanical abrasion was done with different grades of SiC papers while fine polishing was done with a soft cloth impregnated with 1 micron alumina slurry.

Two types of furnaces were used in the process of thermal oxidation of the C36000 and C84400 copper alloys. A specific type of furnace with outlets for the flow of gas in and out of the thermal oxidation chamber was used for the thermal oxidation of samples under different oxygen partial pressures. In this case, the thermal oxidation furnace, with

an inlet and outlet for the flow of the oxidizing gases, was used. However, for thermal oxidation in air an electric Thermolyne furnace from Thermo-scientific was used. These furnaces are shown in figures 5 and 6 below:



Figure 5: Thermal oxidation furnace



Figure 6: Electric furnace

For the chemical reactions of the thermally oxidized copper alloys with the long chained carboxylic acids, a pressure reactor vessel (Parr Pressure reaction apparatus, model 4601Q) was used. This vessel is shown in figure 7.



Figure 7: Parr Pressure reaction apparatus, model 4601Q

4.2 Research Method:

Four basic approaches or methods are adapted for this study of generating different surface morphologies for superhydrophobicity and underwater superoleophobicity on the surfaces of C36000, C84400 and for the study of the contact angles of oil and water at the solid-water and solid-air interfaces respectively.

These are:

[i] Thermal oxidation.

[ii] Chemical Oxidation

[iii] Thermochemical reaction process (combination of thermal oxidation and chemical reaction)

[iv] A combination of mechanical abrasion and chemical oxidation.

These methods and how they are used are explained below:

4.2.1 Thermal Oxidation method: The thermal oxidation process involved the controlled oxidation of the sectioned samples of C36000 and C84400 copper alloys in a closed furnace system. The following procedures are followed for the process of thermal oxidation:

[i] For thermal oxidation in different N_2 - O_2 gas mixtures, the sectioned samples were polished until fine surfaces were obtained by using a soft cloth impregnated in 1 micron alumina slurry. The polished samples were then washed in distilled water and dried in air. To establish the oxidation atmosphere, the various N_2 - O_2 gas mixtures were flowed

through the furnace shown in figure 5 with an inlet and outlet for the introduction of the oxidizing gas mixtures, at a rate of 4.5 liters per minute . The temperature of the furnace was ramped up to the different temperatures desired for the specific experiments and after a time period of 10 minutes for the homogenization of the oxidization gas mixture within the furnace, the samples were push into the hot zone of the furnace. The times set for the thermal oxidation process were 1, 2 and 3 hours respectively and the process was done at atmospheric pressure. After the thermal oxidation for the specified time, the samples were slowly removed and allowed to cool in an evacuated bell jar. For those samples that are oxidized in air, the oxidation is carried out in ambient conditions at the desired temperature in the electric furnace shown in figure 6 for 1, 2, 3 and 4 hours at different desired temperatures.

4.2.2 Chemical Oxidation method: The chemical oxidation method followed the wet immersion procedure which involved the following steps:

[i] The C36000 and C84400 copper alloys were first sectioned into smaller sizes and mounted in polymers for proper handling.

[ii] These mounted samples are polished on a soft cloth impregnated with 1 micron alumina slurry until a smooth, fine surfaces of 1 micron in the average surface roughness is achieved.

[iii] The chemical oxidation of these prepared samples of C36000 and C84400 copper alloys was carried out in by immersion of the samples in aqueous solutions of various concentrations of stearic and arachidic acids. The process of the chemical oxidation of the

copper alloys was carried out over a period of 5 days and the contact angles of water, surface roughness, and surface morphology duly monitored within this time frame.

4.2.3 Thermo-chemical reaction method:

The thermochemical reaction process involves a combination of the thermal oxidation and the chemical reaction processes in modifying the surfaces of the C36000 and C84400 copper alloys. The procedures used are as stated below:

[i] Sectioned and polished samples are first thermally oxidized in air for a specific time, for the formation of various oxides with different morphologies on the samples.

[ii] The oxides are then chemically reacted further to form salts of stearic and arachidic acids at temperatures above 100 °C. In this case, the reaction is carried out in a closed process reactor, shown in figure 7, placed in a furnace for different time durations in specific concentrations of stearic and arachidic acids.

4.2.4 Combination of mechanical abrasion and chemical oxidation:

The processes involved in this route included the mechanical abrasion of the C36000 and the C84400 copper alloys that had been sectioned and mounted in polymers with a particular grade of SiC abrasive paper. After this, the procedures in 3.2.2 from [iii] to [iv] were repeated for a specific concentration of the stearic and arachidic acids respectively. The contact angles of water and oil underwater were specifically measured on the mechanically abraded surfaces before the chemical oxidation. These measurements were also repeated after the chemical oxidation.

[4.3] Surface characterization methods:

To characterize the surfaces, the following were done:

[i] Surface roughness measurement

[ii] Water and oil contact angle measurement

[iii] Determination of chemical composition of the thermally and chemically oxidized surfaces.

[iv] Surface morphology examination.

[i] Surface Roughness Measurement:

The surface roughness parameter of interest that was measured before and after the surface modification by the various methods earlier stated is the average surface roughness, R_a . This was measured with the use of a surface profilometer (Taylor Hobson 2-D precision profilometer). The R_a was measured for five times after which the averages of the five readings were taken. The Taylor Hobson 2-D precision profilometer is shown in figure 8.



Figure 8: Taylor Hobson 2-D precision profilometer

[ii] Water and Oil Contact angle measurement:

The water contact angles on the oxidized samples as well as the oil contact angles on the surfaces in underwater conditions were measured using the goniometer (Rame Hart 250 model). Distilled water or vegetable oil drops are placed on five different places on the surfaces of the samples and the contact angles duly measured after which the average of the five readings are taken. The Rame Hart 250 model goniometer is shown in figure 9.



Figure 9: Rame Hart 250 model goniometer.

[iii] Determination of the chemical composition of the oxidized surfaces:

The evaluation of the oxide phases on the surfaces after thermal oxidation was done with the use of energy dispersive X-ray analysis as well as with X-ray diffraction. The later involved the use of the Scintag 2000 X-ray diffraction equipment. Equally, for the samples of the C36000 and C84400 copper alloys modified through the processes involving chemical oxidation, the chemical composition of the surfaces are evaluated through the energy dispersive X-ray, X-ray diffraction and infra-red spectroscopic techniques.

[iv] Surface Morphology examination:

The examination of the surface morphology was done using the optical microscope and the scanning electron microscope. The S-4800 Hitachi scanning electron microscope is shown in figure 10.



Figure 10: S-4800 Hitachi scanning electron microscope

[v] Evaluation of the surfaces with the Atomic Force Microscope, AFM:

The atomic force microscope was applied to study the nature of the surface and evaluate the roughness parameters of S_a and S_p for samples that were chemically oxidized in arachidic acid at different temperatures. This AFM model is shown in figure 11.



Figure 11: Nanosurf Nanite B Atomic Force Microscope

CHAPTER FIVE

UNDERWATER OLEOPHOBIC BEHAVIOUR AND WETTING TRANSITION ON MECHANICALLY ABRADED SURFACES OF C36000 AND C84400 COPPER ALLOYS

5.0 Introduction: As a preliminary step before the various oxidization process for the C36000 and C84400 copper alloys, mechanical abrasion of the surfaces was used to generate different surface textures of varying roughness. A detailed evaluation of the contact angles of water and oil was done to determine the various wetting regimes for these surfaces.

5.1 Characterization of mechanically abraded surfaces of C36000 and C84400 copper alloys:

The average surface roughness, R_a of the samples was measured using the surface profilometer. To study the wetting regime and the wetting transitions of the oil drops in underwater conditions, the contact angles of the oil drops on the abraded surfaces were measured using the goniometer. The surfaces of the samples were equally studied using the scanning electron microscope.

5.1.1 Surface morphology study of the mechanically abraded surfaces of C36000 and C84400 copper alloys:

The SEM images of the mechanically abraded surfaces and the evaluated contact angles of oil drops are shown in figures 12 and 13 below for the C36000 and C84400 copper alloys respectively. Rough, deep randomly oriented grooves were observed on the surfaces due to the mechanical abrasion.

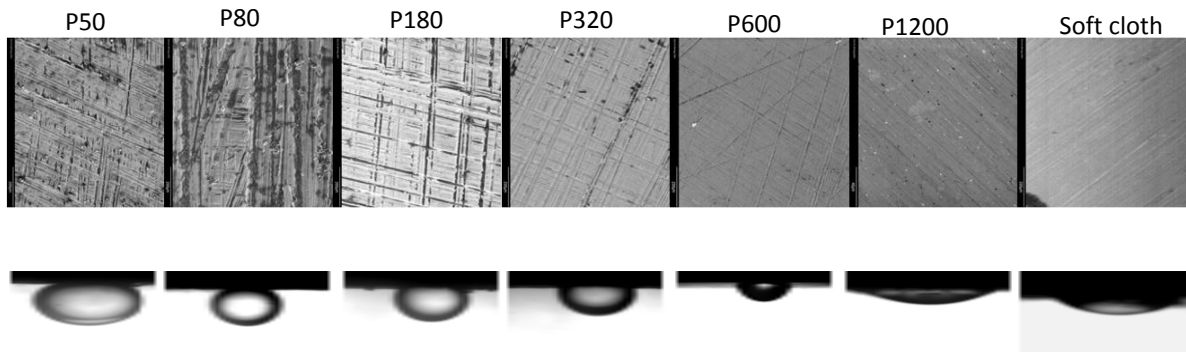


Figure 12: Surface morphology and contact angles of oil on mechanically abraded surfaces of C36000 copper alloy.

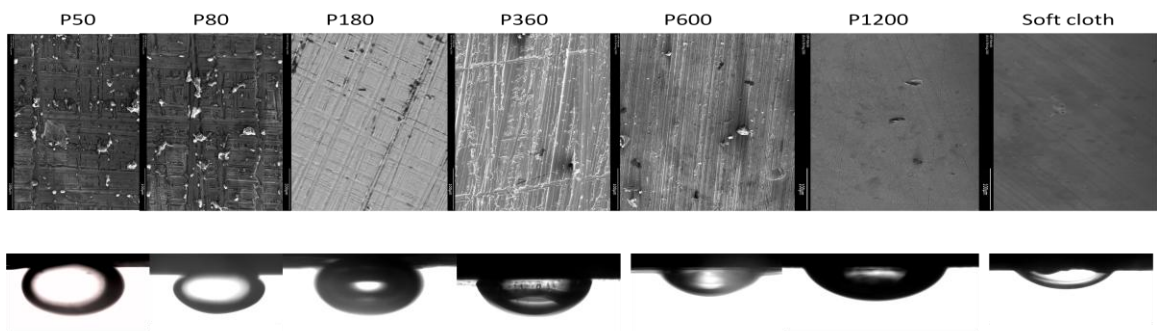


Figure 13: Surface morphology and contact angles of oil on mechanically abraded surfaces of C84400 copper alloy.

The abrasion wear of the surfaces, as seen from the SEM images, increases with increase in abrasive particle size for the C36000 and C84400 copper alloys. This is confirmed by the increase in the value of the average surface roughness, R_a . This increase in the abrasive wear can be attributed to the fact that the coarse SiC abrasive particles tend to dig in and plough out the alloy material resulting in huge alloy material removal. For the smaller grit size SiC papers, the abrasive particles are less densely populated compared with larger grit size paper. Furthermore, the contact surface area per abrasive SiC particle will be higher in smaller grit Size SiC paper compared to those present in larger grit size paper. Higher contact surface area tends to increase the plastic deformation of the

abraded alloy surfaces and produces larger grooves in the resulting surface wear. The particle sizes of the SiC particles for these grit sizes are stated in Table 3.

Table 3: Grit size and average diameter of SiC carbide paper used in mechanical abrasion

Grit size of SiC paper	50	80	180	320	600	1200
Average diameter of SiC particle (μm)	336	201	82	46.2	25.8	15.3

5.2 Surface roughness and underwater oil contact angle evaluation and wetting transition:

The average surface roughness values, R_a , of the C36000 and C84400 copper alloys increased based on the grit size of the SiC paper used for the mechanical abrasion process. These results are as stated in Table 4. Also, the contact angles of oil drops on surfaces under water as well as those of water and oil drops in the air interface were evaluated on the surfaces of the mechanically abraded copper alloy samples. The values of the contact angles obtained are as stated in Table 4:

Table 4: Underwater oil contact angles on mechanically abraded surfaces of C36000 and C84400 copper alloys.

Grit size	Mechanically abraded C36000				Mechanically abraded C84400			
	R_a	Θ_w	Θ_{oa}	Θ_{ow}	R_a	Θ_w	Θ_{oa}	Θ_{ow}
50	3.3	$65.4^\circ \pm 2.1^\circ$	$27.1^\circ \pm 1.5^\circ$	$132.4^\circ \pm 4.4^\circ$	3.4	$72.7^\circ \pm 7.5^\circ$	$64^\circ \pm 5.2^\circ$	$123.2^\circ \pm 7.9^\circ$
80	1.9	$70.4^\circ \pm 0.6^\circ$	$22.7^\circ \pm 4.3^\circ$	$113.2^\circ \pm 11.8^\circ$	1.6	$80.8^\circ \pm 8.0^\circ$	$41.1^\circ \pm 11.2^\circ$	$111.9^\circ \pm 8.7^\circ$
180	1.2	$71^\circ \pm 2.3^\circ$	$11.7^\circ \pm 0.7^\circ$	$106^\circ \pm 5.2^\circ$	1.0	$70.3^\circ \pm 3.6^\circ$	$53.2^\circ \pm 4.9^\circ$	$112.4^\circ \pm 12.3^\circ$
320	0.7	$70^\circ \pm 1.4^\circ$	$39.1^\circ \pm 1.2^\circ$	$101^\circ \pm 4.1^\circ$	0.7	$77.6^\circ \pm 2.3^\circ$	$45.7^\circ \pm 7.0^\circ$	$80.6^\circ \pm 14^\circ$
600	0.5	$78.7^\circ \pm 5.8^\circ$	$32^\circ \pm 1.8^\circ$	$83.2^\circ \pm 3.8^\circ$	0.4	$70.7^\circ \pm 3.9^\circ$	$59.7^\circ \pm 4.4^\circ$	$69.1^\circ \pm 2.5^\circ$
1200 Grit	0.2	$74.4^\circ \pm 3.9^\circ$	$41.5^\circ \pm 3.0^\circ$	$69.5^\circ \pm 5.5^\circ$	0.1	$65.4^\circ \pm 2.6^\circ$	$65.0^\circ \pm 3.3^\circ$	$64.1^\circ \pm 3.0^\circ$
0.1 μm Alumina	0.1	$58.1^\circ \pm 4.9^\circ$	$31.6^\circ \pm 1.4^\circ$	$53.0^\circ \pm 1.1^\circ$	0.1	$54.7^\circ \pm 1.2^\circ$	$51.0^\circ \pm 2.3^\circ$	$58.2^\circ \pm 1.7^\circ$

The contact angles of oil were also measured on surfaces that were abraded under an applied force of 5lb and 10 lb for 1.0 to 12.5 minutes. The contact angles obtained for these set conditions of mechanical abrasion are stated in Table 5, Table 6 and Table 7.

Table 5: Underwater oil contact angle on C36000 and C84400 mechanically abraded with 50 grit SiC paper under controlled applied force and time.

Abrasion of C36000 and C84400 with 50 grit size SiC paper			
Applied Force(Fa), lb	Abrasion Time (minutes.)	Θ _{ow} on C36000	Θ _{ow} on C84400
5	1.0	116.5° ± 5.8°	112.6° ± 2.6°
	1.5	107.8° ± 7.6°	117.6° ± 3.9°
	2.0	115.5° ± 11.1°	110.6° ± 5.4°
	2.5	117.8° ± 4.3°	117.3° ± 4.7°
10	1.0	114.2° ± 9.6°	118.9° ± 2.8°
	1.5	95.2° ± 6.9°	114.9° ± 3.1°
	2.0	114.5° ± 4.5°	110.6° ± 2.4°
	2.5	112.4° ± 8.7°	108.7° ± 1.9°

Table 6: Underwater oil contact angle on C36000 and C84400 mechanically abraded with 180 grit SiC paper under controlled applied force and time.

Abrasion of C36000 and C84400 with 180 grit size SiC paper			
Applied Force(Fa), lb	Abrasion Time (minutes)	Θ _{ow} on C36000	Θ _{ow} on C84400
5	2.5	102.9° ± 3.5°	91.4° ± 4.0°
	5.0	100.5° ± 4.9°	112.0° ± 6.9°
	7.5	105.2° ± 8.1°	101.3° ± 4.7°
	10.0	103.7° ± 7.2°	109.2° ± 8.3°
10	2.5	101.6° ± 4.1°	106.5° ± 1.5°
	5.0	103.5° ± 1.9°	104.3° ± 2.8°
	7.5	101.4° ± 5.6°	113.6° ± 3.3°
	10.0	103.8° ± 2.7°	107.4° ± 4.9°

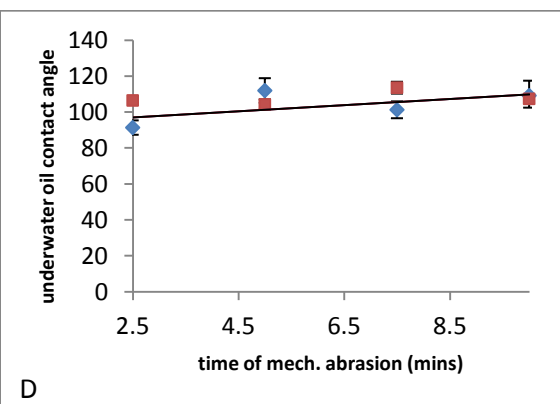
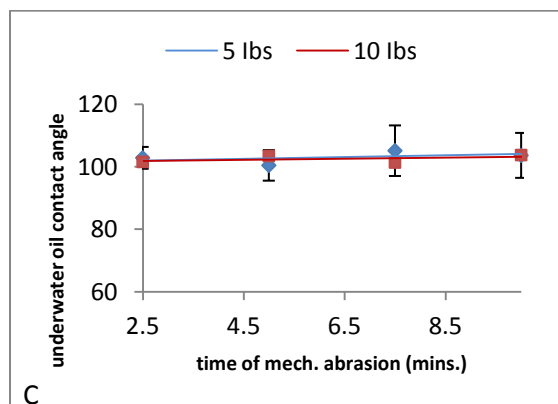
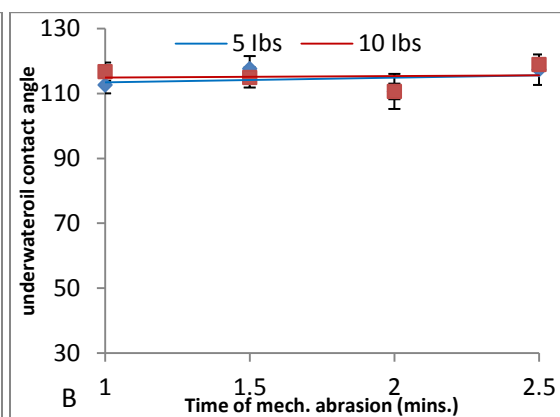
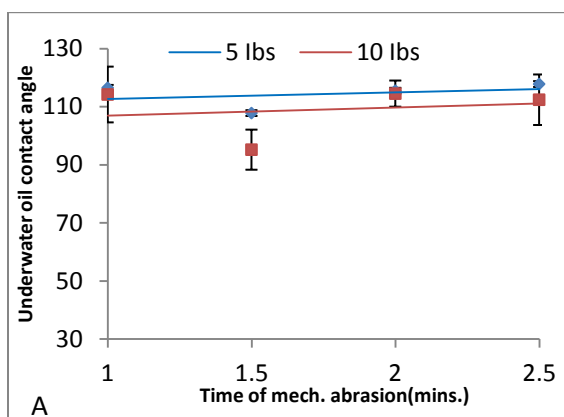
Table 7: Underwater oil contact angle on C36000 and C84400 mechanically abraded with 320 grit SiC paper under controlled applied force and time.

Abrasion of C36000 and C84400 with 320 grit size SiC paper			
Applied Force(Fa), lb	Abrasion Time (minutes)	Θ_{ow} on C36000	Θ_{ow} on C84400
5	2.5	$52.9^\circ \pm 3.5^\circ$	$94.4^\circ \pm 4.0^\circ$
	5.0	$69.7^\circ \pm 10.9^\circ$	$98.7^\circ \pm 2.8^\circ$
	7.5	$67.4^\circ \pm 5.8^\circ$	$96.2^\circ \pm 1.4^\circ$
	10.0	$68.9^\circ \pm 10.3^\circ$	$92.4^\circ \pm 3.8^\circ$
10	2.5	$28.8^\circ \pm 10.7^\circ$	$91.4^\circ \pm 4.9^\circ$
	5.0	$39.4^\circ \pm 9.3^\circ$	$88.6^\circ \pm 10.6^\circ$
	7.5	$46.5^\circ \pm 7.9^\circ$	$85.3^\circ \pm 5.1^\circ$
	10.0	$34.2^\circ \pm 6.2^\circ$	$87^\circ \pm 4.3^\circ$

It was observed that for water drops, there is no significant change in the contact angle with increasing R_a . However, the contact angle of oil in air gradually decreased with increasing roughness from the value of about 42° and reaches the minimum of about 12° at R_a values of 1.2 microns for C36000 copper alloy. The contact angle of oil on the surfaces of the mechanically abraded surfaces of the C84400 and C36000 copper alloys at the solid-air interface decreased. For both surfaces of the copper alloy samples, the mechanical abrasion induced change in surface roughness only accentuated the hydrophilicity of the surface in the water-air and oil-air interfaces as seen in figure 15 and figure 16. It is equally noted that the contact angle of oil in underwater condition did not change with time when the surfaces of the C36000 and C84400 copper alloys were abraded under different applied forces. The slopes of the plots of the average contact angles of oil against time, from figure 14, were very comparable for the two values of the applied force that was used during the mechanical abrasion process.

Table 8: Table of the slope of contact angle of oil in underwater condition as a function of the applied force, F_a and time [minutes] during mechanical abrasion with different grit sizes of SiC paper.

Grit Size	Applied force (F_a) Ib	Slope ($^{\circ}/\text{min}$)	
		C36000	C84400
50	5	2.32	1.4
	10	2.78	0.5
180	5	0.28	1.70
	10	0.18	1.70
320	5	1.8	0.22
	10	0.9	0.39



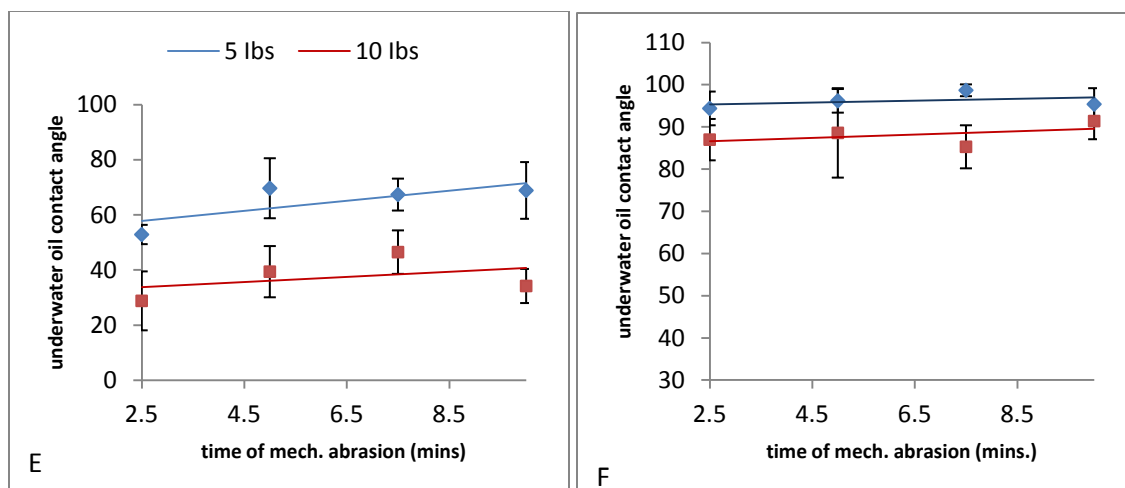


Figure 14: Plot of underwater oil contact angle against time of mechanical abrasion for varied applied forces: [A] for C36000 copper alloy abraded with 50 grit size SiC paper [B] for C84400 copper alloy abraded with 50 grit size SiC paper [C] for C36000 copper alloy abraded with 180 grit size SiC paper [D] for C84400 copper alloy abraded with 180 grit size SiC paper [E] for C36000 copper alloy abraded with 320 grit size SiC paper [F] for C84400 copper alloy abraded with 320 grit size SiC paper.

However, for oil droplet in water there is wetting transition in the measured contact angles of the oil droplets. For the C36000 copper alloy, this transition from olephilicity to oleophobicity is observed at a surface roughness equal to 0.7 microns; while in the C84400 copper alloy, this transition is observed at 0.96 microns for the average surface roughness value.

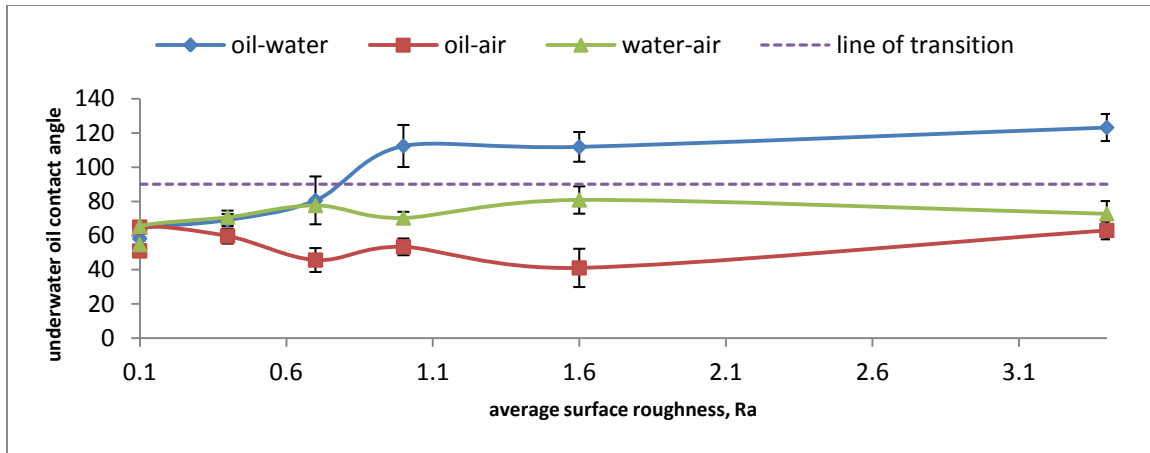


Figure 15: Graph of wetting regimes of oil drop on C84400 surface in air and water and water drop on C84400 surface in air.

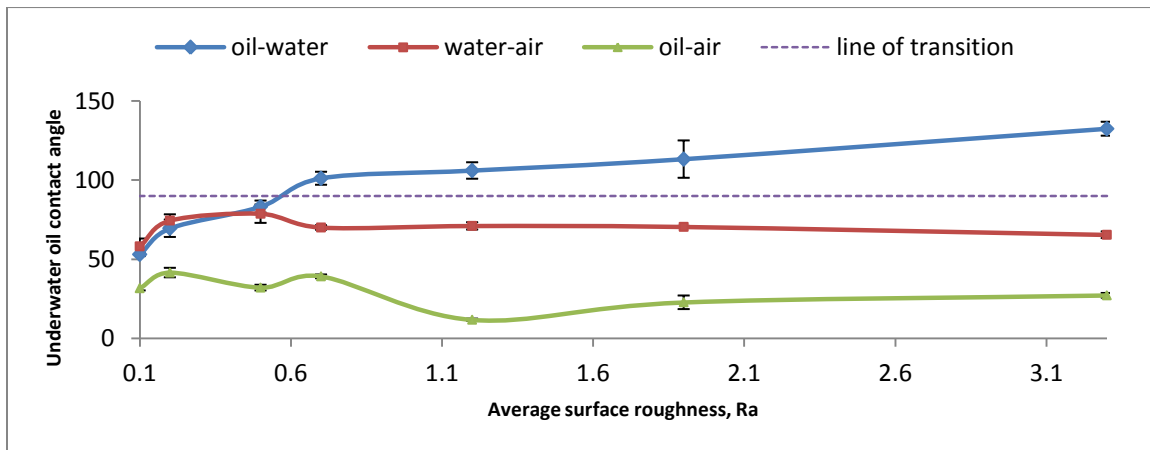


Figure 16: Graph of wetting regimes of oil drop on C36000 surface in air and water and water drop on C36000 surface in air.

This abrupt change in the contact angle of oil in this underwater condition is attributable to the transition from the Wenzel to the Cassie-Baxter regimes. The contact angles, based on the Wenzel regime $[\theta_w]$ as given by equation [2] are confined to the smoother surfaces of the mechanically abraded surfaces of the C36000 and C84400 copper alloys.

We know that both R_f and R_a are the measures of surface roughness. However, for rough surfaces the $R_f \geq 1$ and is a non-dimensional parameter while $R_f = 1$ for smooth, polished surfaces. For the rougher surfaces, where the average surface roughness values are above

0.7 and 0.96 microns for the C36000 and C84400 samples respectively, the Cassie-Baxter regime, given in equation 5, becomes operative.

It is expected that increase in the average surface roughness, R_a , will cause a corresponding increase in the roughness factor, R_f of the abraded surfaces. Accordingly from equation 2 for the initially oleophilic surfaces of the alloy samples [$\cos \Theta_o > 0$], increasing the surface roughness cannot result in a transition to oleophobicity [$\cos \Theta_w < 0$]. To this extent, the Wenzel model in equation 2, cannot be used to explain this transition from oleophilicity to oleophobicity.

However, using the Cassie-Baxter regime, the transition from oleophilicity to oleophobicity in underwater conditions for the oil drops on these abraded surfaces can be explained. It is observed from the Cassie-Baxter model in equation 5, that the abrupt transition from oleophilicity to oleophobicity of the oil drops on these surfaces can be attributed to either the f_{s_o} or the R_f . Mechanical abrasion of the surface with SiC paper results in the increase of the average surface roughness hence the roughness factor, R_f . However, based on the Cassie-Baxter equation, increase in the roughness factor, R_f will not cause a change of sign of $\cos \Theta_o$ from positive [oleophilic] to negative [oleophobic]. Therefore, the only effective explanation for the observed transition is in the change in the f_{s_o} due to the mechanical abrasion.

The relationship between the R_a and R_f is not straight forward due to the chaotic irregularity of the abraded surface generated and therefore, for the purpose of explaining the results, we assume using geometrical considerations that the non-dimensional R_f change with R_a [measured in micrometers], is given by the relationship:

$$R_f = R_a / (3 + 0.5 R_a) + 1 \quad [16]$$

In analyzing the data for C36000 and C84400 copper alloys using the Cassie-Baxter equation, the fractional areas of the solid-oil, f_{so} , is assumed to be equal to 0.15 and 0.23 for the abraded C36000 and C84400 copper alloy surfaces respectively. Such choice of parameters provides a reasonable fit of the experimental data for small roughness values, where $R_a < 0.3 \mu\text{m}$, for the copper alloy samples with Wenzel model and for large roughness values [$R_a > 0.7 \mu\text{m}$ and $R_a > 0.96 \mu\text{m}$ for the C36000 and C84400 copper alloy respectively] with the Cassie-Baxter model. Also, the assumption of the constant solid-oil contact area does not stand in the transition region [$0.3 \mu\text{m} < R_a < 0.7 \mu\text{m}$ for the C36000 copper alloy and $0.4 < R_a < 1.2 \mu\text{m}$ for the C84400 copper alloy].

To account for the change in the f_{so} during the transition from the Wenzel state to the Cassie-Baxter state, a piece-wise dependency of the f_{so} on the surface roughness was assumed. Therefore, for the C36000, the assumption follows that:

$$f_{so} = \begin{cases} -0.956R_a + 0.95; & 0\mu\text{m} \leq R_a < 0.7\mu\text{m} \\ -0.06R_a + 0.33; & 0.7\mu\text{m} \leq R_a < 3.3\mu\text{m} \\ 0.15 & ; R_a \geq 3.3. \end{cases} \quad [17]$$

And in the C84400 roughed samples, the piece-wise dependency of f_{so} on the surface roughness follows that:

$$f_{so} = \begin{cases} -0.0156R_a + 0.395; & 0\mu\text{m} \leq R_a < 1.2\mu\text{m} \\ -0.078R_a + 0.49 & ; 1.2\mu\text{m} \leq R_a < 3.4\mu\text{m} \\ 0.23 & ; R_a \geq 3.4 \end{cases} \quad [18]$$

The Cassie-Baxter model, taking into account the changing f_{so} , as given in equations 17 and 18 effectively explains the experimental trend of oleophilic to oleophobic transition as shown in figure 17 [a and b] below:

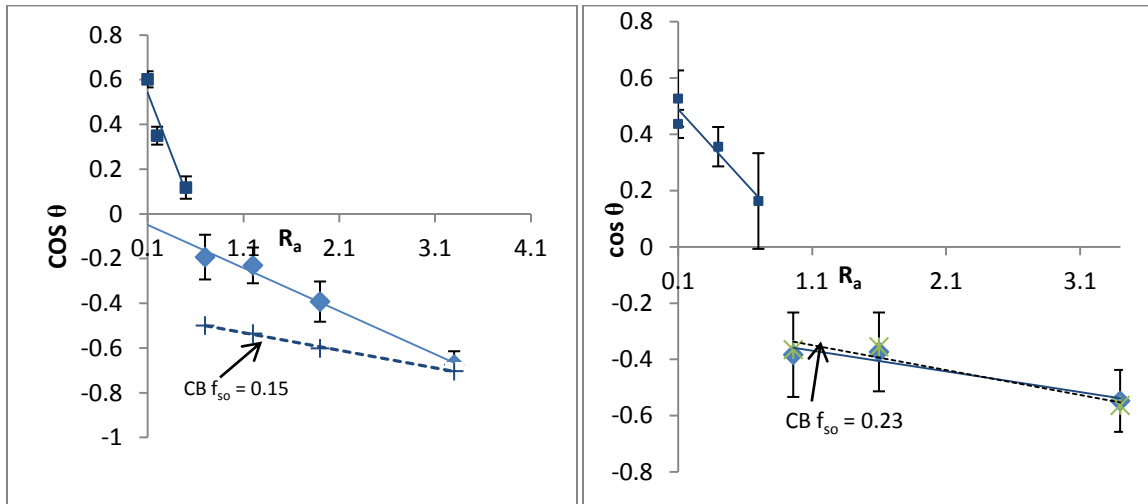


Figure 17: Contact angle of oil under water on mechanically abraded surfaces of C36000 and C84400 copper alloys showing the Cassie-Baxter and Wenzel wetting regimes as a function of average surface roughness, R_a .

From the preliminary surface texturing through mechanical abrasion prior to the other surface treatments, there is an abrupt increase in the contact angle of oil in underwater system as a function of the surface average roughness. The increase in values and transition in the underwater oil contact angle behaviour cannot be explained strictly using the Wenzel or the Cassie-Baxter models; however, it is consistent with the wetting regime change from the Wenzel to the Cassie-Baxter state. Equally, the wetting regimes and contact angle behaviour of water and oil in the air and water interfaces showed independence to the time of the mechanical abrasion as well the applied force used for the abrasion process.

CHAPTER SIX

WETTING BEHAVIOUR OF WATER ON THERMALLY OXIDIZED SURFACES OF C36000 COPPER ALLOY

6.0 Introduction:

The C36000 copper alloy is a type of leaded brass consisting of copper, zinc and lead as the alloying elements. In order to appraise the microstructure and the elemental composition of the C36000 copper alloys used in this research, the samples were polished and etched using a method described elsewhere ⁷⁶ and the microstructures obtained are as shown in figure 18.

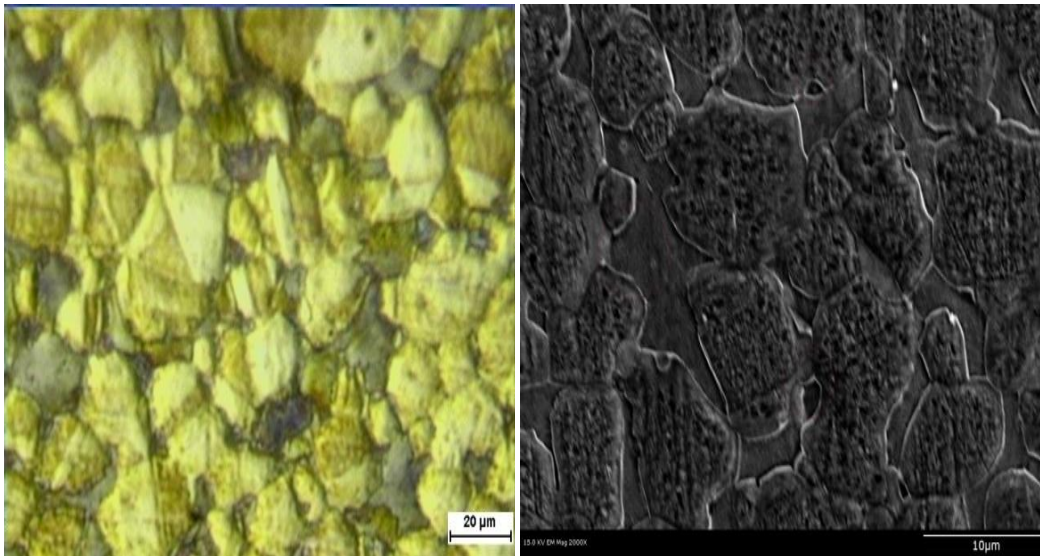


Figure 18: Optical and SEM micrographs of the microstructure of C36000 copper alloy.

From the above optical microscope and SEM images of the microstructure of the C36000 copper alloy that the discrete lead particles are primarily in the grain boundaries and inter-dendritic regions. The lead particles are practically insoluble in the C36000 microstructure. The two phase structure consists of the alpha and beta phases. Elemental analysis and quantification of the polished C36000 copper alloy through Energy

Dispersive X-ray study showed elemental composition in terms of atomic and weight percentages as stated in Table 9.

Table 9: Elemental composition of C36000 copper alloy from EDX analysis

Element	Atomic %	Weight %
Copper	65.61	61.70
Zinc	32.03	31.05
Lead	2.36	7.25

The elemental mapping of the distribution of these elements within the microstructure of the alloy showed the lead particles were clearly concentrated within specific regions within the microstructure while the copper and zinc alloying elements were evenly distributed within the matrix as stated in figure 19.

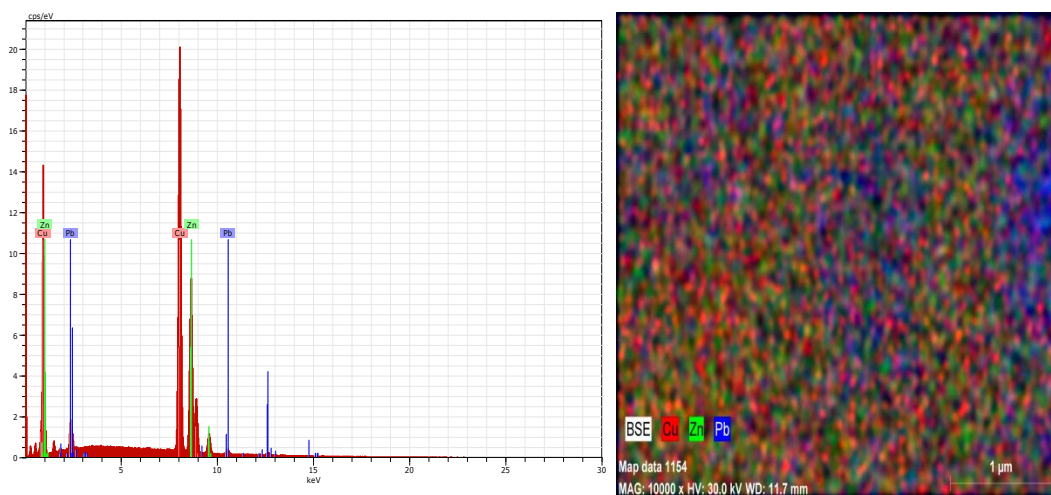


Figure 19: EDX spectrum and elemental map showing percentage and distribution of the alloying elements in the microstructure of C36000 copper alloys.

6.1 Experiment: The samples of the C36000 copper alloy were sectioned into the dimension of $2 \times 1 \times 0.5$ mm. These samples were polished until fine surfaces are obtained. The thermal oxidation processes were done in air and in various N_2 - O_2 gas mixtures. The concentration of oxygen is controlled by using gases with specific oxygen

content for the oxidation in closed furnace shown in figure 5. The furnace atmosphere is controlled by initially flowing of the gas through the furnace chamber. The temperature is then ramped up to the desired value.

The gas mixtures used include:

- (i) Nitrogen-0.75 Wt. % Oxygen.
- (ii) Nitrogen- 5 Wt. % Oxygen and
- (iii) Nitrogen- 12 Wt. % Oxygen

The controlled temperature is set at 550 °C and 650 °C and the thermal oxidation were carried out for 1 to 3 hour duration.

6.2 Characterization: The characterization included the determination of the chemical composition of the oxidized sample surfaces by using the Scintag-2000 XRD machine for X-ray diffraction analyses; the evaluation of the surface morphology using the Hitachi-4800 scanning electron microscope (SEM) equipped with the energy dispersive X-ray probe. The evaluation of the chemical composition of the oxide nanowires was carried out by using the energy dispersive X-ray instrument attached to the Hitachi-4800 scanning electron microscope while the measurement of the contact angle for water and oil (underwater) was done with the Rame Hart 500 model goniometer. The average surface roughness, R_a , was evaluated with a 2-D profilometer.

6.3 Results and Discussion:

The results from the thermal oxidation of the C36000 copper alloy in these various oxidizing conditions in terms of the chemical composition of the oxides formed, surface morphology and the contact angles of water are discussed as follows:

6.3.1 Identification of phases on the surfaces of the oxidized samples of C36000 copper alloy.

X-ray diffraction with a 2θ range of $10-70^\circ$ at a continuous count rate of 2 degrees per minute using the α -Cu emission was used to study the surfaces. The X-ray diffraction patterns obtained are shown in figures 20, 21 and 22 respectively for the C36000 samples oxidized in $N_2-0.75$ wt. % O_2 , N_2-5 wt. % O_2 and N_2-12 wt. % O_2 gas mixtures respectively at $650^\circ C$. In the $N_2-0.75$ wt. % O_2 , N_2-5 wt. % O_2 and N_2-12 wt. % O_2 the major diffraction peaks corresponded to the (100),(002), (001) and (102) planes of ZnO. Equally, a (310) plane of the PbO was observed from the X-ray diffraction studies, implying that the Pb precipitates at the grain boundaries of C36000 Copper alloy microstructure were oxidized to PbO.

All the peaks for the ZnO formed on the surfaces of the samples in all the N_2-O_2 oxidizing atmospheres confirm a hexagonal ZnO crystal structure. Also, the preponderance of the ZnO X-ray diffraction peaks implies that the oxide layer is mainly composed of ZnO as a continuous phase in the oxide layer.

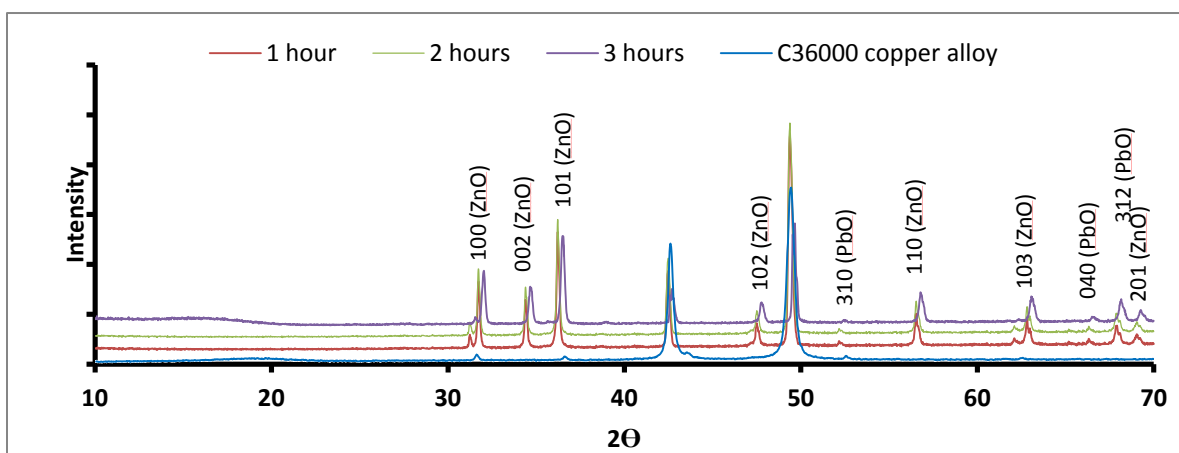


Figure 20: X-ray diffraction pattern of C36000 copper alloy thermally oxidized in $N_2-0.75$ wt.% O_2 .

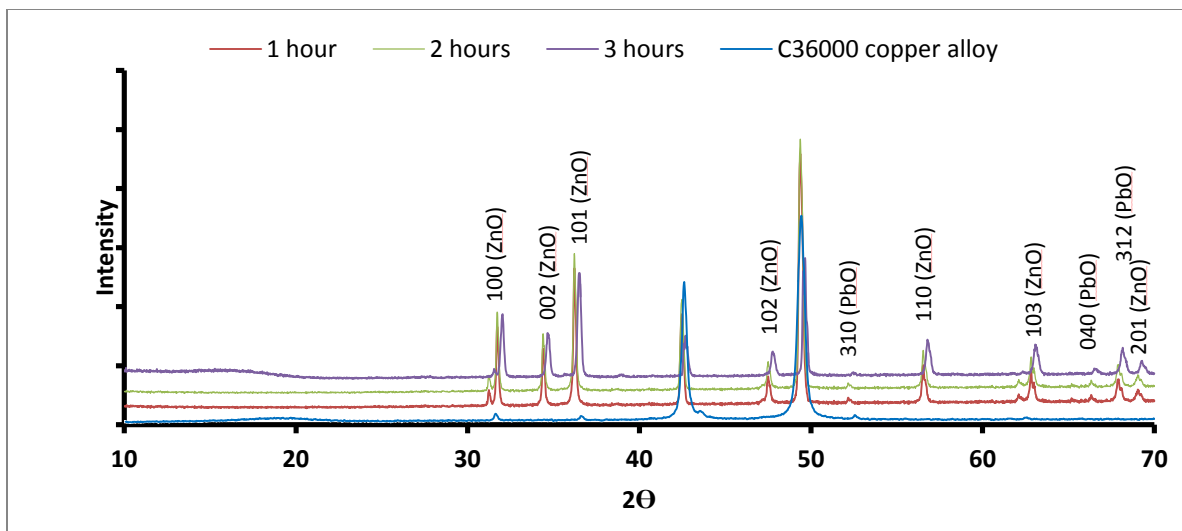


Figure 21: X-ray diffraction pattern of C36000 copper alloy thermally oxidized in N_2 -5 Wt. % O_2 .

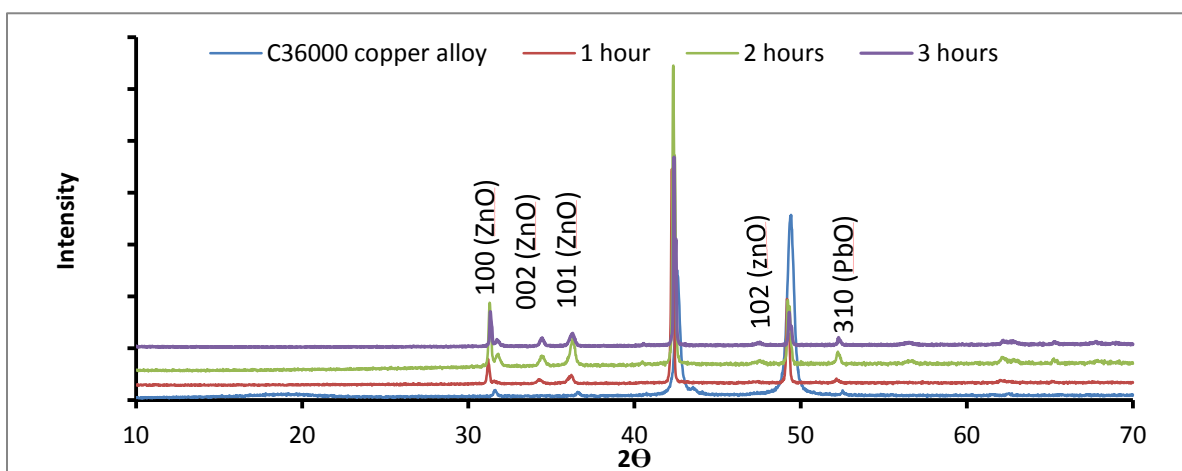
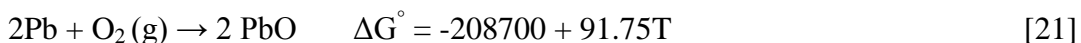
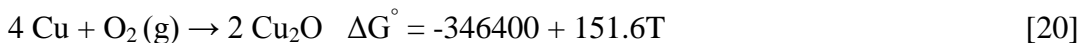
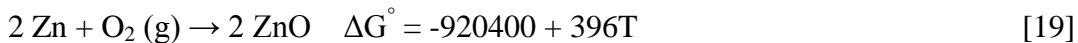


Figure 22: X-ray diffraction pattern of C36000 copper alloy thermally oxidized in N_2 -12 Wt. % O_2 .

It is noted that as the amount of oxygen in the oxidizing gas increases, the number of oxide planes diffracting the X-rays reduced. This is due to the coarsening of the oxides. The results from the X-ray diffraction studies are in agreement with the thermodynamic prediction of the oxide product formation of high temperature thermal oxidation. Since the major chemical constituents of the C36000 copper alloy are copper and zinc and very

limited amount of Pb; the expected reactions from a thermodynamic standpoint with standard Gibbs free energies, ΔG^0 are ⁷⁷:



From the Cu-O phase diagram, CuO-Cu₂O and Cu₂O-Cu phase equilibria can exist at high temperatures. However, the oxidation product is mostly ZnO. At the high temperatures of 650 °C, the Gibb's free energy of formation of ZnO is -570,563J which is more negative than the standard Gibbs free energy of formation of CuO and Cu₂O as well as PbO. Therefore, ZnO is expected as the preponderant metal oxide as confirmed from the X-ray analysis. Even if there would have been a little amount of CuO formed during the thermal oxidation, such CuO would be easily reduced to Cu by Zn (Zn + CuO → Cu+ ZnO).

6.3.2 Surface morphology examination with the Scanning electron microscope:

The surface morphologies of the C36000 copper alloys were altered by the thermal oxidation and subsequent formation of oxides examined with a scanning electron microscope.

6.3.2a Surface morphology of oxide layer after thermal oxidation at 550 °C and 650 °C in air:

The surface morphology of the C36000 copper alloy samples oxidized in air was evaluated after 4 hours of the thermal oxidation at 550 °C and 650 °C. At both 550 °C and 650 °C, the surfaces showed oxide layers due to the various oxides that have been

formed. The shapes and sizes of the oxides formed varied as seen in Figure 23. The measured average size of the oxide granules were $0.065\ \mu\text{m}$ and $0.08\ \mu\text{m}$ for the samples oxidized 550°C and 650°C respectively. These values ranged from as small as $0.04\ \mu\text{m}$ to about $0.15\ \mu\text{m}$ in both cases. The oxide granules were nearly spherical in shape and conglomerated together. The oxide layer formed was contorted due to the difference in the thermal behavior of the C36000 copper alloy substrate and the oxides formed.

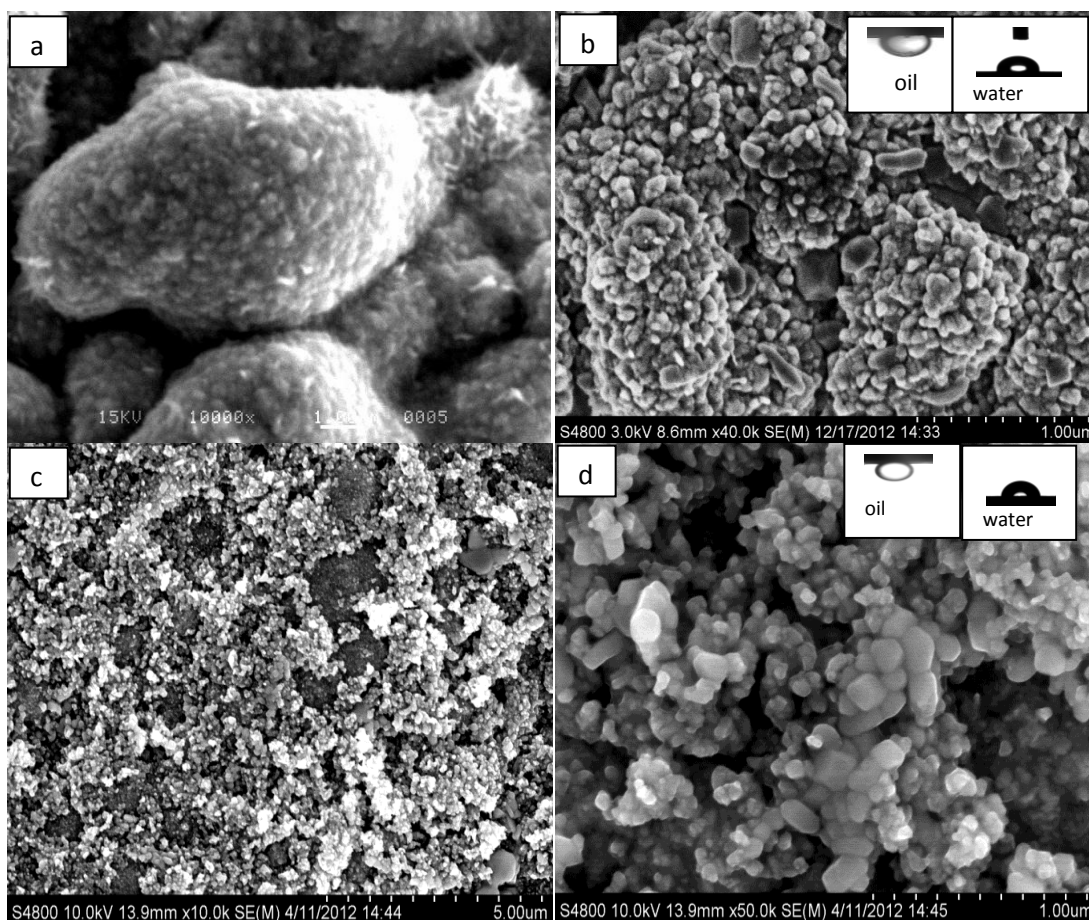


Figure 23: SEM of thermally oxidized C36000 for 4hours at 550°C and 650°C in air. [a and b] 550°C [c and d] 650°C .

6.3.2b Surface morphology of oxide layer after thermal oxidation at 550°C and 650°C in N_2 -0.75 Wt. % O_2 , N_2 -5 Wt. % O_2 and N_2 -12 Wt. % O_2 gas mixtures:

The SEM images in figures 24, 25 and 26 of the C36000 copper alloys revealed distinctly different surface morphologies which included oxide nanowires as well as convoluted

oxide layer after oxidation in the above stated N_2 - O_2 gas mixtures at $650^\circ C$. It is known that metal oxide nanowires grow only within a certain window of time and temperature during the thermal oxidation of copper alloy substrates⁷⁸. Spalling of the oxide layer from the C36000 copper alloy substrate at the metal oxide-C36000 copper alloy interface was not observed at any of the temperatures used in this process.

The morphologies of the oxide nanowires formed changed with the thermal oxidation conditions, in terms of their length and diameter of their cross sectional areas. However, no nanowires were formed after thermal oxidation for 2 and 3 hours in N_2 -0.75 wt. % O_2 ; after thermal oxidation for 1 hour in N_2 -5 wt. % O_2 and after 3 hours in N_2 -12 wt. % O_2 . From the SEM images in figures 23, 24 and 25, oxide nanowires were found to grow randomly on the convoluted oxide layer within specific time periods of 1 during the thermal oxidation of the C36000 in N_2 -12 wt. % O_2 , 2 and 3 hours during the thermal oxidation of the C36000 copper alloy in N_2 -5 wt. % O_2 gaseous atmosphere and at 1 and 2 hours in N_2 -12 wt. % O_2 gaseous atmosphere respectively.

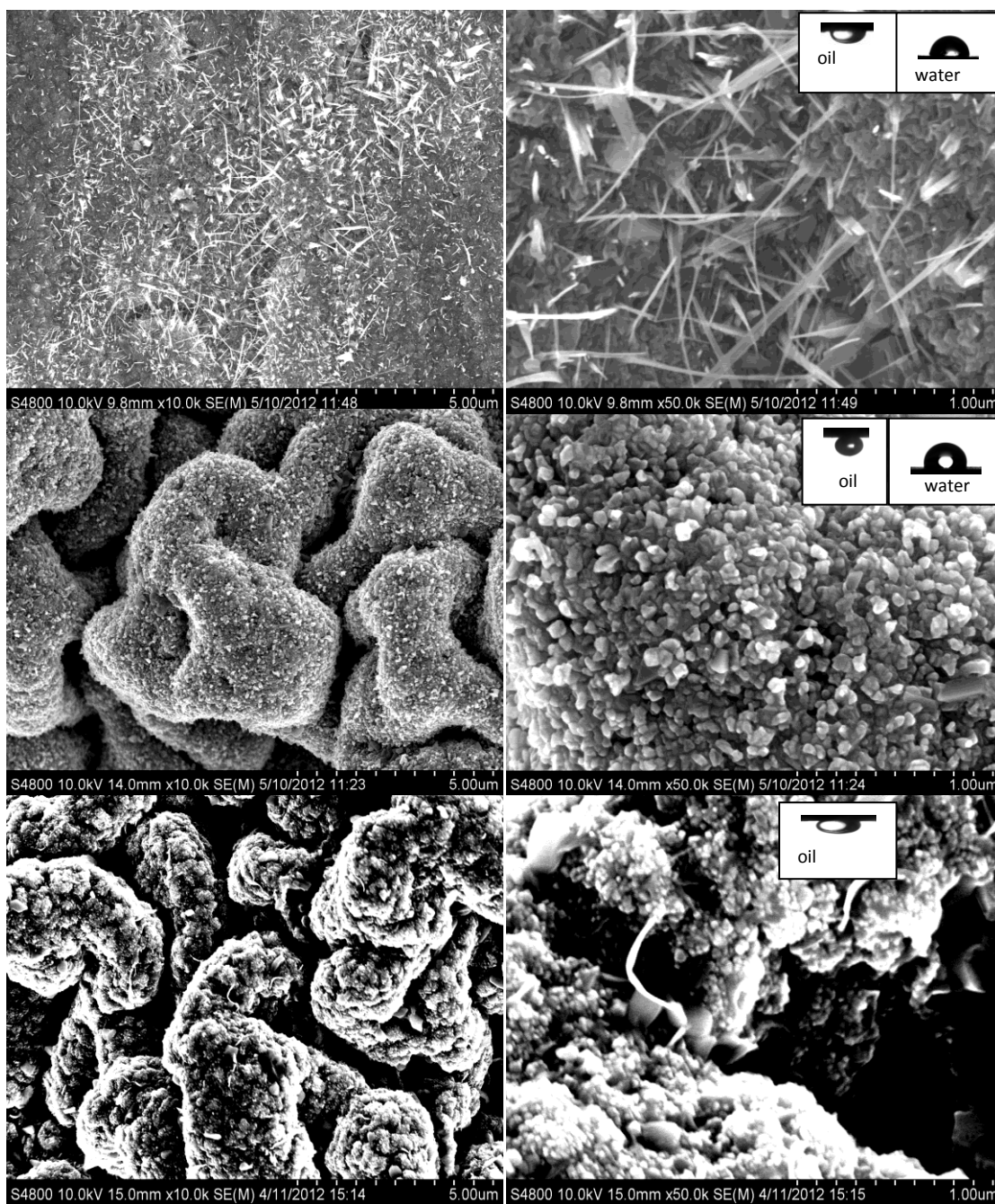


Figure 24: SEM images of thermally oxidized C36000 copper alloy samples in N_2 -0.75 Wt. % O_2 showing oxide layer convolution and ZnO nanowire growth at $650^\circ C$. (1) SEM for 1 hour in N_2 -0.75 Wt. % O_2 (2) SEM for 2 hours in N_2 -0.75 Wt. % O_2 (3) SEM for 3 hours in N_2 -0.75 Wt. % O_2 . Images 1, 2, 3 are at 10 000x and 1a, 2a, 3a are at 50 000x

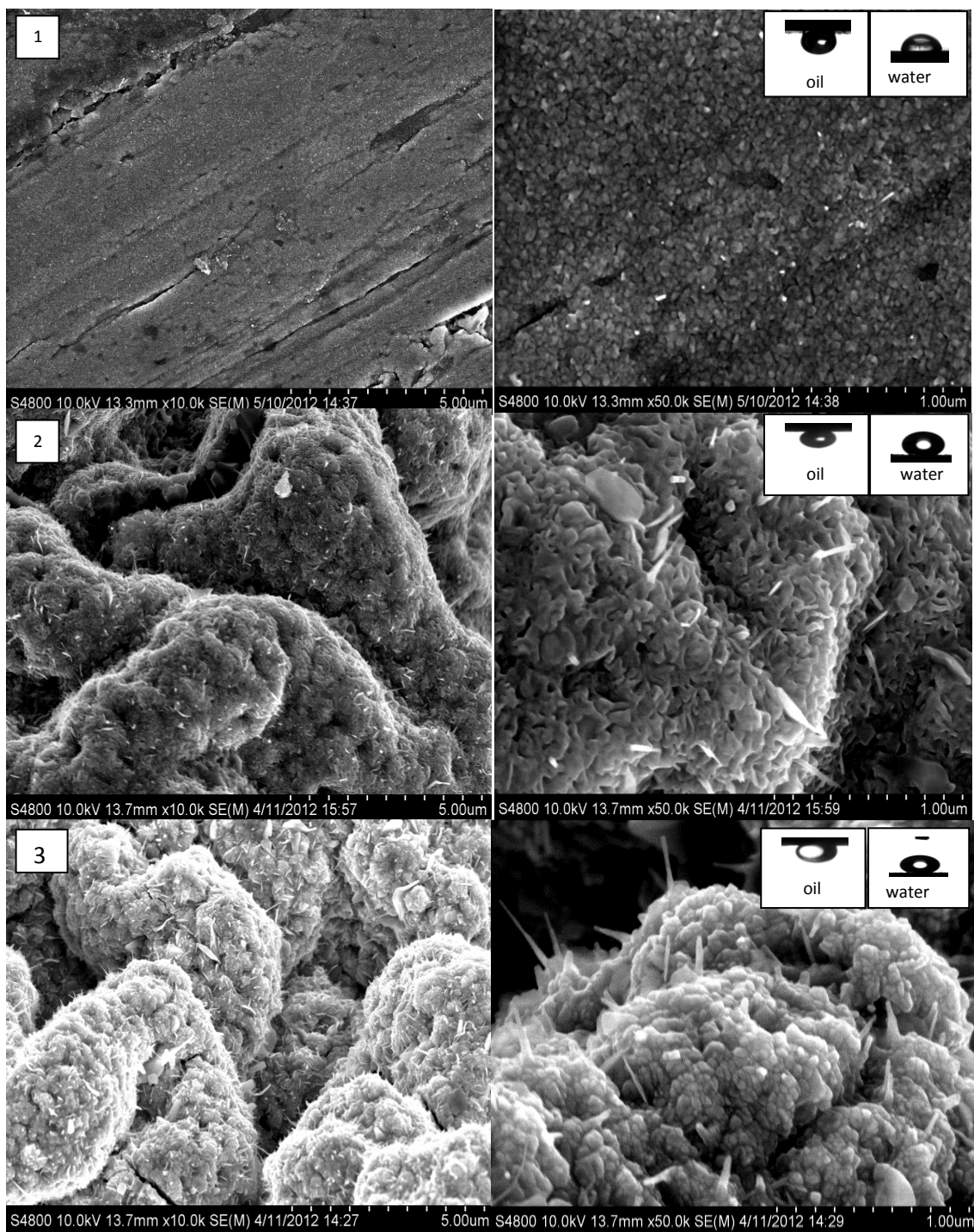


Figure 25: SEM images of thermally oxidized C36000 copper alloy samples in N_2 -5 Wt. % O_2 showing oxide layer convolvement and ZnO nanowire growth at $650^\circ C$. (1) SEM for 1 hour in N_2 -5 Wt. % O_2 (2) SEM for 2 hours in N_2 -5 Wt. % O_2 (3) SEM for 3 hours in N_2 -12 Wt. % O_2 . Images 1, 2, 3 are at 10 000x and 1a, 2a, 3a are at 50 000x

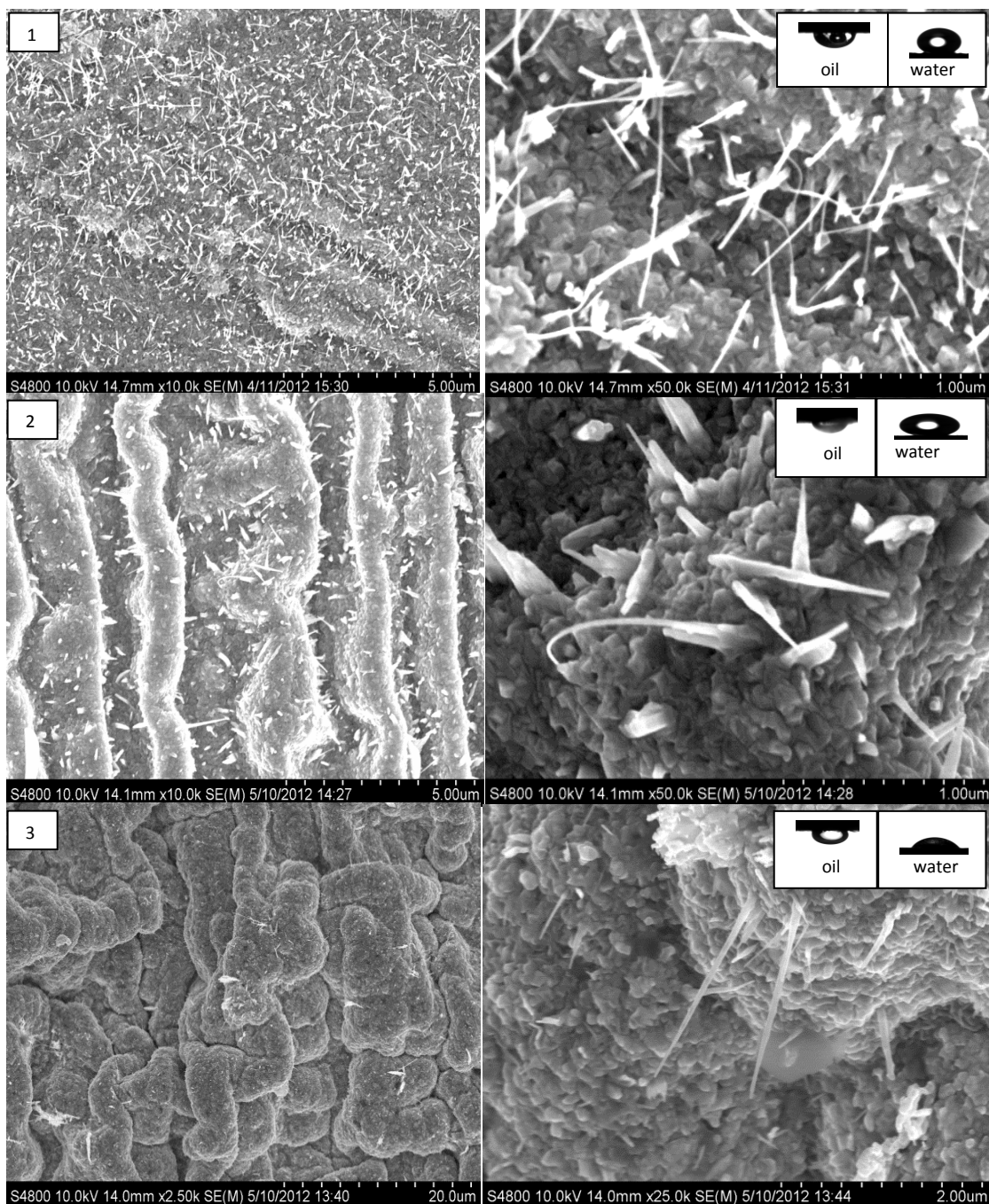


Figure 26: SEM images of thermally oxidized C36000 copper alloy samples in N_2 -12 Wt. % O_2 showing oxide layer convolution and ZnO nanowire growth at $650^\circ C$ (1) SEM for 1 hour in N_2 -12 Wt. % O_2 (2) SEM for 2 hours in N_2 -12 Wt. % O_2 . (3) SEM for 3 hours in N_2 -12 Wt. % O_2 . Images 1, 2, 3 are at 10 000x and 1a, 2a, 3a are at 50 000x

From the SEM images of these figures, the thermal oxidation of the C36000 copper alloy resulted in the growth of a substantial layer of the oxides which exhibits convolution. The observed convolution of the oxide layers are as a result of substantial stress build-up in the substrate and the growth of the oxide layer during the thermal oxidation in the various oxidizing atmospheres used. Such stresses exist at the metal oxide interfaces due to differences in their crystallographic structures, molar volumes as well as densities⁷⁹. This volume differences between the oxide formed and the consumed metal can be described by the Pilling-Bedworth ratio (PBR)⁸⁰. The PBR value is within the 1.54-1.57 range for a typical Cu-Zn alloy⁸¹ implying that there are differences in the molar volumes of the oxides formed and the C36000 copper alloy substrate.

6.4 Chemical composition of the oxide nanowires:

The chemical composition of the nanowire was determined through the energy dispersive x-ray spot analysis of the nanowires, which is stated in figure 27. The elemental composition revealed that the nanowires were composed of basically zinc and oxygen in weight percentage composition that confirms them to be zinc oxide. The average weight percentage of zinc in the nanowire is 80.47 wt.-% while that of oxygen is 19.53 wt.-%, confirming a ZnO composition.

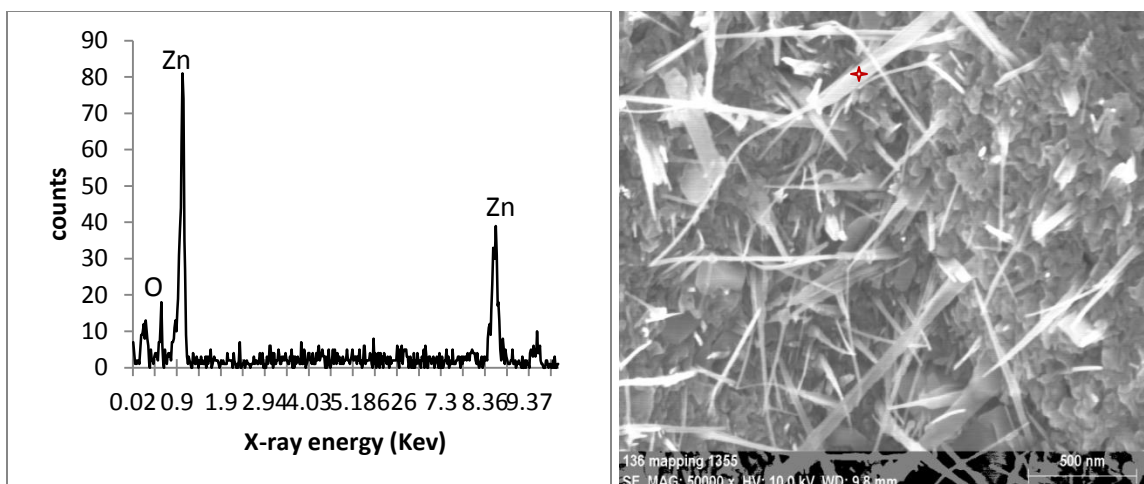


Figure 27: EDX spectrum showing composition of oxide nanowire.

6.5 Mechanism of growth of ZnO nanowires and the oxide layer:

At the reaction temperatures used for the thermal oxidation process (550 °C and 650 °C), the copper in the C36000 alloy and the alloy itself exist in the solid state. However, the lead and the Zinc are in a liquid form, with their vapour pressure increasing with the temperature used.

Therefore on the thermal oxidation of C36000 copper alloys in air and in the N₂-O₂ gas mixtures, the lead and then the zinc species in the alloy melts, segregates and diffuses towards the surface via the grain boundaries. Since the lead species have the lowest melting point, there would diffuse first followed by the zinc species. At the surface, these molten lead and zinc are oxidized by the oxygen in the gas mixture thereby forming the thin oxide layer consisting of the lead oxide and zinc oxide. This thin oxide layer further grows as this diffusion driven thermal oxidation process continues.

From the SEM images of the morphologies of the oxidation products show that the formation of ZnO nanowires relates to the convoluted oxide layer. The melting point of C36000 alloy is 890 °C and that of ZnO, which is the continuous oxide phase of the

oxide layer formed, is 1975 °C respectively. This implies that the C36000 substrate will deform more easily than the layer composed of the ZnO and PbO. However, since the thickness of the oxide layer is thinner than that of the alloy substrate, the plastic deformation may occur in the oxide layer. The plastic deformation in the oxide layer that is under compressive growth stresses results in the convolution of the oxide layer. The increase in density of dislocations in the oxide scale due to the plastic deformation results in the formation of the ZnO nanowires.

At high temperature, the kinetics of the oxidation of metals and alloys follow the parabolic law in equation 22

$$X^2 = K_p t \quad [22]$$

Where X is the oxide layer thickness and t is the oxidation time. The SEM images below show the cross-section of the oxide layer thickness and the evaluated thickness of the oxide layer are stated in Table 10.

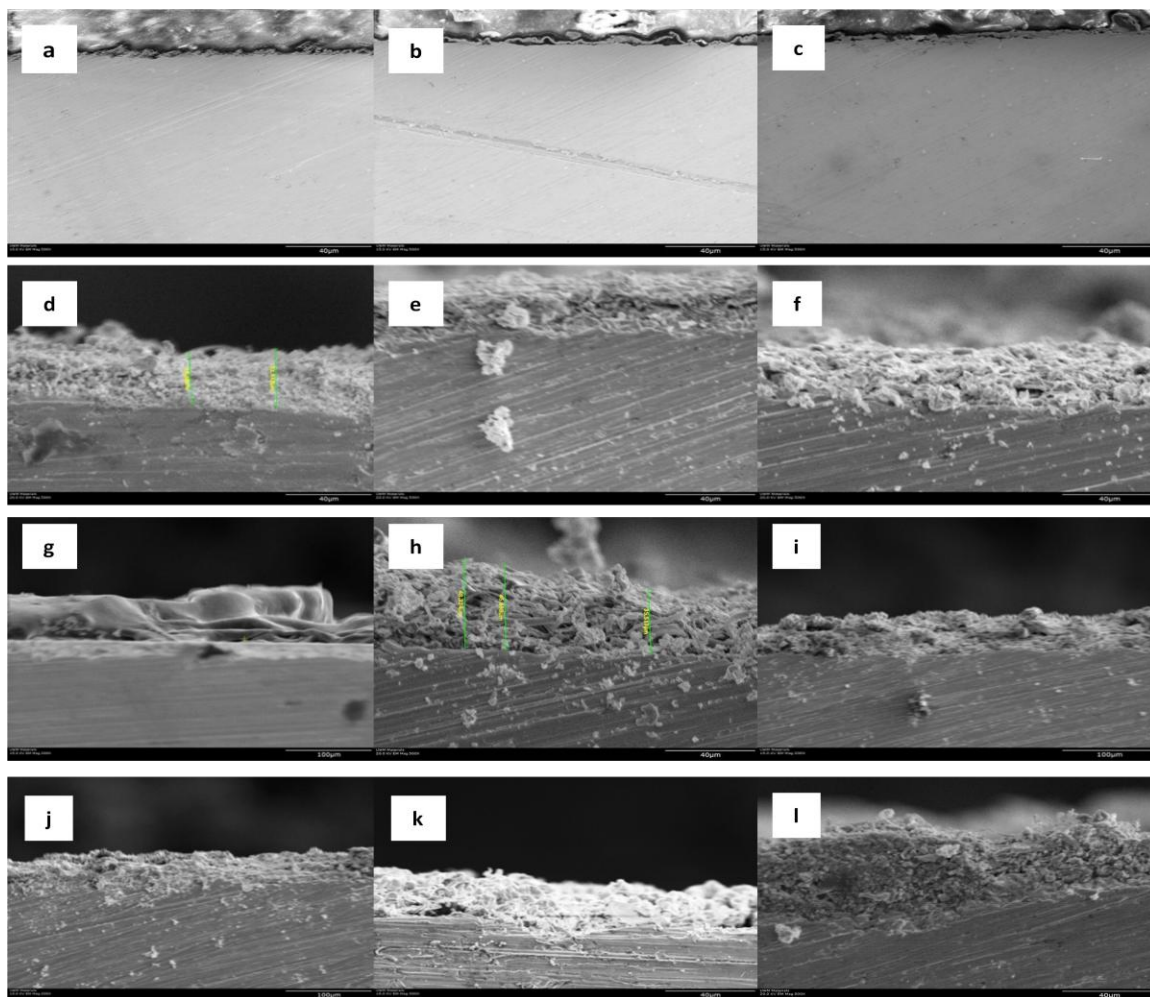


Figure 28: A cross-section showing the thickness of the oxide layer (a) 1 hour in N_2 -0.75 wt. % O_2 (b) 2 hours in N_2 -0.75 wt. % O_2 (c) 3 hours in N_2 -0.75 wt. % O_2 (d) 1 hours in N_2 -5 wt. % O_2 (e) 2 hours in N_2 -5 wt. % O_2 (f) 3 hours in N_2 -5 wt. % O_2 . (g) 1 hour in N_2 -12 wt. % O_2 (h) 2 hours in N_2 -12 wt. % O_2 (i) 3 hours in N_2 -12 wt. % O_2 (j) 1 hour in air (k) 2 hours in air (l) 3 hours in air.

The cross-sectional thickness of the oxide formed showed dependence on time, temperature and weight percentage of oxygen composition used during the thermal oxidation of the C36000 copper alloy.

Table 10: Dimensions of thickness of oxide layer of C36000 thermally oxidized in N₂-5 wt. % O₂ and N₂-12 wt. % O₂ and air at 650 °C.

Sample ID	Atmosphere	Oxidation time	Oxide layer thickness
A	N ₂ -0.75 wt. % O ₂	1	4.4±0.3
B		2	5.2±0.8
C		3	6.95±1.4
D	N ₂ -5 wt. % O ₂	1	30.3±3.1
E		2	47.7±1.7
F		3	48.3±1.9
G	N ₂ -12 wt. % O ₂	1	44.7±8.4
H		2	56.8±2.1
I		3	52.9±1.6
J	Air	1	28.3±3.5
K		2	40.2±1.9
L		3	47.7±4.6

The resulting oxidation kinetic plots for the growth of the oxide layers are shown in figure 29, for the variation of oxide layer thickness (X) with the square root of the thermal oxidation time ($t^{1/2}$) at 650 °C in air and the N₂- O₂ oxidizing gas mixtures.

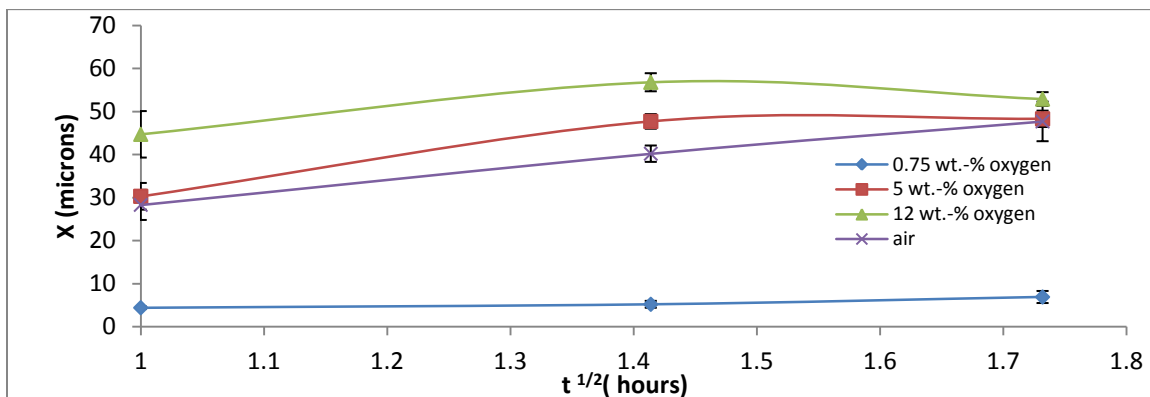


Figure 29: Plot of the square of the oxide layer thickness against oxidation time

By increasing the weight percentage of oxygen in the oxidizing medium, the rate of the oxidation process, through the growth of the oxide layer increased remarkably. However, at extensive times of oxidation, the growth of the oxide layer reduced due to reduction in the diffusion of the zinc, lead and oxygen through the oxide layer for further oxidation

From these SEM images in figures 24, 25 and 26, the values of the average lengths and diameters of the oxide nanowires can be evaluated. It is observed that an increase in the weight percentage of oxygen in the oxidizing atmosphere resulted in an increase in the average lengths and diameters of the nanowires that grew. Equally, the density of the ZnO oxide nanowires formed was found to correlate with the partial oxygen pressure used in the thermal oxidation process. Much more oxide nanowires were found to grow in N₂-12 wt. % O₂ compared to the other oxidizing gas mixtures. These changes in dimensions are simply due to the availability of more oxygen to drive the growth of the oxide nanowires. The average cross sectional thickness of the oxide layer as well as the average lengths, average cross-sectional diameters and the average distances between the oxide nanowires were evaluated using the SEM images. These dimensions of the nanowires and the thickness of the convoluted oxide layers so measured are presented in Table 11.

Table 11: Dimensions of ZnO nanowires grown on the surfaces of C36000 thermally oxidized in N₂-0.75 wt. % O₂, N₂-5 wt. % O₂ and N₂-12 wt. % O₂ at 650 °C

Sample ID	Atmosphere	Oxidation time (hrs)	Av. Diameter of nanowire (nm)	Av. Length of nanowire (μm)	Distance between nanowires (μm)
A	N ₂ -0.75 wt. % O ₂	1	34.0±0.02	0.52±0.31	0.17±0.07
B		2	-----	-----	-----
C		3	-----	-----	-----
D	N ₂ -5 wt. % O ₂	1	-----	-----	-----
E		2	27±0.01	0.20±0.04	0.23±0.09
F		3	35±0.01	0.23±0.09	0.24±0.10
G	N ₂ -12 wt. % O ₂	1	29±0.01	0.36±0.13	0.19±0.07
H		2	58±0.02	0.40±0.23	0.30±0.15
I		3	-----	-----	-----

The average diameter of the nanowires increased with increase in the time of the thermal oxidation process, for the cases in which the nanowires were found to have grown on the C36000 copper alloy samples. The average diameter of the ZnO nanowires increased from 27±0.01nm to 35±0.01nm after 2 and 3 hours of thermal oxidation in N₂-5 wt. % O₂ gas mixture respectively. In N₂-12 wt. % O₂ gas mixture, the average diameter of the ZnO nanowires increased from 29±0.01nm to 58±0.02 nm after 1 and 2 hours of thermal oxidation. To this end, the increase of about 29.63 % was observed in N₂-5 wt. % O₂ gas mixture whereas a 100% increase in the nanowire diameter was noted after just 2 hours of oxidation in N₂-12 wt. % O₂ gas mixture. Beyond the diameter, the average lengths of the nanowires also increased with the time of the thermal oxidation and the amount of oxygen used in the process. However, irrespective of the thermal oxidation condition, the oxide layers on which the ZnO nanowires grew were all convoluted.

6.6 Water Contact angle and surface roughness evaluation:

The contact angles of water measured on the surfaces of these thermally oxidized samples showed variations in values depending on the changes in the surface morphologies. The results obtained are presented in the Tables as follows:

Table 12: Contact angles of water on thermally oxidized surfaces of C36000 in air at 450 °C, 550 °C and 650 °C

Time (hrs)	450 °C			550 °C			650 °C		
	R _a	Θ _{AV}	Θ _{AV(oil)}	R _a	Θ _{AV}	Θ _{AV(oil)}	R _a	Θ _{AV}	Θ _{AV(oil)}
0	0.10	58.1°±4.9°	53.0°±1.1°	0.1	58.1°±4.9°	53.0°±1.1°	0.1	58.1°±4.9°	53.0°±1.1°
1	0.10	72.8°±2.8°	76.3°±6.3°	0.14	77.2 ⁰ ±2.8°	88.1°±11°	0.48	52.9°±2.6°	105.8°± 3.2°
2	0.10	76.2°±1.7°	71.3°±3.3°	0.20	77.6°±4.5°	72.1°±8.7°	0.52	73.0°±2.8°	97.7°± 2.1°
3	0.10	77.1°±2.8°	78.1°±11.6°	0.22	75.6°±1.6°	68.3°±5.9°	0.64	67.9°±3.1°	116.7°±4.6°
4	0.12	80.7°±2.9°	81.6°±2.9°	0.22	66.4°±1.8°	72.9°±7.4°	1.04	72.9°±2.9°	128.9°±1.9°

Table 13: Contact angles of water on thermally oxidized surfaces of C36000 in N₂- 0.75 Wt. % O₂ gas mixtures at, 550 °C and 650 °C.

Atmosphere	Oxidation time	550 °C			650 °C		
		R _a	Θ _{AV}	Θ _{AV(oil)}	R _a	Θ _{AV}	Θ _{AV(oil)}
N ₂ - 0.75wt. %O ₂	1	0.20	79.3°±7.5°	95.2°±4.4°	0.28	101.3°±9.4°	68.19°±9.7°
	2	0.35	82.9°±2.9°	97.9°±4.3°	0.42	111.7°±8.8°	106.9°±8.8°
	3	0.45	73.1°±5.1°	103.9°±0.7°	0.62	65.0°±14.1°	84.3°±9.7°

Table 14: Contact angles of water on thermally oxidized surfaces of C36000 in N₂-5Wt. % O₂ gas mixtures at, 550 °C and 650 °C.

Atmosphere	Oxidation time	550 °C			650 °C		
		R _a	Θ _{AV}	Θ _{AV(oil)}	R _a	Θ _{AV}	Θ _{AV(oil)}
N ₂ -5wt. % O ₂	1	0.34	93.6°±6.1°	95.2°±0.7°	0.34	84.6°±6.4°	91.5°±0.7°
	2	0.43	95.8°±5.9°	97.9°±4.3°	0.43	124.4°±1.5°	114.4°±4.4°
	3	0.68	82.1°±6.8°	103.9°±0.7°	0.68	115.9°±7.8°	92.8°±2.2°

Table 15: Contact angles of water on thermally oxidized surfaces of C36000 in N₂-12 Wt. % O₂ gas mixtures at, 550 °C and 650 °C.

Atmosphere	Oxidation time	550 °C			650 °C		
		R _a	Θ _{AV}	Θ _{AV} (oil)	R _a	Θ _{AV} (water)	Θ _{AV} (oil)
N ₂ -12 wt. % O ₂	1	0.40	80.0°±3.3°		0.40	132.2°±2.7°	74.0°±6.7°
	2	0.65	78.9°±4.2°		0.65	141.6°±2.5°	73.3°±0.7°
	3	0.50	86.3°±6.6°		0.50	37.6°±11.7°	101.8°±0.5°

The contact angles of water followed the Wenzel behavior for the surfaces of the C36000 copper alloys that were oxidized in air at 450 °C and 550 °C. The average surface roughness values of these samples did not change in any considerable manner as the thermal oxidation did not cause any marked formation of an oxidized surface layer. The oil contact angles recorded on these surfaces equally showed complete wetting, Wenzel behaviour. This is represented in figure 30

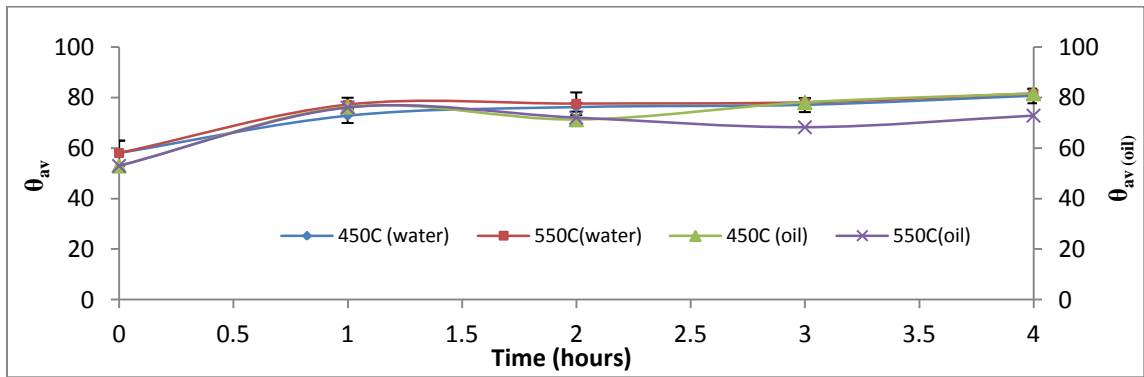


Figure 30: Plot of the contact angle of water and oil after thermal oxidation in air at 450 °C and 550 °C.

The roughness factor, R_f in the Wenzel equation is geometric factor that depends on surface roughness⁸². Therefore, the lack of change in the surface roughness due to the thinness of the melted lead/oxides on the surface, the roughness factor is approximately one ($R_f \approx 1$). The water drops and oil drops completely wetted these surfaces.

The thermal oxidation of the samples of C36000 in the air and in the different N₂-O₂ gas mixtures at 650 °C resulted in an increase in the value of the average surface roughness, R_a. Distinct high contact angles of water on the surfaces were observed after 2 and 3 hours of thermal oxidation in N₂- 5 wt%.O₂ and after 1 and 2 hours of thermal oxidation in N₂-12 wt. %.O₂.

The average roughness of the surfaces of the samples, as stated in Tables 12, 13, 14, and 15, increased with increase in the oxidation time at 650 °C. This is due to the build-up of stresses that causes the oxide layer convolution and oxidation products being more at higher thermal oxidation times and temperature. In instances where ZnO nanowires grew on the surfaces at the various times, the contact angle behaviour of water changed as the surfaces become hydrophobic. This hydrophobic behavior is attributable to the growth of ZnO nanowires combined with an increased thickness of the convoluted oxide layer. To appropriately explain these changes in the water contact angle with the growth of ZnO nanowires on oxide layer thicknesses of various dimensions, the aspect ratio, the fractional area of the ZnO nanowire surface available for the water drop are evaluated as presented in Table 16. In estimating the fractional surface, two methods were used, namely from an equation developed from a model shown in figure 31 and directly from the Cassie-Baxter model in equation 4, with the contact angle of water on a smooth, polished surface of C36000 copper alloy and with a measured average surface roughness of 0.1 microns and an average contact angle of $58.1^\circ \pm 4.9^\circ$.

Table 16: f_{sl} , aspect ratio and R_a of C36000 copper alloy thermally oxidized in N_2 -5 Wt. % O_2 and N_2 -12 Wt. % O_2 at $650^\circ C$.

Sample ID	Atmosphere	Aspect ratio (δ)	f_{sl} (calculated from (10))	f_{sw} (calculated from (4) for water)	f_{so} (calculated from (4) for oil in water)
Polished sample	No thermal oxidation	-	-	-	-
A	N_2 -0.75wt % O_2	-	-	0.50	0.89
B		-	-	0.39	0.44
C		-	-	0.88	0.68
D	N_2 -5wt % O_2	7.55	-	0.71	0.61
E		7.67	0.002	0.27	0.37
F		-	0.017	0.35	0.59
G	N_2 -12wt % O_2	5.51	0.015	0.21	0.79
H		10.63	0.038	0.14	0.80
I		-	-	-	0.49
J	Air	-	-	-	0.45
K		-	-	-	0.54
L		-	-	-	0.34

The average diameters and the average distances between the ZnO nanowires were used to estimate the water-solid fractional area, f_{sl} . The f_{sl} in this case is given by the ratio

$$f_{sl} = A_{sl}/A_{proj}. \quad [23]$$

Where A_{sl} is the area of the solid-liquid interface and $A_{proj.}$ is the projected area from which the ZnO nanowires grow. We assume that the nanowires are cylindrical with circular tips of average diameter, D and grow from a circular plane of projection of radius, X and are separated from each other by a distance of $2x$ as illustrated in figure 31.

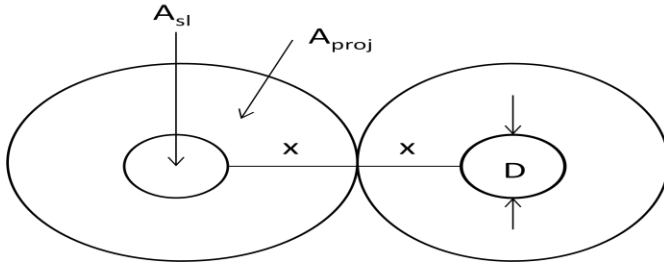


Figure 31: ZnO nanowire growing from a plane of projection of an oxide layer

Based on the ratio stated in equation 23, we have that;

$$f_{sl} = \frac{\pi\left(\frac{D}{2}\right)^2}{\pi\left[\frac{D+2X}{2}\right]^2} \quad [24]$$

$$f_{sl} = \frac{D^2}{(D+2X)^2} \quad [25]$$

Since $D + 2X$ is approximately equal to $2X$ because of the very small value of D then the f_{sl} is approximated as stated in equation 26:

$$f_{sl} = \left(\frac{D}{2X}\right)^2 \quad [26]$$

Using this expression, the calculated f_{sl} for the surfaces with the ZnO nanowires were all very low, $\ll 1$. Following equation 4, the f_{sl} values obtained for the Cassie-Baxter wetting state were greater than those calculated from equation 26. This only suggest that beyond the ZnO nanowires, the thickness of the oxide layer has contributed to the interface between the water/ drop and the solid surface.

Equally, the aspect ratios of the ZnO nanowires, ∂ , were calculated based on the relationship;

$$\theta = \frac{L}{D} \quad [29]$$

In equation 28, L is the length of the ZnO nanowire and D is the cross-sectional diameter of the ZnO nanowire. The aspect ratios increased with time of thermal oxidation as well as with the oxygen weight percent. It is also observed that the contact angles of water on the surfaces of the C36000 samples increased and saturated at the maximum aspect ratio of 10.86. The increase in the values of the aspect ratios affects the average surface roughness of the samples as it increases with increasing average surface roughness.

It is expected that increase in the surface roughness, as given by the average roughness parameter, R_a , should result in a decrease in the observed contact angle of water for a hydrophilic metallic surface⁸³. Equally, previous studies have shown that transition metal oxides are hydrophilic with contact angle less than 90° ⁸⁴. In this case however, the increase in surface roughness due to the growth of the ZnO nanowires of different aspect ratios as well as increase in the oxide layer thickness, as induced by the various atmospheres used during the thermal oxidation process were equally accompanied with an increase in the contact angles of water on the samples thermally oxidized for 2 and 3 hours in N_2 -5 Wt. % O_2 and for 1 and 2 hours in N_2 -12 Wt. % O_2 oxidation atmospheres respectively. Air trapped within the grooves of the convoluted oxide layer equally caused an increase in the air/water interface, preventing the water drops from penetrating the grooves of the oxidized surface. This shifts the behavior of the surface towards hydrophobic, non-wetting behavior and the increase in the surface roughness due to the growth of the ZnO nanowires rather than lead to a reduction in the contact angles of water accentuates them. The high contact angles observed is due to the combination of

the ZnO nanowires and the oxide layer grooves correspond to the Cassie-Baxter wetting state.

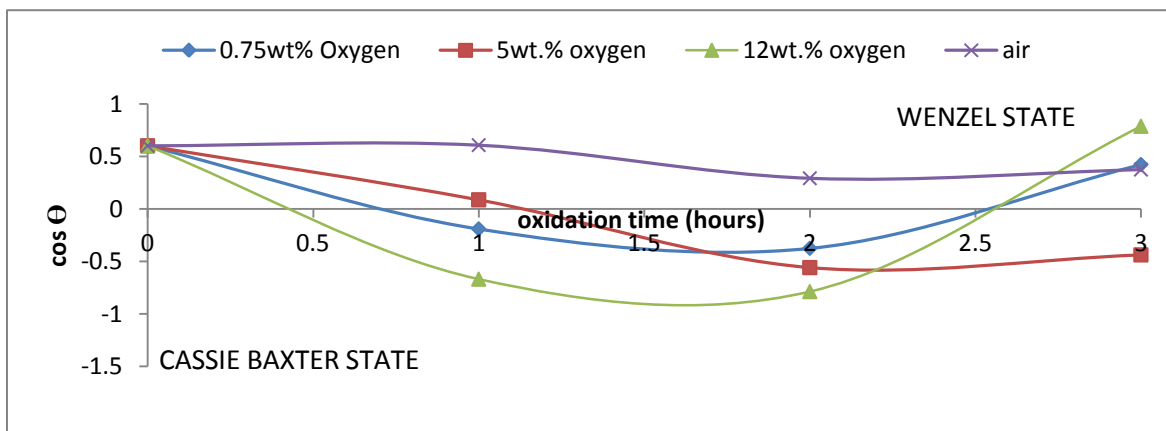


Figure 32: Plot of cosine of the contact angle of water as a function of the thermal oxidation time at 650 °C.

As can be seen in figure 32, the wetting state showed dependence on the oxidation time and by extension the thickness of the oxide layer formed as well as the presence or absence of ZnO nanowires of dimensions. To this end, the surfaces that had total absence of the ZnO nanowires, showed no hydrophobic property such as seen in samples oxidized in air. However, the growth of ZnO nanowires on the oxide layers resulted in the unique shift of the wetting behavior to high water contact angles of the Cassie-Baxter state. In the case of samples thermally oxidized in N₂-12 wt.% oxygen, contact angles as high as 142 ° was observed after 2 hours of thermal oxidation.

To further explain this shift, the values of the f_{sl} were calculated, and very low values were obtained. This implies that the fraction for the solid–water interface (f_{sl}), on the surfaces with the presence of ZnO nanowires, will be sufficiently small enough to cause a shift in the wetting behavior of the surfaces of the thermally oxidized C36000 copper alloys making them hydrophobic.

For the study of the underwater contact angle of oil, the surfaces thermally oxidized at 450 °C and 550 °C were oleophilic, in figure 30. Though the presence of oxides was detected from the XRD surfaces, the oxidized layer were thin and could not sustain oleophobicity. The changes in the surface morphology and oxide layer thickness also altered the underwater oil contact angle behavior, seen in figure 33. The surfaces became oleophobic for cases where the oxidation resulted in the growth of thick oxide layers.

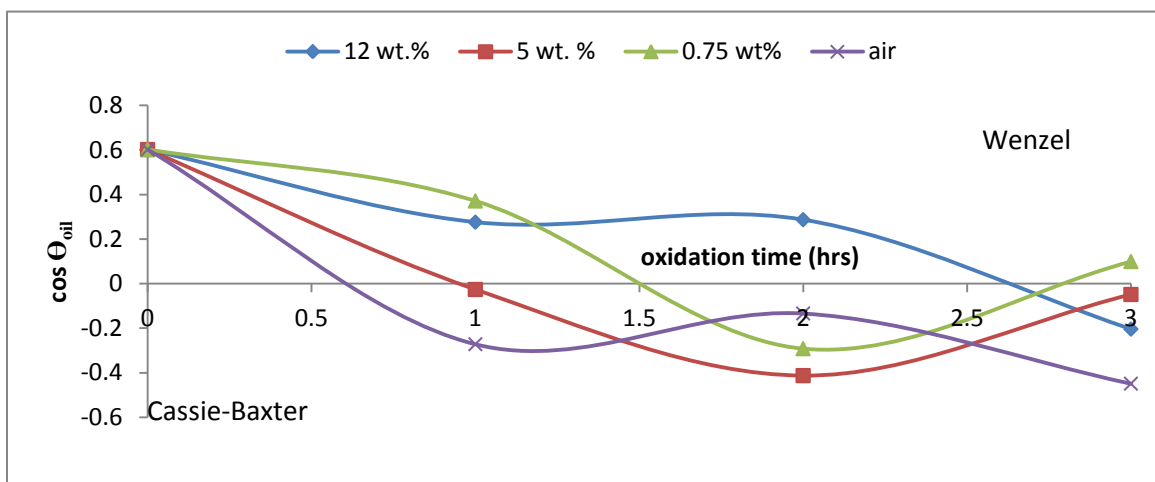


Figure 33: Plot of cosine of the underwater oil contact angle as a function of the thermal oxidation time at 650 °C.

The reason for the shift in behavior to the Cassie-Baxter wetting state lies in the ability of the convoluted oxide layer to sufficiently entrap water to sustain a Cassie-Baxter state. Therefore the samples oxidized in air showed the most oleophobicity. It should however be noted that surfaces that showed pronounced hydrophobicity were very oleophilic under water as the Cassie-Baxter state was impossible. It was impossible to create oleophobic surfaces at the solid-water-oil interface for samples with water contact angles above 130 °C.

The thermal oxidation effectively modified the surface morphology by the growth of various oxide granules and ZnO nanowires of varied dimensions. The thickness of the oxide layer equally depended on the time, temperature and the weight percentage of oxygen used in the thermal oxidation process. The high contact angle of water drops, corresponding to the Cassie-Baxter wetting state depended on the small values of f_{sw} at the solid-water-air interface due to the presence of ZnO nanowires as well as grooves in the convoluted oxide layer that can trap water. These factors were equally found to affect the contact angles of oils. The oxide layer served for the entrapment of water for a stable Cassie-Baxter state. However, the Cassie-Baxter state for oil drops at the solid-water-oil interface was not possible for surfaces that were hydrophobic with $\Theta_w > 130^\circ \text{C}$.

CHAPTER SEVEN

SUPEROLEOPHOBIC BEHAVIOUR OF THERMALLY OXIDIZED SURFACES OF C844000 COPPER ALLOY

7.0 Introduction: The C84400 copper alloy is a typical leaded brass that contains copper, tin, lead and zinc. The C84400 copper alloy, also known as the semi-red brass, is commonly used for plumbing. The microstructure of the C84400 in figure 31(a & b)] contains discrete lead particles primarily in the grain boundaries or inter-dendritic regions. This microstructure of C84400 copper alloy was equally established with an etching method as described elsewhere ⁷⁶. The optical and SEM images of the microstructure of the C84400 copper alloy is stated in figure 34 below:

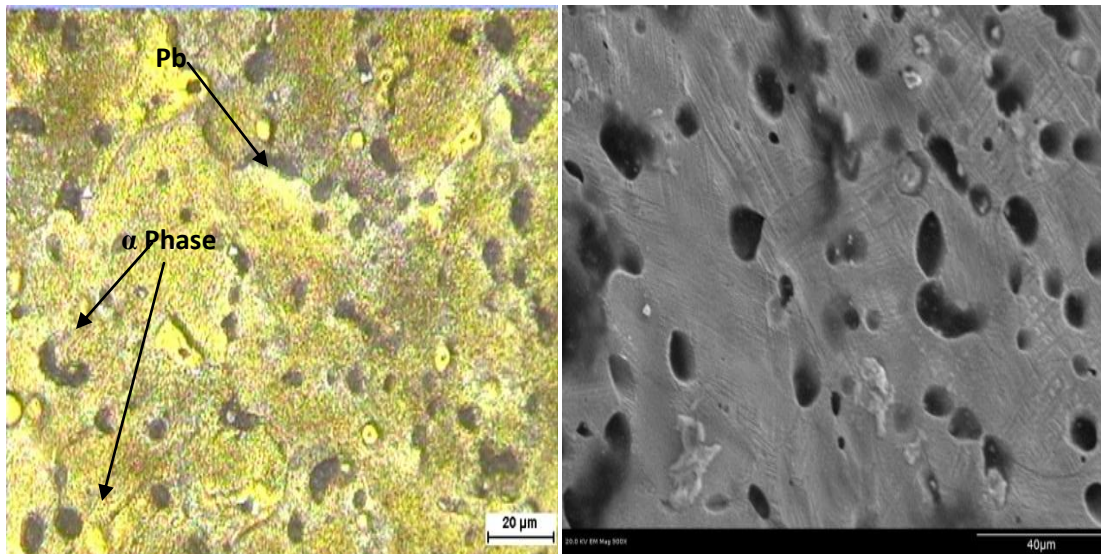


Figure 34: Optical (a) and SEM (b) micrographs of the microstructure of C84400 copper alloy

The microstructure of the C84400 consists of a single phase solid solution of alpha phase with lead particles dispersed throughout in inter-dendritic region in figure 34. The elemental composition, quantification as well as distribution within the C84400 copper alloy microstructure were evaluated.

Table 17: Elemental composition of C84400 copper alloy:

Element	Atomic %	Weight %
Copper	92.30	86.96
Zinc	4.48	4.29
Lead	2.30	7.07
Tin	0.92	1.69

Equally from the mapping of the elemental distribution, as seen in figure 35, the lead was concentrated along specific region of the microstructure while the copper, zinc and tin were all distributed within the matrix.

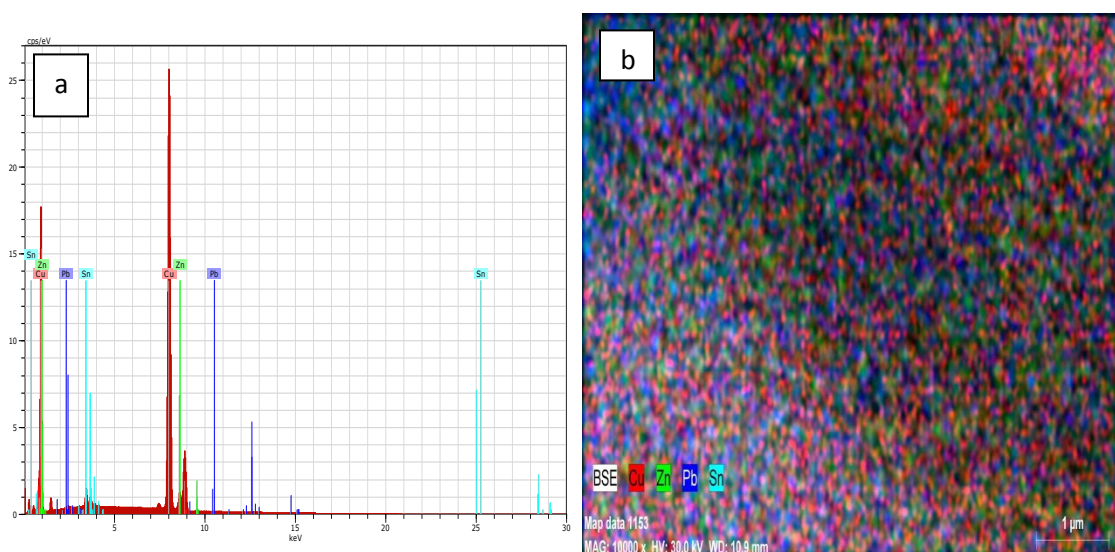


Figure 35: Energy dispersive plot (a) and the elemental mapping (b) of the microstructure of C84400 copper alloy showing elemental composition and distribution.

7.1 Experiment: The samples of the C84400 copper alloy of the dimension $2 \times 1 \times 0.5$ mm, were polished until fine surfaces were obtained. The thermal oxidation process was done in air and in various N_2 - O_2 gas mixtures, containing different amounts of oxygen. The partial pressure of oxygen is changed by using gases with different amounts of oxygen content for the thermal oxidation in closed furnace in figure 5. The furnace atmosphere is controlled by initially flowing of the gas through the furnace

chamber. The N_2 - O_2 gas mixtures used are those stated earlier in the chapter discussing the materials and methods. The controlled temperature is set at 550 °C and 650 °C and the thermal oxidation were carried out for 1 to 3 hour duration.

7.2 Characterization: The characterization included determination of the chemical composition of the oxidized sample surfaces by using the X-ray diffraction technique [XRD], with the 2000-scintag X-ray diffractometer. Further evaluation of the surface morphology of the samples was done with the Hitachi-4800 scanning electron microscope. The measurement of the contact angle for oil drops on the samples under water, with the Rame Hart 250 goniometer. The illustration of the set up for the measurement of the oil contact angles under water is shown in the illustration in figure 36. The oil contact angles under water were measured by placing the samples slightly below the surface of pure distilled water in a clean, transparent container. The drops of oil with volume of about 5 μ l were placed on the surface using a micro-syringe as shown in the illustration.

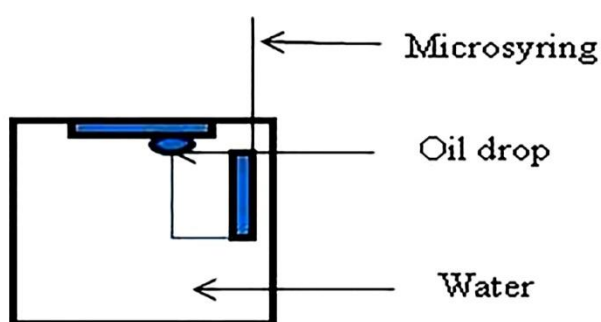


Figure 36: Experimental set up for the measurement of oil drop contact angle under water
The average surface roughness values, R_a , were evaluated with a 2-D surface profilometer, model phase II SRG-4500.

7.3 Result and Discussion:

The surface morphology, sizes of the oxide granules, chemical composition of the oxide surface layers, oxide layer thicknesses and the underwater contact angle of oil behaviour thereof on the surfaces of thermally oxidized of C84400 copper alloys are examined as follows:

7.3.1 Surface morphology evaluation with the scanning electron microscope:

The morphologies of the oxides formed after thermal oxidization of the C84400 samples at 650 °C were studied using the images obtained from the Hitachi-S4800 Scanning electron microscope. From observed morphologies, the shapes of the granules of various oxides formed were irregular in nature, due to the variations in the thermal oxidation conditions that affected the nucleation process. To this extent, the surface morphologies and the sizes of the oxide granules varied with the amount of oxygen in the N₂-O₂ gas mixtures, the time and temperature applied during the thermal oxidation process.

In the N₂-0.75 wt. % O₂ gas mixture, long oxide granules were observed on the surface after one hour of thermal oxidation, as seen in the SEM image in figure 37. Beyond these, other grains were not so well formed and defined at this time range. The EDX on these long grains showed very high weight percentage of lead with some limited amounts of zinc and copper which can be attributed to traces of ZnO and CuO formed around these long granules.

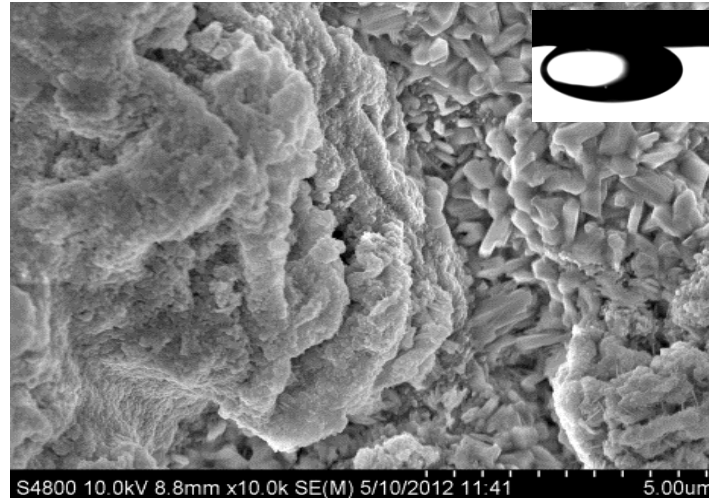


Figure 37: SEM images of thermally oxidized C84400 in N_2 -0.75 wt. % O_2 for 1 hour at $650^\circ C$. Insert is oil contact angles under water.

At two hours of thermal oxidation, the morphology of the oxidized surface layer changed; with flowery oxide features interspersed with spherically shaped oxide grains as shown in figure 38. This morphology can be understood since low oxygen partial pressure to a certain range is expected to decrease the oxide nucleation rate. Under such condition and with fewer nucleation sites, the oxide grains grow laterally into these flowery forms. The measured width of the flowery oxides formed was an average of 85 nanometers in thickness. At 3 hours of the thermal oxidation, the morphology consist oxide grains of various dimension, as shown in figure 39. An EDX study showed that the various oxidation products formed at 2 hours of the oxidation consisted of mostly zinc, lead and oxygen.

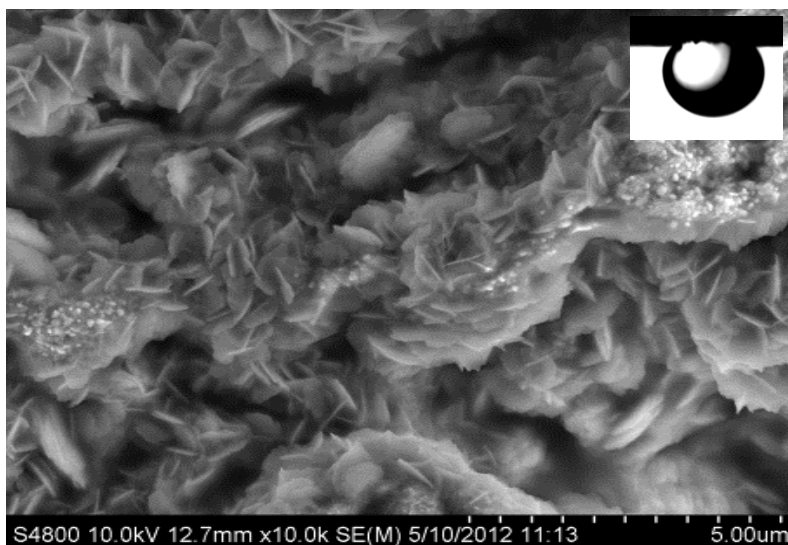


Figure 38: SEM images of thermally oxidized C84400 in N_2 -0.75 wt. % O_2 for 2 hours at 650 °C. Insert is oil contact angles under water.

More defined oxide grains were formed after the 3 hour of the thermal oxidation process, with average granule size of 110 nm. At this extended oxidation time the oxide layer clearly showed convolution of the oxide layer due to stress build up.

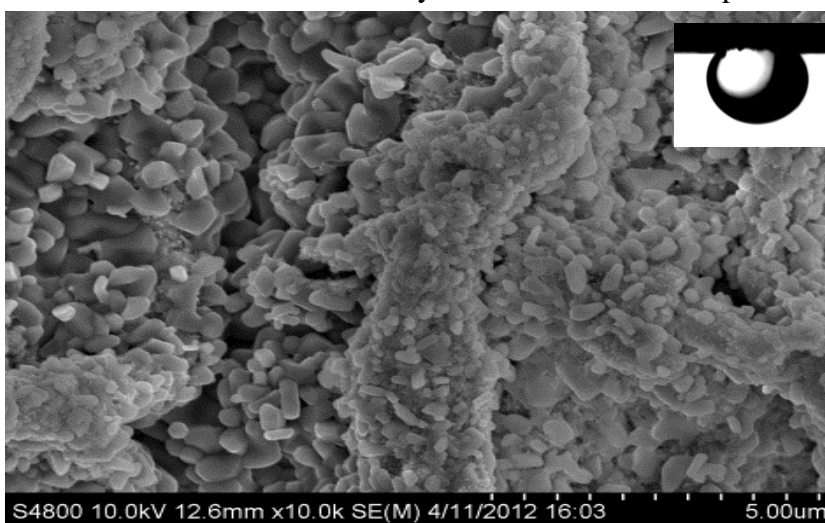


Figure 39: SEM images of thermally oxidized C84400 in N_2 -0.75 wt. % O_2 for 2 hours at 650 °C. Insert is oil contact angles under water.

In N_2 -5 wt. % O_2 , N_2 -12 wt. % O_2 , the oxide granules formed were more consistent in form and size. No unique flowery oxide morphology was formed when the amount of O_2 from the N_2 -0.75 wt. % O_2 used in the earlier case. The nature of the oxide granules

formed during thermal oxidation in these N_2 -5 wt. % O_2 and N_2 -12 wt. % O_2 gas mixtures as well as in air at 650 °C for 1 to 3 hours of thermal oxidation are shown in the SEM images in figure 40, a-c; figure 41, a-c; figure 42, a-c.

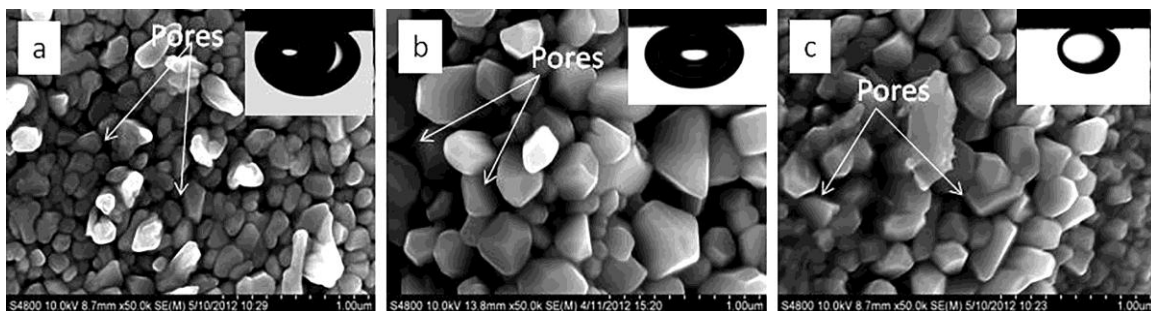


Figure 40: SEM images of thermally oxidized C84400 in different oxidizing atmospheres viz: a, b, c in N_2 -5 wt. % O_2 at 650 °C. Insert is oil contact angles under water.

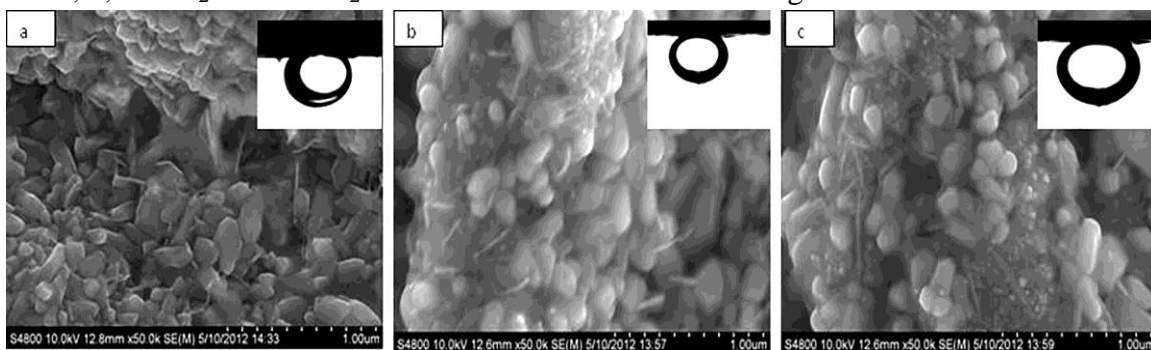


Figure 41: SEM images of thermally oxidized C84400 in different oxidizing atmospheres viz: a, b, c in N_2 -12 wt. % O_2 at 650 °C. Insert is oil contact angles under water.

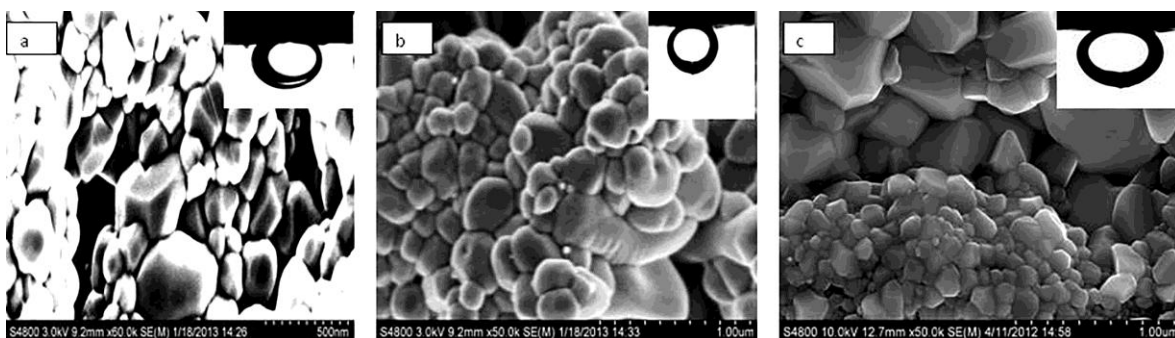


Figure 42: SEM images of thermally oxidized C84400 in different oxidizing atmospheres viz: a, b, c in air at 650 °C. Insert is oil contact angles under water.

From these SEM images, the measured average granule sizes for the oxides formed during the thermal oxidation at 650 °C are presented in the Table 18.

Table 18: Measured sizes of oxides granules on surfaces of thermally oxidized C84400 copper alloy.

Atmosphere	Oxidation time	Average granule size
N ₂ -0.75 wt.% O ₂	1	0.006-0.174
	2	0.13
	3	0.11
N ₂ -5 wt.% O ₂	1	0.134
	2	0.011
	3	0.22
N ₂ -12 wt.% O ₂	1	0.015
	2	0.030
	3	0.070
Air	1	0.23
	2	0.48
	3	0.42 ± 0.14

The average granule sizes of the oxides formed from the thermal oxidation process showed variation with changes in the amount of oxygen used in the thermal oxidation process, as seen in figure 43.

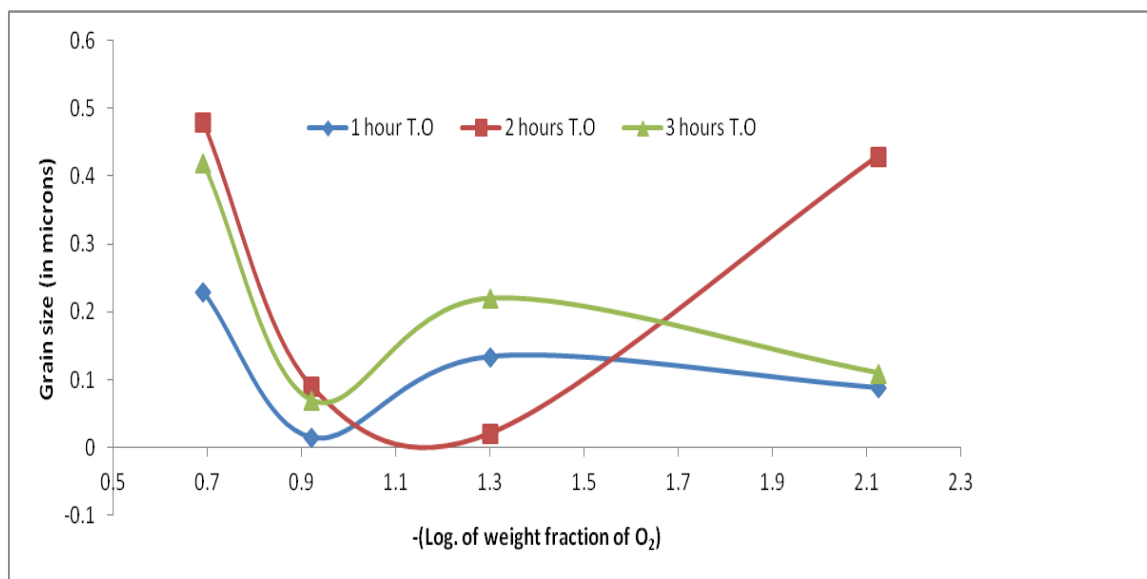


Figure 43: Plot of grain size of oxide against the negative logarithm of the weight fraction of Oxygen used in the thermal oxidation of C84400 copper alloys.

The graph shows that at early oxidation times, the estimated sizes of the oxide granules were smaller than at extensive oxidation times of 3 hours at higher oxygen partial pressures. At early oxidation times, the coarsening of the oxides is not dominant compared to the case at extensive times. Thus, the oxide granules observed after three hours of thermal oxidation in air were therefore larger than those at early stages due the coarsening of the granules.

7.3.2 Oxide layer thickness and mechanism of growth:

The cross-sectional thicknesses of the oxide layers grown on these substrates at 650 °C were examined with the Hitachi S-4800 scanning electron microscope; in figure 10. The well defined oxide layers for the samples that were oxidized in N₂-5 wt. % O₂, N₂-12 wt. % O₂ and air showed cracks of the layers in certain areas. These are shown in figures 44 to 47. At the high temperature of 650 °C used in the thermal oxidation, the differences in the thermal expansivities between the oxides forming in the oxide layer and the substrates resulted in stresses that led to the cracks observed as well as the cavities. Equally the observed cavities can be due to the effect of wear during polishing of the cross-sections for examination.

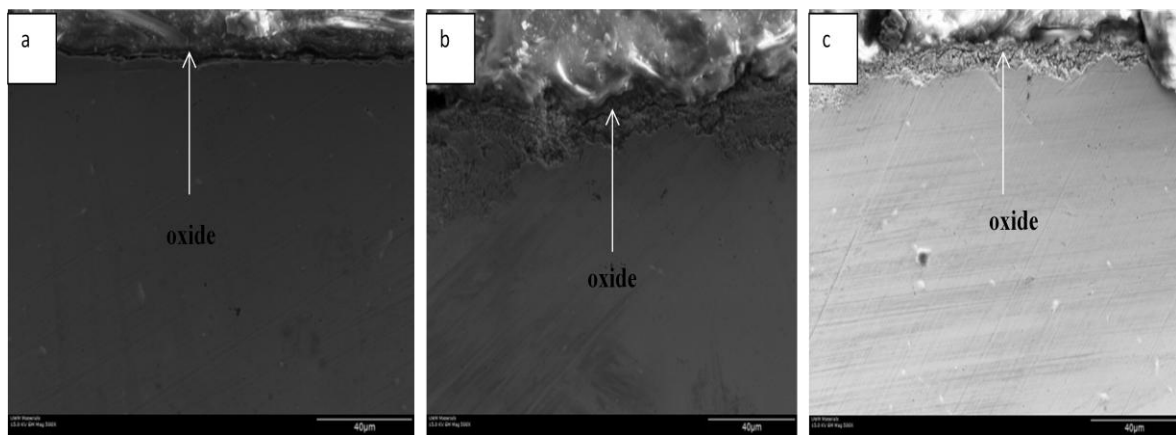


Figure 44: SEM of cross-sectional thickness of oxide layers on the thermally oxidized C84400 at 650 °C viz: a, b, c in N₂-0.75 wt. % O₂.

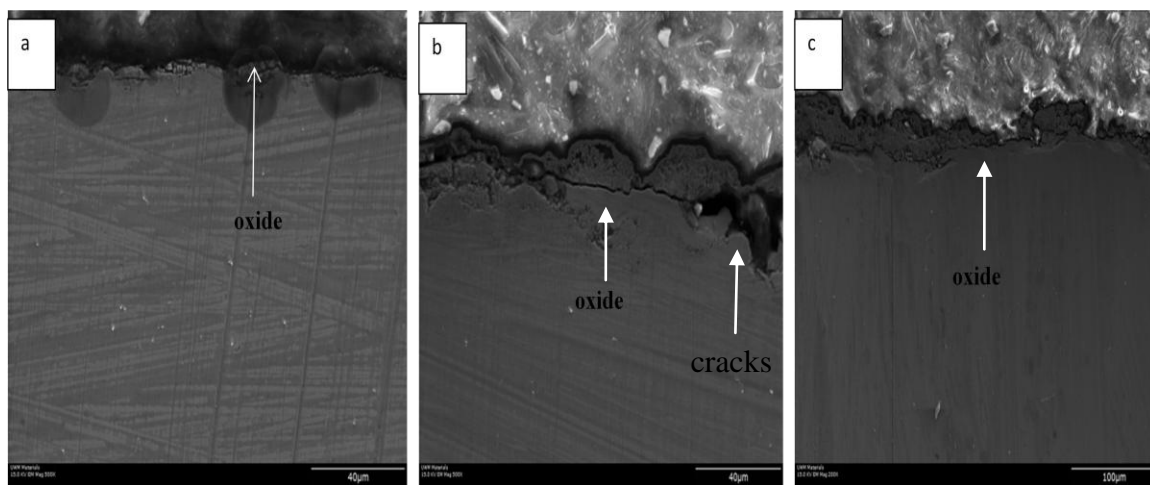


Figure 45: SEM of cross-sectional thickness of oxide layers on the thermally oxidized C84400 at 650 °C viz: a, b, c in N_2 -5 wt. % O_2 .

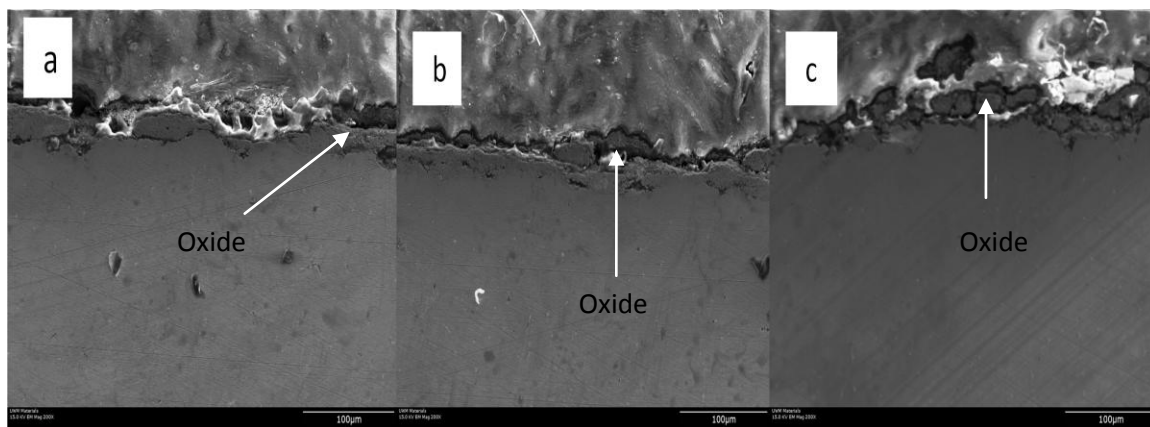


Figure 46: SEM of cross-sectional thickness of oxide layers on the thermally oxidized C84400 at 650 °C viz: a, b, c in N_2 -12 wt. % O_2 .

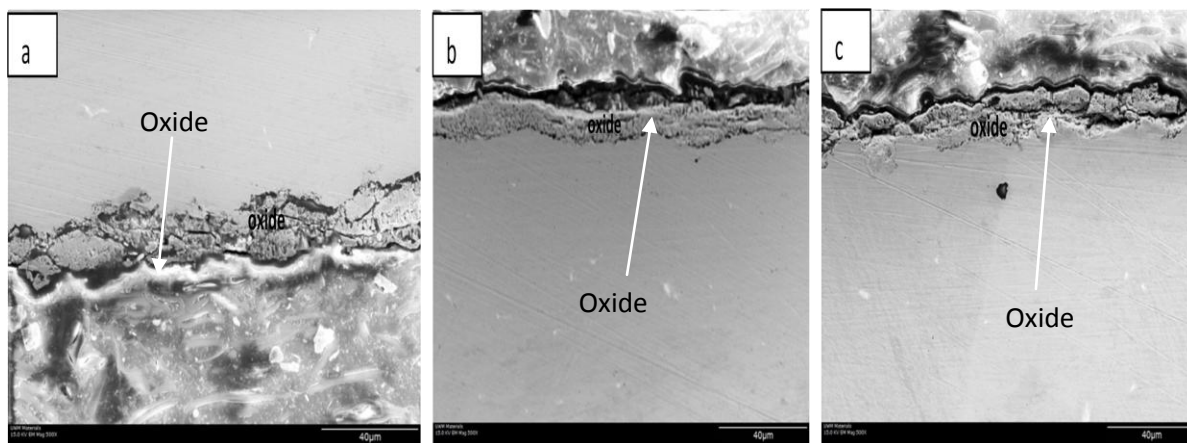


Figure 47: SEM of cross-sectional thickness of oxide layers on the thermally oxidized C84400 copper alloy at 650 °C viz: a, b, c in air.

From these SEM images, the average oxide layer thicknesses at 650 °C were measured and are presented in Table 19:

Table 19: Oxide layer thickness due to the thermal oxidation of C84400 copper alloy in the different nitrogen-oxygen gas mixtures:

Atmosphere	Oxidation time	Oxide layer thickness (μm)
N ₂ -0.75 wt.% O ₂	1	2.52 \pm 0.92
	2	11.94 \pm 3.23
	3	14.37 \pm 2.07
N ₂ -5 wt.% O ₂	1	4.38 \pm 1.63
	2	18.69 \pm 5.03
	3	25.69 \pm 9.14
N ₂ -12 wt.% O ₂	1	21.58 \pm 5.57
	2	22.13 \pm 1.76
	3	30.79 \pm 12.65
Air	1	15.56 \pm 3.38
	2	21.07 \pm 2.50
	3	21.37 \pm 1.50

The oxidation rate at which these various oxides were formed was measured as a function of the thermal oxidation time at 650 °C, based on the oxide layer thickness. The oxidation rate curves obtained on the basis of the parabolic equation, in equation 22 generated rate constants, K_p , for the process Table 20: Rate constants for the formation of the oxide layer using the parabolic law.

Table 20: Rate constants for the growth of the oxide layer

Atmosphere	N ₂ -0.75 wt.% O ₂	N ₂ -5 wt.% O ₂	N ₂ -12 wt.% O ₂	Air
Rate constant, $K_p \mu\text{m}^2\text{sec}^{-1}$	0.0003	0.0008	0.0007	0.0002

The rate of the oxidation showed increase as the weight percentage of oxygen in the N₂-O₂ oxidizing gas mixture increased. However, there is a reduction in the K_p in the samples oxidized in air. This reduction in the rate constants of the oxidation process for

the samples in air implies that though there is an initial fast growth of the oxide layer, diffusion of the reactive oxygen species through the oxide layer is severely inhibited overtime thereby reducing the overall oxidation process. The thickness of the oxide layers equally changed with the amount of oxygen in the N_2 - O_2 gas mixture. The mechanism of this kind of variation of the oxide layer thickness has already been explained elsewhere⁸⁵. The growth of the oxide layer depends on the diffusion of oxygen through the oxide layer at any given time. This diffusion of oxygen is governed by the Fick's first law. Therefore, the higher the amount of oxygen in the oxidizing media, the higher the oxygen concentration across the oxide layer and the metal alloy interface, thereby driving the growth of the oxide layer.

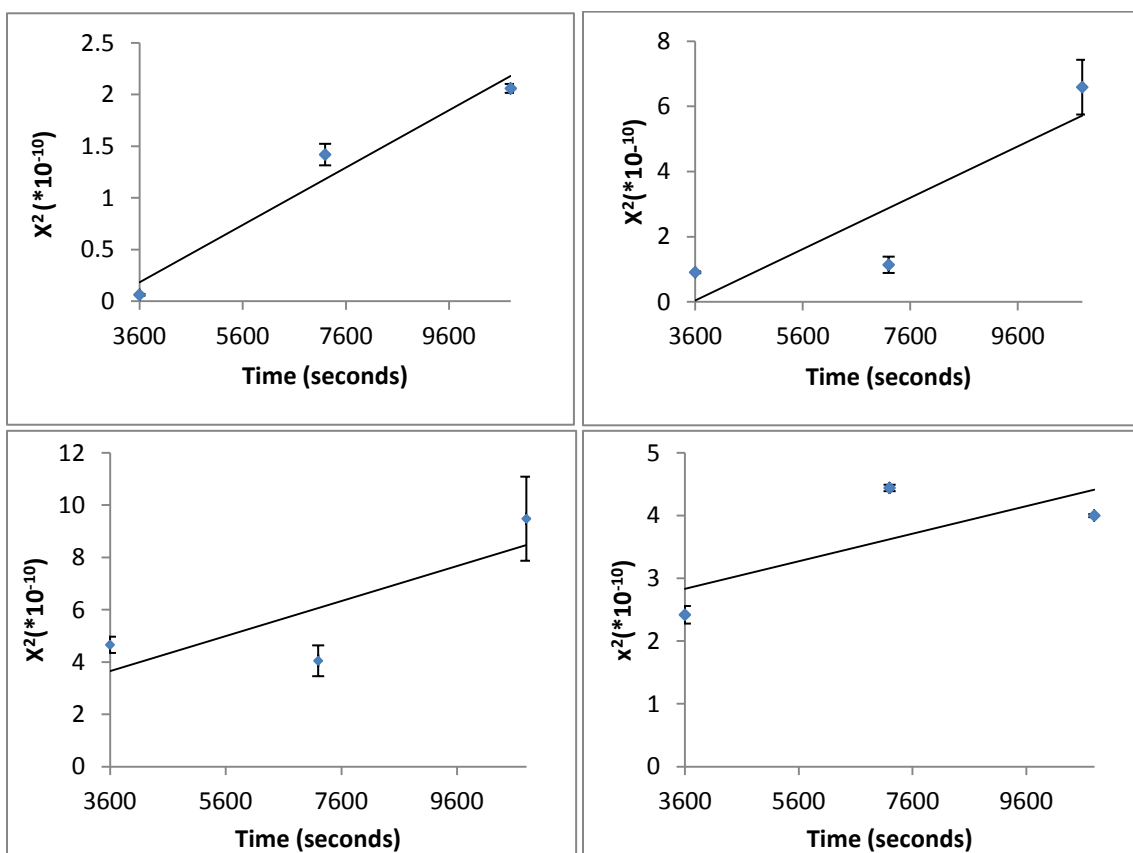


Figure 48: Parabolic plots for the determination of the rate constant, K_p , for the thermal oxidation of C84400 copper alloy samples in [a] N_2 -0.75 wt. % O_2 [b] N_2 -5 wt. % O_2 [c] N_2 -12 wt. % O_2 [d] air.

In the C84400 samples that were treated in N_2 -0.75 Wt. % O_2 , very thin oxide layer were created within the first and second hours of the process, at 650 °C. The reason for the thinness of the oxide layer lies in the negligible amount of oxygen available for oxidation of the C84400 copper alloy. However, as the oxygen weight percentage increased in the oxidizing atmosphere, the observed oxide layer thickness increased. The plot showing the oxide layer thickness as a function of the oxidation time for the different oxidizing atmospheres used in the process is shown in figure 49. In the samples oxidized in air, the oxide layer reduced in thickness after 3 hours of the thermal oxidation process. This reduction may be due to the fluffing off of some of the oxide scale after the extensive thermal oxidation at the high temperature.

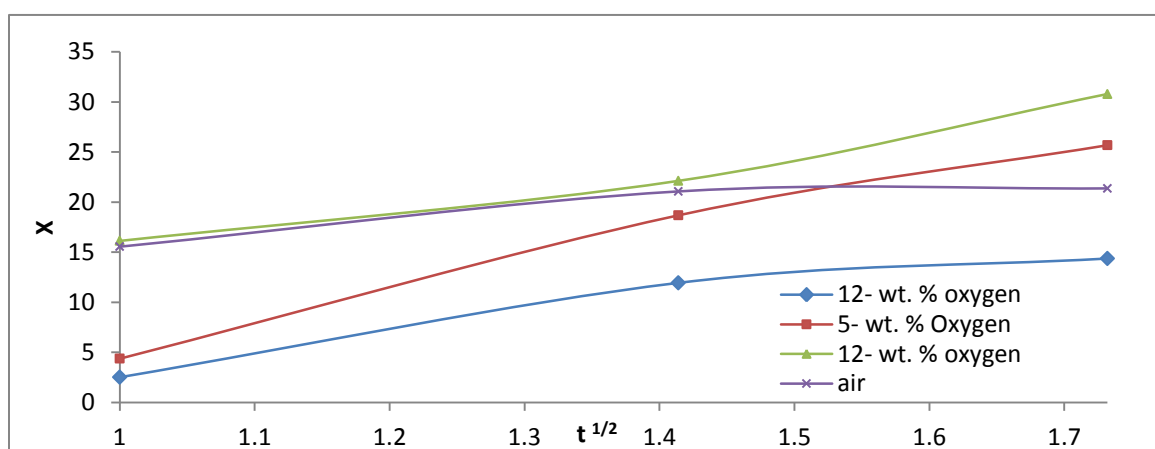


Figure 49: Plot of the oxide layer thickness against the time for thermal oxidation.

The maximum oxide layer thickness of 30.79 microns was obtained after 3 hours of thermal oxidation in N_2 -5 wt. % O_2 gas mixture.

7.3.3 Phase identification of the oxides on the surfaces of the thermally oxidized C84400 copper alloy.

X-ray diffraction with a 2θ range of 10-70° with a continuous count rate of 2 degrees per minute using the $k\alpha$ -Cu emission of wavelength of 1.54 Å was used to study the phases

of the oxides on the thermally oxidized surfaces of C84400 copper alloy samples. The XRD of the sample surfaces after thermal oxidation in air at 550 °C showed the presence of mostly PbO, in the first two hours of the oxidation process, of which the planes are as in indexed in figure 50.

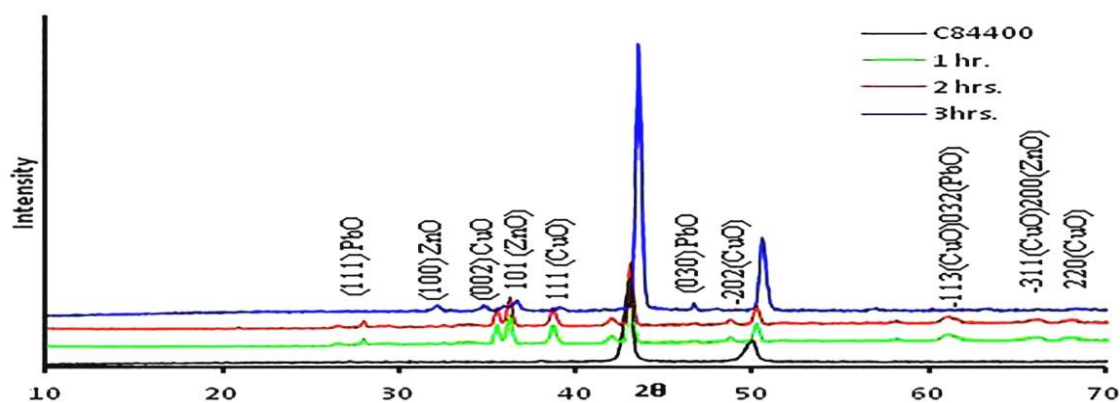


Figure 50: X-ray diffraction pattern of oxidized C84400 copper alloy in air at 550 °C.

Since Pb has a low melting point (327.5 °C), it is easily melted and oxidized at this temperature. The dominant planes of the oxides after the first two hours of the thermal oxidation in air were the (200), (002), (220), (022) and (131) planes of PbO. The X-ray diffraction also showed few diffraction planes of CuO and ZnO. However, as the oxidation was extended to the third hour, the surface oxides formed were predominated by CuO and ZnO. Equally, the phase analyses of the surfaces of the samples of the C84400 copper alloy, thermally oxidized in air at 650 °C, showed also the presence of ZnO, CuO and PbO as seen in figure 51.

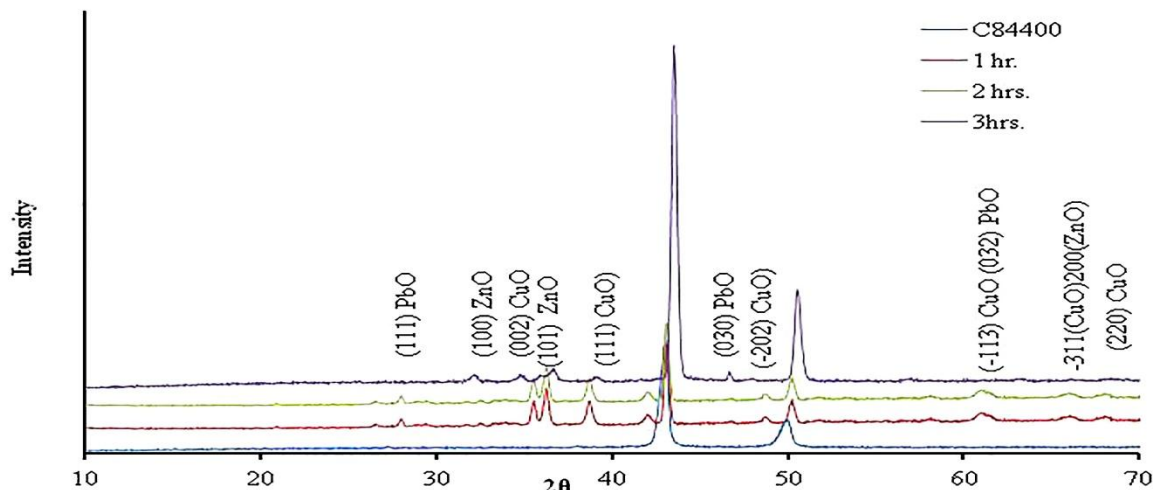


Figure 51: X-ray diffraction pattern of oxidized C84400 copper alloy in air at 650 °C.

The diffraction peaks corresponded to the (111), (-202), (002), (-113) and (-311) planes of CuO; (101), (200) planes of ZnO; (111) and (032) planes of PbO. These identified planes confirmed the presence of orthorhombic PbO, monoclinic CuO and hexagonal ZnO on the oxidized surfaces, based on PDF cards numbers 38-1477, 80-1917, and 36-1451 for PbO, CuO and ZnO respectively. Similar X-ray diffraction peaks were observed in the C84400 copper alloys oxidized in N₂-0.75 wt% O₂, N₂-5 wt. % O₂ and N₂-12 wt. % O₂ oxidizing gas mixtures at 550 °C and 650 °C as shown in figure 52.

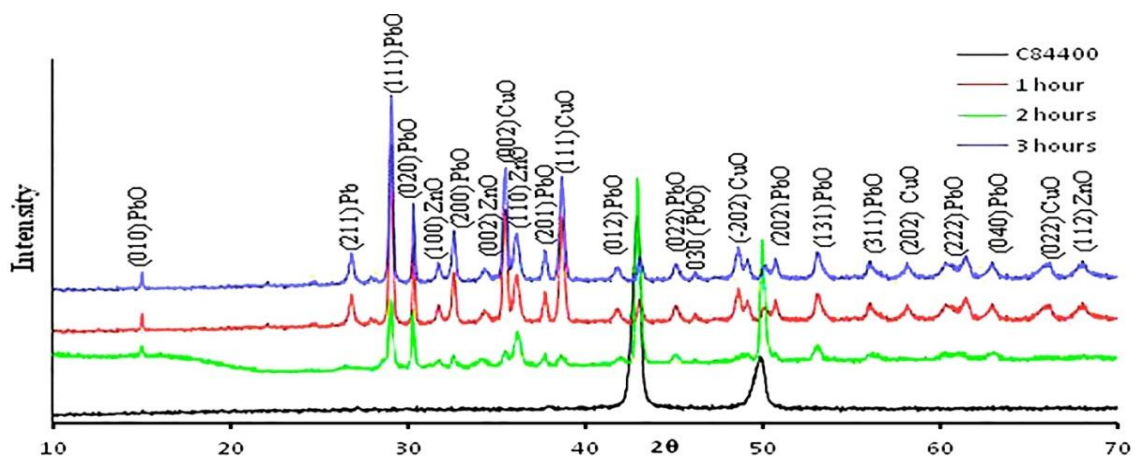


Figure 52: X-ray diffraction pattern of oxidized C84400 copper alloy in N₂-0.75 wt% O₂, N₂-5 wt.% O₂ and N₂-12 wt.% O₂ oxidizing gas mixtures at 550 °C and 650 °C.

The thermal oxidation of the samples at different temperatures, oxygen weight percentage and time implies that different crystallographic planes of oxides were formed on the surfaces of the samples which participated in the wetting behavior of the surfaces.

7.4 Underwater oil contact angle and surface roughness evaluation:

The underwater oil contact angle was evaluated on surfaces of the samples oxidized at 550 °C and 650 °C in air and in the various N₂-O₂ gas mixtures. Equally evaluated were the average surface roughness values oxidized at these temperatures. The measured values of the average surface roughness showed that the samples oxidized in air and in the different nitrogen-oxygen mixtures at 650 °C were rougher than those oxidized at 550 °C. The stresses built up at higher temperatures as well as the oxide grains formed at 650 °C resulted in higher average surface roughness values. The average surface roughness, R_a and the underwater oil contact angle on surfaces of the C84400 samples thermally oxidized at 550 °C are presented in Table 21. The surfaces oxidized at 550 °C were all oleophobic.

The surface tension of oil and other organic liquids are known to be generally lower than that of water and under water, where the solid-water-oil interface exist; the contact angle of an oil drop in such a case is given by the Young's equation⁸⁶, stated as:

$$\cos\Theta_{ow} = \frac{\gamma_{oA}\cos\Theta_o - \gamma_{wA}\cos\Theta_w}{\gamma_{ow}} \quad [31].$$

In equation 31, γ_{ow} is the surface tension at the oil water interface, γ_{oA} is the surface tension at the oil-air interface and γ_{wA} is the surface tension at the water-air interface. Θ_o and Θ_w are the contact angles of oil and water respectively on the surface of thermally oxidized sample of the C84400 copper alloy in air.

As observed in equation 31, an oleophobic surface can be created at the solid-water interface if $\gamma_{oA} \cos \Theta_o$ is less than $\gamma_{wA} \cos \Theta_w$. Since the surface tension of oil and other organic liquids is much lower than that of water, most hydrophilic, high energy oxide surfaces become oleophobic at the solid-water-oil interface due to surface tension phenomenon.

To this end, the contact angle of oil is estimated for the surfaces of the C84400 sample on the basis of equation 31. The measured values of the contact angles of oil (Θ_o) and water (Θ_w) in air were used to calculate the contact angles expected for these surfaces for oil drop of surface tension value of 27.6 mN/m ⁸⁷ (for the soybean oil used in the study), with the interfacial surface energy of water in air, γ_{wA} , equal to 73 mNm^{-1} . The calculated values of the oil contact angle on the C84400 copper alloy surfaces oxidized at 550°C were closely in agreement with experimentally obtained values. Thus, the oleophobic behavior observed at this temperature was driven by surface tension phenomenon.

Table 21: Average surface roughness and underwater oil contact angle on surfaces of C84400 copper alloy thermally oxidized at 550°C .

Atmosphere	Oxidation time	Surface roughness	Water contact angle in air	Oil contact angle in air	Underwater oil contact angle (Θ) (experimental)	Underwater oil contact angle (Θ) (calculated)
N_2 -0.75wt.% O_2	1	0.31	$76^\circ \pm 5^\circ$	$47^\circ \pm 5^\circ$	$112^\circ \pm 9^\circ$	93°
	2	0.56	$93^\circ \pm 2^\circ$	$43^\circ \pm 7^\circ$	$93^\circ \pm 8^\circ$	52°
	3	0.53	$75^\circ \pm 12^\circ$	$50^\circ \pm 4^\circ$	$91^\circ \pm 5^\circ$	90°
N_2 -5wt.% O_2	1	0.39	$79^\circ \pm 7^\circ$	$88^\circ \pm 3^\circ$	$95^\circ \pm 3^\circ$	112°
	2	0.73	$83^\circ \pm 3^\circ$	$72^\circ \pm 2^\circ$	$96^\circ \pm 2^\circ$	90°
	3	0.53	$73^\circ \pm 5^\circ$	$68^\circ \pm 5^\circ$	$102^\circ \pm 1^\circ$	106°
N_2 -12wt.% O_2	1	0.44	$79^\circ \pm 3^\circ$	$52^\circ \pm 4^\circ$	$107^\circ \pm 6^\circ$	83°
	2	0.51	$73^\circ \pm 1^\circ$	$58^\circ \pm 2^\circ$	$98^\circ \pm 4^\circ$	97°
	3	0.56	$73^\circ \pm 2^\circ$	$61^\circ \pm 4^\circ$	$94^\circ \pm 5^\circ$	105°
Air	1	0.63	$76^\circ \pm 11^\circ$	$49^\circ \pm 5^\circ$	$98^\circ \pm 3^\circ$	87°
	2	2.30	$59^\circ \pm 10^\circ$	$43^\circ \pm 7^\circ$	$110^\circ \pm 7^\circ$	123°
	3	3.41	$77^\circ \pm 2^\circ$	$56^\circ \pm 4^\circ$	$129^\circ \pm 9^\circ$	84°

However, the oil contact angles under water were very high with the exhibition of superoleophobicity on samples thermally oxidized at 650 °C as shown in Table 22. The average surface roughness and fractional surface area, f_{so} , [calculated from equation 5] of the surfaces exposed to the oil are additionally also presented in Table 22 for the C84400 samples oxidized thermally at 650 °C.

Table 22: Average surface roughness, R_a ; fractional surface area wetted by oil, f_{so} and the average contact angle of oil underwater, Θ_{av} .

Oxidizing atmosphere	Thermal Oxidation time (hrs)	Average surface roughness (R_a)	f_{so} (from Eqn. 4)	Θ_{av}
No oxidation/polished	0	0.1	-----	54.7°
N ₂ -0.75wt.% O ₂	1	1.13	0.74	109.6° ± 8.7°
	2	1.88	0.67	113.4° ± 3.9°
	3	2.15	0.58	118.6° ± 2.7°
N ₂ -5wt.% O ₂	1	0.96	0.61	116.8° ± 4.3°
	2	1.10	0.32	135.5° ± 3.5°
	3	2.08	0.11	154.4 ± 1.2
N ₂ -12wt.% O ₂	1	0.63	0.72	110.7° ± 4.7°
	2	1.24	0.48	124.9° ± 4.2°
	3	1.73	0.12	140.1° ± 2.3°
Air	1	2.0	0.39	130.8° ± 2.6°
	2	4.38	0.29	137.4° ± 3.5°
	3	3.25	0.25	140.8° ± 2.1°

Using the image processing software, image J, the presence of pores on the surfaces of the thermally oxidized samples at 650 °C were marked and the pore sizes measured. These samples with very high underwater oil contact angles showed considerable presence of pores of various sizes due to the irregular packing of the oxides of various grain sizes.

In order to explain the contact angle observed, the roughness of the surfaces with time is examined. The change of the average surface roughness was linear for the time of the thermal oxidation. This rate of change of the average surface roughness ($\Delta R/\Delta t$) for the C84400 copper alloys that were thermally oxidized in N₂-0.75 wt. % O₂ and N₂-5 wt. %

O_2 gas mixtures were low (0.61 and 0.67 microns/hour). This is to the near same sizes of the oxide grains formed after the thermal oxidation process. However, the samples that where oxidized showed a marked increase in the surface roughness as shown in the figure 53. This is due to the fact that the oxide grains formed in air where large and coarse.

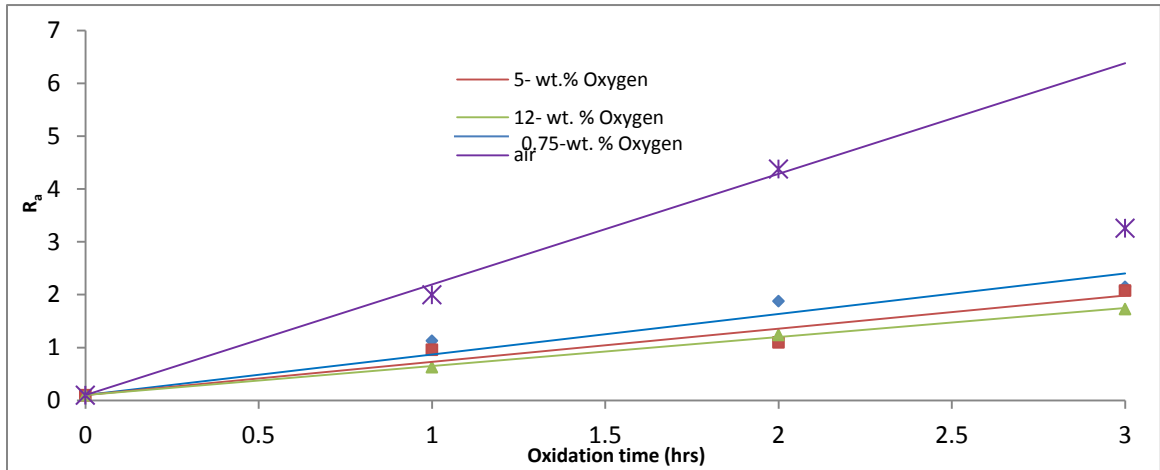


Figure 53: The variation of the average surface roughness with the thermal oxidation time a 650 °C.

From the appraisal of the surfaces, very limited number of pores were observed in the samples that were thermally oxidized in N_2 - 0.75 Wt. % O_2 as well as those oxidized in air. However beyond these rough surfaces, conspicuous pores were observed in the samples that were thermally oxidized in N_2 - 5 wt. % O_2 and N_2 - 12 wt. % O_2 gas mixtures. These pores observed in these cases are shown in figure 53-54.

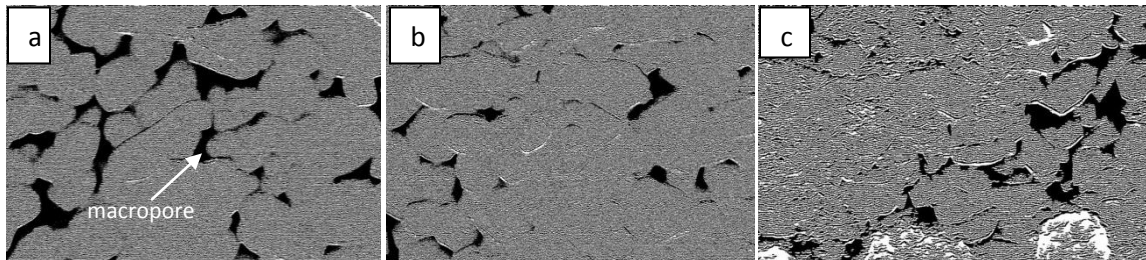


Figure 54: Process surface images of thermally oxidized C84400 copper alloy thermally oxidized in N_2 -5 wt. % O_2 at 650 °C [a. 1 hour, b. 2hours. c. 3hours].

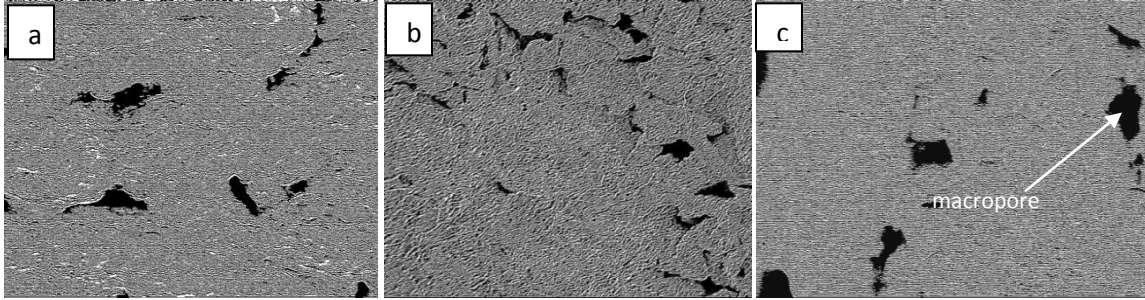


Figure 55: Process surface images of thermally oxidized C84400 copper alloy thermally oxidized in N_2 -12 wt. % O_2 at 650 °C [a. 1 hour, b. 2 hours, c. 3 hours].

The measured values of the average pore sizes imply that the pores are macro-pores⁸⁸.

In order to estimate the macro-pore volume, V_p ; the thickness of the oxide layers of the samples oxidized in the different N_2 - O_2 gas mixtures are assumed to be composed of macro-cylindrical and interconnected pores with the average pore length, h_{av} equal to the oxide layer thickness, λ . Hence, the pore volume,

$$V_p = \frac{1}{4}\pi D^2 h_{av} \quad [28]$$

$$h_{av} = \lambda, \quad [29]$$

$$V_p = \frac{1}{4}\pi D^2 \lambda \quad [30]$$

Using this relationship, the pore volumes are estimated for the oxidized surface layers, as shown in Table 23.

Table 23: Oxide layer thickness, λ ; pore size, D and estimated pore volume of C84400 copper alloy samples oxidized in N_2 -5wt.% O_2 and N_2 -12wt.% O_2 gas mixtures.

Atmosphere	Time (hrs)	oxide layer thickness	Average Pore size	Estimated Pore volume(μm^3)
N_2 -5wt.% O_2	1	4.38 ± 1.63	0.08 ± 0.03	0.27
	2	10.72 ± 5.03	0.14 ± 0.09	1.17
	3	25.69 ± 9.14	0.28 ± 0.08	5.65
N_2 -12wt.% O_2	1	21.58 ± 5.57	0.517 ± 0.13	8.81
	2	20.13 ± 7.68	0.587 ± 0.10	9.17
	3	30.19 ± 12.65	0.509 ± 0.23	12.07

The estimated pore volume is in direct proportionality with the oxide layer thickness as shown in figure 56. To this extent, there is porosity in the oxide layer based on the elaborate pores whose volume increases with the oxide layer thickness based on the increase in the pore volume observed. Thus, the presence of elaborate pores on the oxide layer of the samples treated in N₂-5 Wt. % O₂ and N₂-12 Wt. % O₂ resulted in the oxide layer porosity.

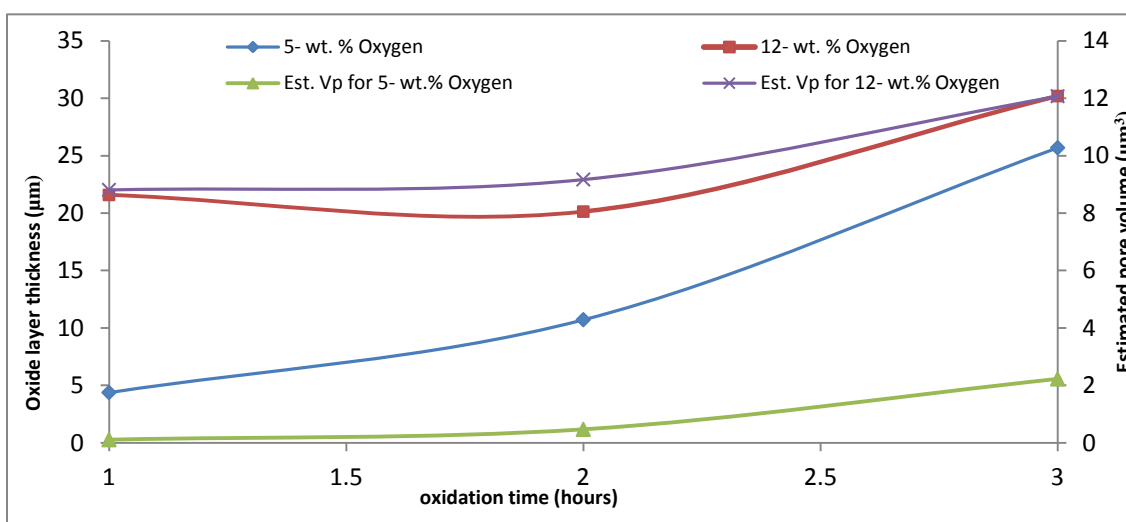


Figure 56: Plot of the oxide layer thickness and the estimated pore volume against the oxidation time (hours).

The underwater oil contact angle and the resultant superoleophobicity, with increase in the oxide layer thickness, can therefore be explained from two perspectives, namely; the surface tension of oil at the oxide-oil interface on the surfaces of the thermally oxidized C84400 alloys as well as the porosity due the macro-pores of varying pore volumes on the oxide layers.

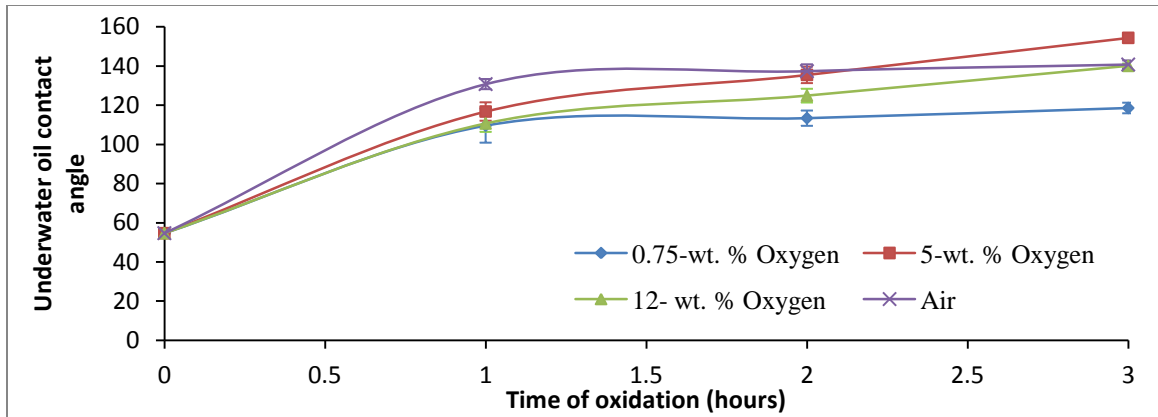


Figure 57: Plot of the underwater oil contact angle against the oxidation time at 650 °C [hours].

The porosity of the oxide layer is affected by the grain size, grain packing and the thickness of the oxide layer. The generally very small grains of the oxides formed during the thermal oxidation imply significant contribution to the surface porosity. The specific surface area [exposed grain surface area per unit solid volume] is inversely proportional to the size of the oxide granule. This indicates that when all other factors are equal, a given weight of small grains will be stabilized by higher porosities. Spontaneous invasion of water into the pores of volume, V_p ; of the porous oxide layers of the samples of the C84400 thermally oxidized in N_2 -0.75wt.% O_2 [for 3hours], N_2 -5wt.% O_2 , N_2 -12wt.% O_2 and air takes places through capillary phenomenon while the remaining water stays on the surface as a patchwork of solid and water.

The apparent contact angle of oil in this type of system under water can therefore be explained using the Cassie-Baxter model in equation 4.

$$\cos \Theta_{CB} = f_{so} (\cos \Theta_o + 1) - 1 \quad [4]$$

where f_{so} is the fraction of the solid oxide granules in contact with the oil drop in the underwater condition. This equation is used to predict increase in the underwater oil

contact angle through developed porosity that causes the trapping of water to form a cushion under the oil drop. Using equations 30 and 4, the pore volume and f_{so} are calculated and stated in Table 30. The plots of the relationship between the oxide layer thickness and the observed underwater oil contact angles as well as between V_p and the underwater oil contact angles are shown in figure 58.

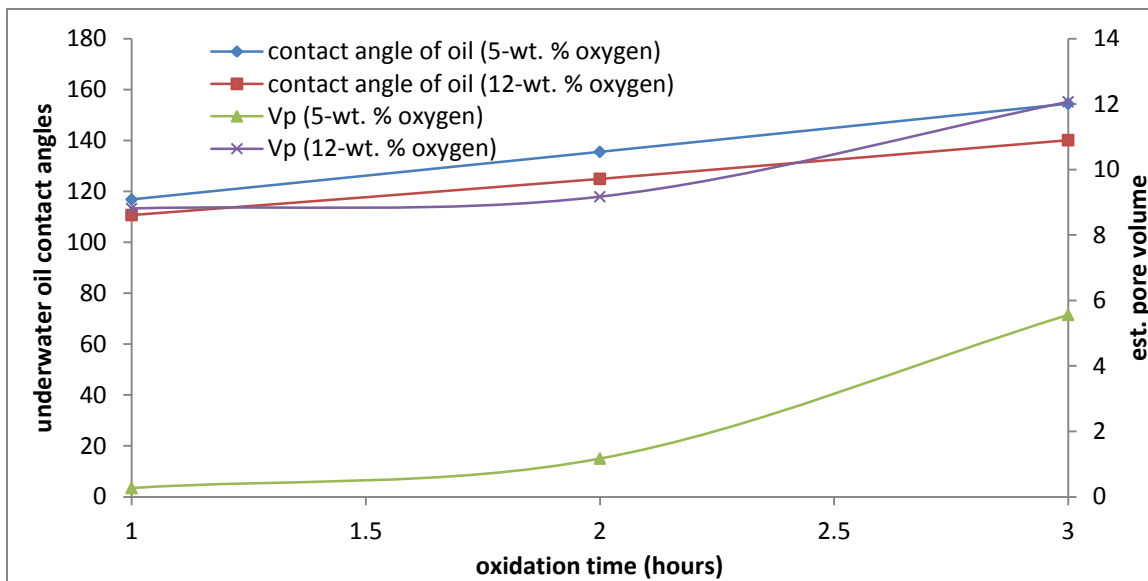


Figure 58: Plot of the underwater oil contact angle and the estimated pore volume with the oxidation time.

It is observed that as the pore size, D and the pore volume, V_p , of the oxide layer increases, the fractional area of the solid wetted by oil, f_{so} reduces. The implication of this is that the increase in D as well as V_p conveys porosity on the oxide layer and as such water is trapped more easily and effectively under the oil drop. This induces the observed superoleophobicity. The superoleophobicity is therefore achieved by a combination of the surface tension effect of the high energy oxides formed and the presence of pores inducing in the porous oxide layer generated that effectively traps water for the underwater Cassie-Baxter state to develop.

CHAPTER EIGHT

SUPERHYDROPHOBICITY OF C36000 AND C84400 GENERATED BY THE THERMO-CHEMICAL TREATMENT WITH STEARIC AND ARACHIDIC ACIDS.

8.0 Introduction: A thermo-chemical process is a chemical reaction process that involves the application and evolution of heat. In this case, the thermo-chemical process of generating superhydrophobic surfaces involves the reaction of thermal oxidation products on the surfaces of C36000 and C84400 copper alloys with stearic and arachidic acids at temperatures above the room temperature. The thermal oxidation process was used as a surface engineering technique to create surfaces of oxides with different morphologies and sizes which were further reacted with STA or ARA to generate a hierarchical rough surface for superhydrophobicity.

8.1 Experimental approach:

8.1.1 Materials: The C36000 and C84400 copper alloys were used in the experiments and were obtained from Baker Manufacturing, LLC [Evansville, WI] and have the chemical composition earlier stated in Table 1 and 2. The reagents used include ethanol solution, stearic acid and arachidic acid, both obtained from Aldrich chemicals. All the reagents were used without further purification. For the thermal oxidation process, an electric furnace was used while the parr pressure reaction apparatus (model no. 4601Q), was used to conduct the reaction of the oxides on the thermally oxidized C36000 and C84400 samples with solutions stearic acid and arachidic acid respectively.

8.1.2 Preparation of superhydrophobic surface: The C36000 and C84400 copper alloy samples of 2×1×0.5 mm in dimension, were polished until a fine surface was obtained by

using 1200 grit sandpaper and 0.1 μ m alumina. The polished samples were washed promptly in ethanol and de-ionized water to remove dirt from the surfaces.

The next step involved the thermal oxidation of the polished sample. The process of the thermal oxidation was carried out in a furnace at 650 °C for 4 hours. The oxidized samples were then allowed to cool outside the furnace, in ambient conditions. These thermally oxidized samples were chemically reacted in pressure reaction apparatus containing 0.005M of stearic acid / arachidic acid in 500ml of ethanol for 6, 12 and 18 hours at 110 °C, respectively. After the process, the samples were picked out from the solution, rinsed in ethanol and de-ionized water, followed by drying in air.

8.1.3 Surface characterization: The water contact angle measurement was done using de-ionized water with the aid of a goniometer (Rame Hart 250 model). The water contact angles were measured at 5 different points on the samples surfaces and the average values calculated. All the contact angle measurements were done at room temperature. The contact angle measurements were done on the polished, thermally oxidized and the chemically treated samples respectively.

The scanning electron microscope was used to study the surface morphology of the samples before and after thermal oxidation and also after the reaction with stearic acid and arachidic acid in the pressurized vessel. The S-4800 Hitachi scanning electron microscope, equipped with the energy dispersive X-ray analyzer, was used for surface morphology and chemical studies. The chemical nature of the surfaces was further characterized using the Fourier-Transform Infrared spectroscopy (FT-IR) and X-ray diffraction (XRD) analytical techniques. The energy dispersive X-ray analyses were done

on the thermally oxidized as well as the stearic and arachidic acid treated samples. The X-ray diffraction study was carried out using the X-2000 scintag X-ray diffractometer after thermal oxidation and the reaction of the thermally oxidized samples with the acids. The X-ray diffraction was done at a scan rate of 2.00 deg. / min. for 2θ values ranging between 10° and 60° for the analyses of the samples after thermal oxidation and between 2° and 60° for the samples after the reaction process with the acids. The average surface roughness, R_a , was measured for the polished, thermally oxidized and chemically treated samples using a 2-D surface profilometer (Phase II, SRG-450).

8.2 Results and discussion:

8.2.1 Surface morphology characterization using the Scanning electron microscope:

The scanning electron microscopic images after the thermo-chemical processes that involved thermal oxidation and reaction with stearic and arachidic acids revealed the evolution of various surface morphologies, depending on the stage of the process. The different morphologies obtained before and after the thermal oxidation; before and after the reactions with stearic and arachidic acids are shown in the figures below:

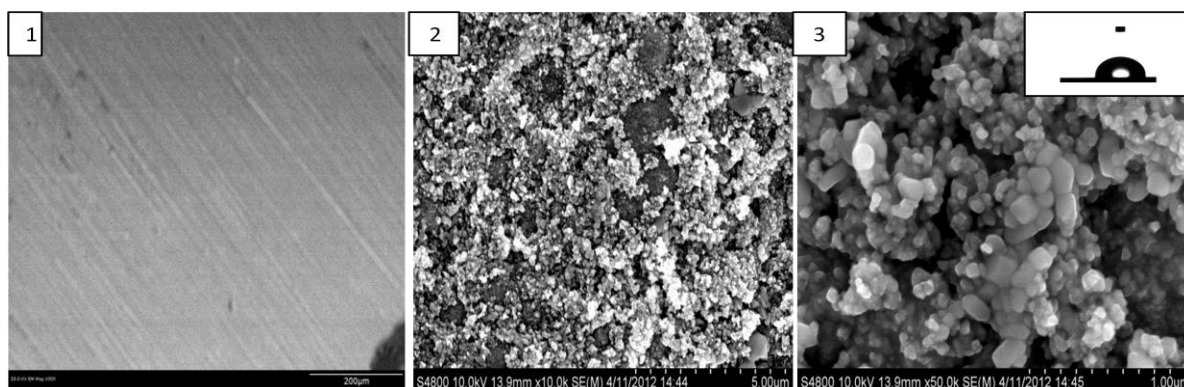


Figure 59: Polished and thermally oxidized surfaces C36000 copper alloy after thermal oxidation in air for 4 hours [insert is the contact angle of water on the surface].

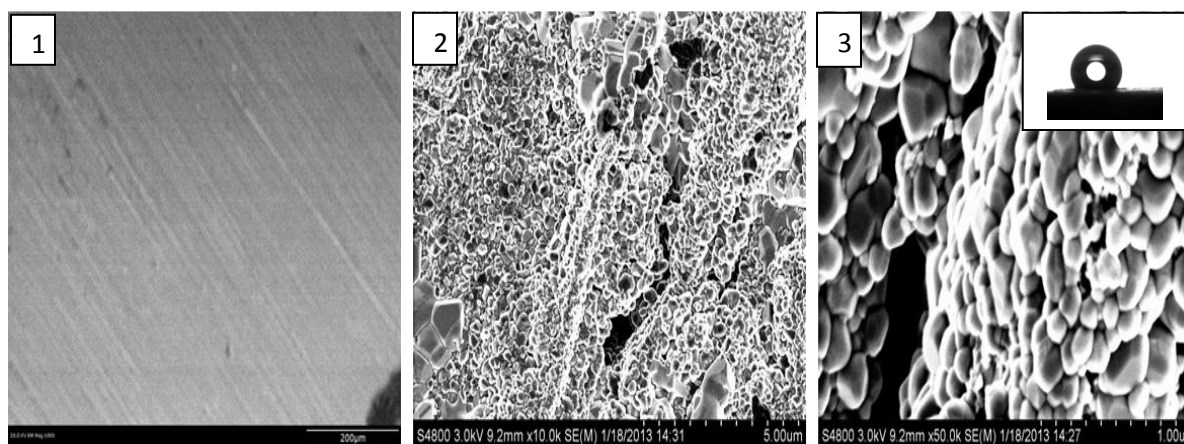


Figure 60: Polished and thermally oxidized surfaces C84400 copper alloy after thermal oxidation in air for 4 hours [insert is the contact angle of water on the surface].

From the scanning electron microscope images, tiny oxide granules were generated through thermal oxidation of C36000 and C84400 copper alloys, in figure 59 and figure 60. The average size of the oxide granules formed due to the thermal oxidation of C36000 copper was about 80 nm, ranging from 40 nm to about 100 nm. On the other hand, the average size of the oxides granules formed on the thermal oxidation of C84400 copper alloy for four hours was 170 nm.

The scanning electron images after the reaction of the oxide granule on the thermally oxidized C36000 and C84400 copper alloys with stearic acid solutions (0.005M STA)

show unique and different surface morphologies, in figure 61

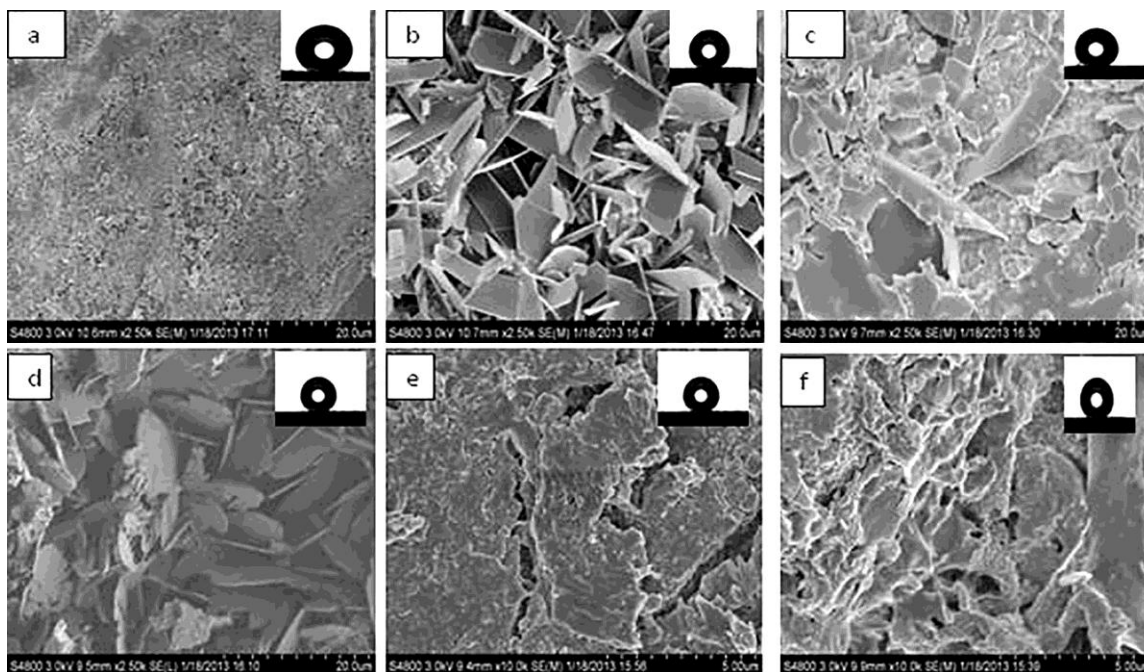


Figure 61: Scanning electron microscopic images of C36000 and C84400 after thermo-chemical modification in 0.005M STA; (a) C36000 after 6 hours thermo-chemical modification (b) C36000 after 12 hours thermo-chemical modification (d) C84400 after 6 hours thermo-chemical modification (e) C84400 after 12 hours thermo-chemical modification (f) C84400 after 18 hours of thermo-chemical modification.

As observed from the images above, after 12 hours of treatment of the C36000 copper alloy in 0.005M STA, flowery features grew on the surface, with an average dimension of 3.30 ± 1.20 microns. However, after further extension of the process to 18 hours, the fine flowery morphology of the surface became less apparent. The disappearance of these flowery features is not exactly understood but may be connected to the time used in the reaction process. Equally, flowery petals were observed after 6 hour of treatment of C84400 in 0.005M STA. However, the rough C84400 surfaces showed no unique features after 12 and 18 hours of reaction of the oxides with 0.005 M stearic acid.

The surface morphologies of the thermally oxidized C36000 and C84400 samples after the reaction with 0.005M ARA for different durations were equally examined using the scanning electron microscope in figure 62.

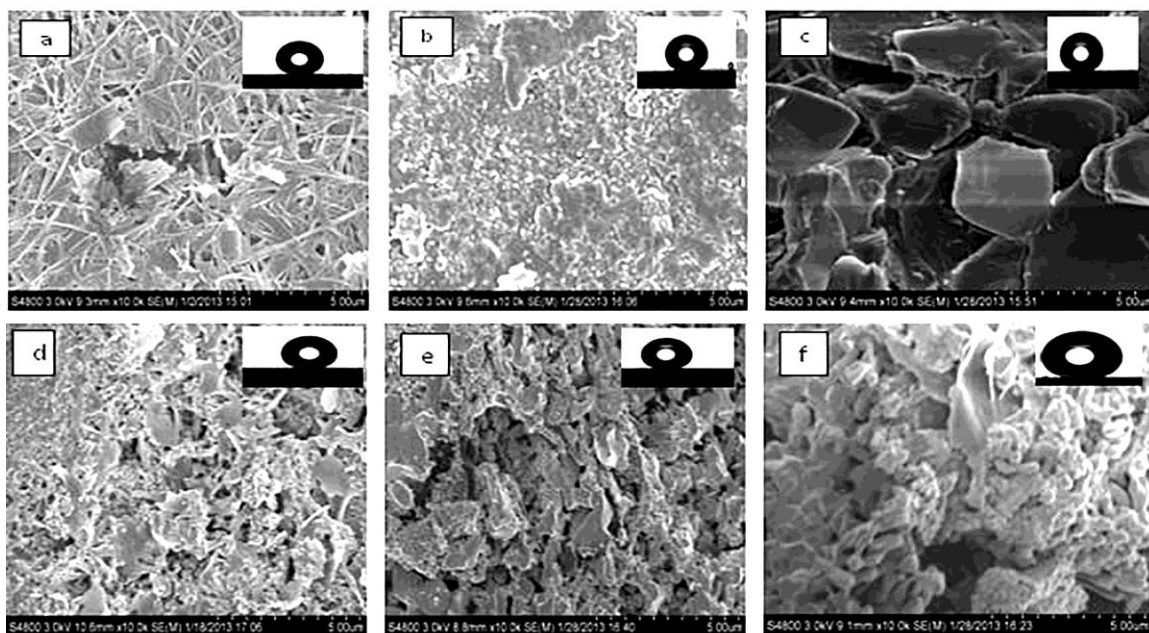


Figure 62: Scanning electron microscopic images of C36000 and C84400 after thermo-chemical modification in 0.005M ARA; (a) C36000 after 6 hours thermo-chemical modification (b) C36000 after 12 hours thermo-chemical modification (c) C36000 after 18 hours thermo-chemical modification (d) C84400 after 6 hours thermo-chemical modification (e) C84400 after 12 hours thermo-chemical modification (f) C84400 after 18 hours of thermo-chemical modification.

From the scanning electron microscope images, on reaction of the thermally oxidized C36000 copper alloy in 0.005M ARA for 6 hours, thin filament-like nanobelts grew on the surface of the sample with average size of 210 ± 60 nm. However, as the time of the reaction process extended, the morphological features coarsened into disc-like shapes as seen after 18 hours of the thermo-chemical treatment. Equally very rough, grainy surfaces were established on the C84400 copper alloys surfaces that were treated.

8.2.2 Chemical Composition of superhydrophobic surfaces formed by the thermo-chemical treatment of C36000 and C84400 copper alloys:

The chemical composition of the surfaces of the C36000 and C84400 copper alloy sample surfaces were evaluated using the following techniques:

- [i] Energy Dispersive X-ray analysis [EDX].
- [ii] Fourier Transform Infra-Red spectroscopy, [FT-IR].
- [iii] X-ray diffraction analysis, [XRD].

8.2.2 [i] Energy Dispersive X-ray analysis:

In this case, the energy dispersive X-ray analyses were carried out on thermally oxidized samples of the copper alloys that were reacted with the STA and ARA for 12 hours in figure 63, figure 64, and figure 65. The energy dispersive X-ray analyses show the immobilization of carbon, from the stearic and arachidic acids, on the surfaces of these samples. This resulted in a high carbon-oxygen elemental ratio as seen in the quantitative analyses of the elemental composition in Table 24 and Table 25.

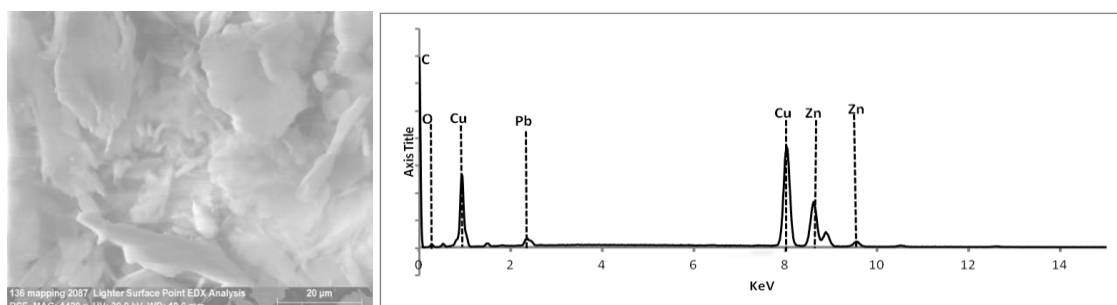


Figure 63: EDX elemental mapping and surface chemical composition of thermally oxidized C36000 copper alloy after reaction with 0.005M STA for 12 hours.

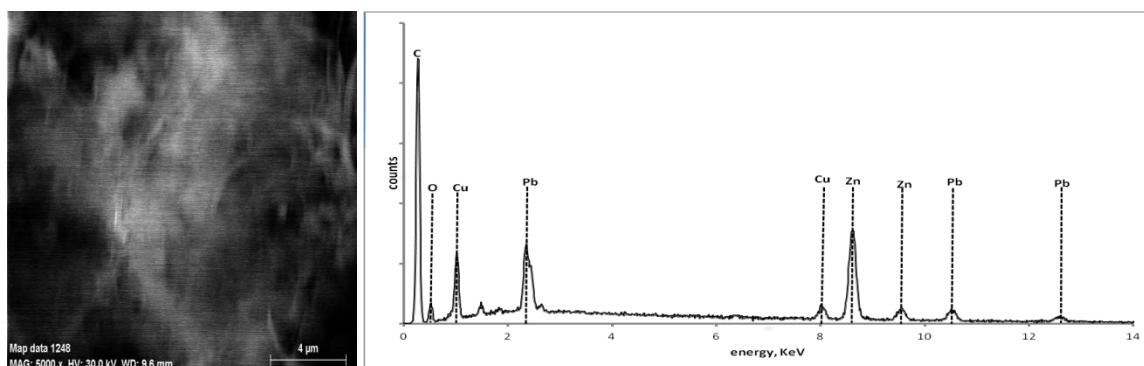


Figure 64: EDX elemental mapping and surface chemical composition of thermally oxidized C84400 copper alloy after reaction with 0.005M STA for 12 hours.

Table 24: Elemental composition of surfaces of thermally oxidized C36000 and C84400 copper alloys after reactions with 0.005M STA.

Thermally oxidized C36000 treated with STA			Thermally oxidized C84400 treated with STA		
Element	Wt. %	At. %	Element	Wt. %	At. %
Carbon	28.33	45.14	Carbon	11.84	19.59
Copper	13.70	1.27	Copper	0.48	0.15
Zinc	15.70	4.60	Zinc	9.83	2.99
Lead	1.76	0.53	Lead	16.96	1.63
Oxygen	40.51	48.47	Oxygen	60.89	75.65
Total	100.00	100.00	Total	100.00	100.00

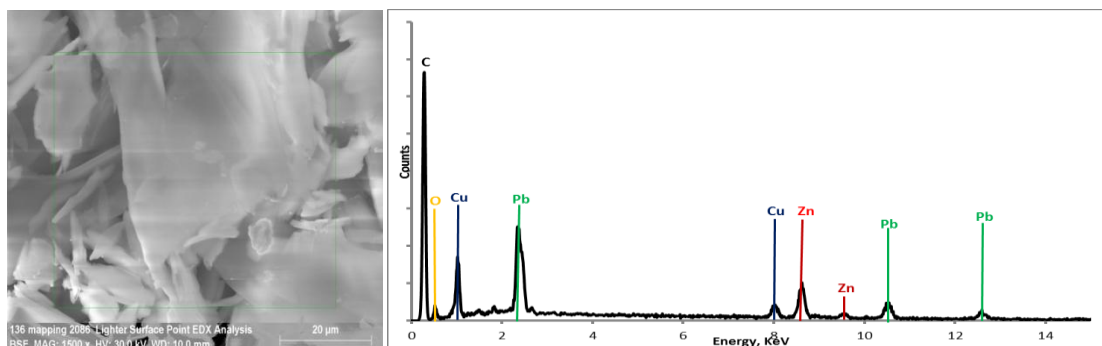


Figure 65: EDX elemental mapping and surface composition of thermally oxidized C84400 copper alloy after reaction with 0.005M ARA for 12 hours.

Table 25: Elemental composition of surfaces of thermally oxidized C36000 and C84400 copper alloys after reactions with 0.005M ARA.

Thermally oxidized C36000 treated with ARA			Thermally oxidize C84400 treated with ARA		
Element	Wt. %	At. %	Element	Wt. %	At. %
Carbon	21.74	58.92	Carbon	30.19	44.75
Copper	38.08	19.50	Copper	1.67	52.01
Zinc	21.27	21.27	Zinc	5.00	1.36
Lead	14.63	2.30	Lead	16.41	1.41
Oxygen	4.27	8.69	Oxygen	46.73	52.01
Total	100.00	100.00	Total	100.00	100.00

From the elemental analysis, it is noted that after 12 hours of the chemical reaction with STA, the surface in weight percentage of elemental composition is made mainly of carbon, due to the reaction of the oxides with the stearic and arachidic acids respectively. On the surfaces of the samples, elements of copper, zinc and lead were equally detected. The presence of these elements may be due to the un-reacted oxides present on the surfaces or elemental composition of the alloy samples. However, the energy dispersive X-ray analyses have shown that there were reactions between the acids with the oxide nano-particles on the surfaces thereby effectively altering the surfaces' chemical composition. These were effectively understood through the X-ray diffraction studies of which will be discussed later.

8.2.2 [ii] Infra-red spectroscopic analysis of surface of samples:

The infra-red spectroscopic analysis, in figures 66 and 67, of the surfaces of the samples of the thermally oxidized C36000 and C84400 copper alloys after 12 hours of the reaction process with STA and ARA, showed a number of bands due to the formation of stearates/ arachidates surface layers on interaction of the carboxylate group with thermally oxidized metallic surfaces.

8.2.2 [ii] a. FT-IR spectroscopic analysis of thermo-chemically treated (12hrs) C36000 sample in 0.005M STA:

Characteristic bands for the stearate formed were observed at 1536 cm^{-1} and 1398 cm^{-1} . These bands are due to the anti-symmetric and symmetric carboxylate stretching bands [$\nu_a\text{ COO}^-$ and $\nu_s\text{ COO}^-$], respectively⁸⁹. Anti-symmetric and symmetric methylene stretching and methylene scissoring bands [$\nu_a\text{ CH}_2$, $\nu_s\text{ CH}_2$ and $\delta_s\text{ CH}_2$] were observed at about 2915 , 2848 and 1460 cm^{-1} , respectively. These bands are due to the alkyl chain of

the stearate formed. The infra red bands at 1105 cm^{-1} , 720 cm^{-1} and 676 cm^{-1} are respectively assigned to the stretching frequency of the carbon-carbon bond (C-C) in the stearate chain and the bending frequency of the methylene group [$\delta_s\text{ CH}_2$] respectively⁹⁰.

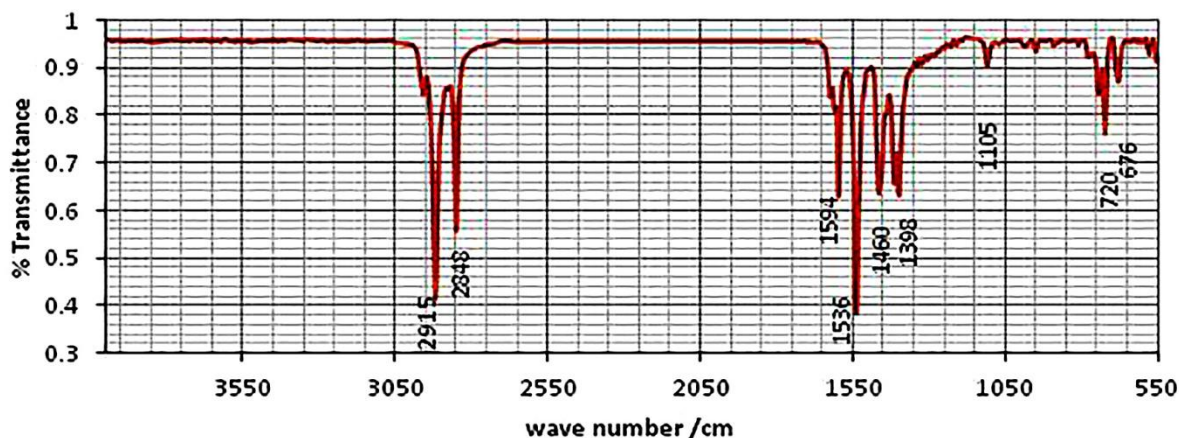


Figure 66: FT-IR spectrum of thermally oxidized C36000 after reaction with 0.005M STA for 12 hours.

The shift in infra-red transmittance after the reaction process with stearic acid shows that there is the presence of the stearate reaction product on the surface of the C36000 sample that was treated.

8.2.2 (ii) b. FT-IR spectroscopic analysis of thermo-chemically treated (12hrs) C84400 sample in 0.005M STA:

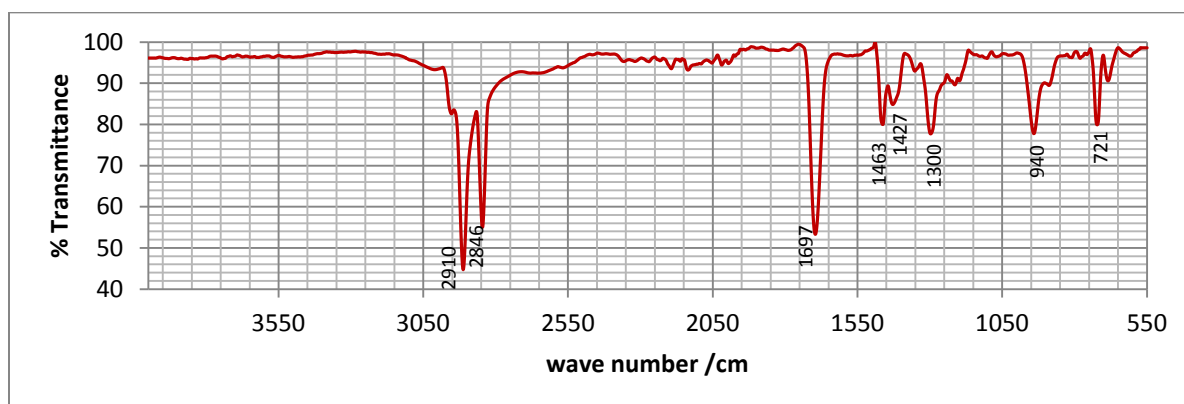


Figure 67: FT-IR spectrum of thermally oxidized C84400 after reaction with 0.005M STA for 12 hours.

The absorption bands observed included the anti-symmetric and symmetric methylene stretching at 2910 cm^{-1} and 2846 cm^{-1} . The medium assumption bands at 1463 cm^{-1} is equally assigned to the methylene group. These bands are formed from the stearates on the surface of the sample. The bands due to the carboxylate stretching were observed 1427 cm^{-1} . The C-C bonds stretch at the absorption bands observed at 1300 cm^{-1} , 940 cm^{-1} , 721 cm^{-1} respectively.

8.2.2 (ii) c. FT-IR spectroscopic analysis of thermo-chemically treated (12hrs) C36000 sample in 0.005M ARA:

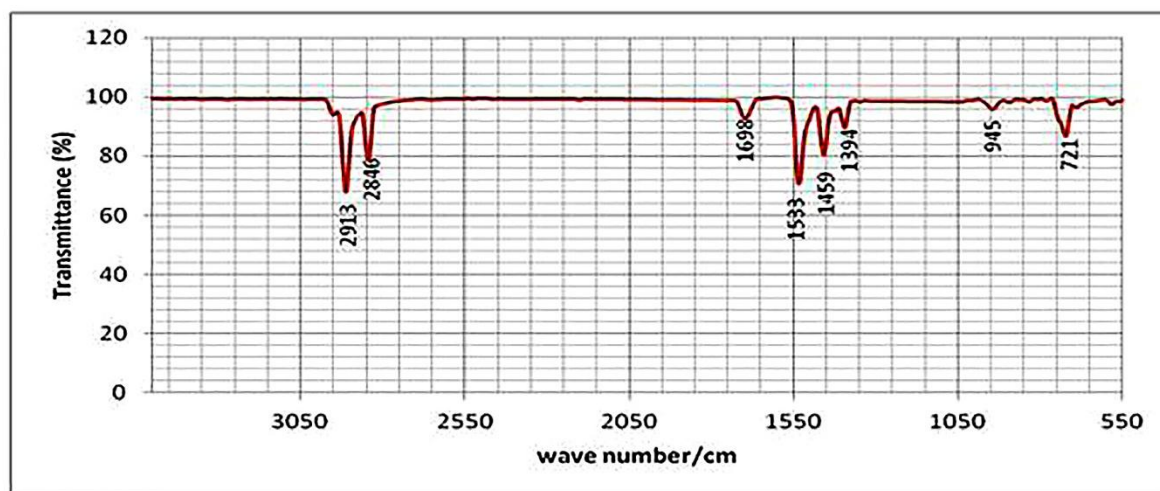


Figure 68: FT-IR spectrum of thermally oxidized C36000 after reaction with 0.005M ARA for 12 hours

In the FT-IR spectra of the C36000 sample after 12 hours of treatment in 0.005M ARA, and presented in figure 67, showed the anti-symmetric and symmetric methylene stretching frequencies at 2913 cm^{-1} and 2846 cm^{-1} . The methylene scissoring band was observed at 1459 cm^{-1} . The characteristic bands of the arachidates were observed at 1395 cm^{-1} and 1533 cm^{-1} respectively.

8.2.2 (ii) d. FT-IR spectroscopic analysis of thermo-chemically treated (12hrs) C84400 sample in 0.005M ARA:

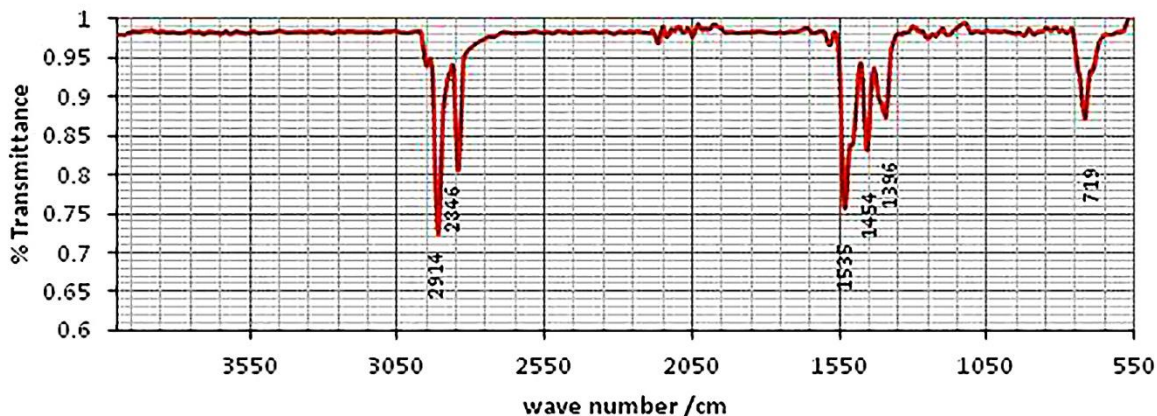


Figure 69: FT-IR spectrum of thermally oxidized C84400 after reaction with 0.005M ARA for 12 hours

In figure 69, the anti-symmetric and symmetric methylene stretching frequencies are observed at 2914 cm^{-1} and 2846 cm^{-1} in the spectra. The asymmetric and the symmetric stretching band for the COO^- at 1396 cm^{-1} and 1535 cm^{-1} equally proved the formation of arachidates with the oxides that was on the surface of the C84400 substrate.

The FT-IR spectra of the thermally oxidized C36000 and C84400 samples that were treated in the fusion reaction process with stearic as well as arachidic acids show a lack of an O-H absorption band in some cases, for both stretching and bending frequencies that are found in the both the stearic and arachidic acids as well as other carboxylic acids.

The COO^- stretches which produce two strong, unique infrared absorbance bands are also observed in all spectra presented. The asymmetric COO^- stretch generally falls between 1650 and 1540 cm^{-1} and the symmetric COO^- stretch is found between 1450 - 1398 cm^{-1} [91]. Thus the presence of these bands is confirmatory of the formation of metal stearates and arachidates with the oxides on the surfaces of the C36000 and C84400 samples.

8.2.2 (iii) a X-ray diffraction studies of the thermally oxidized and stearic acid treated C36000 samples:

To further determine the nature of the chemical composition of the oxides formed on the samples that were thermally oxidized, the X-ray diffraction analysis stated in figure 70 of the surface was studied.

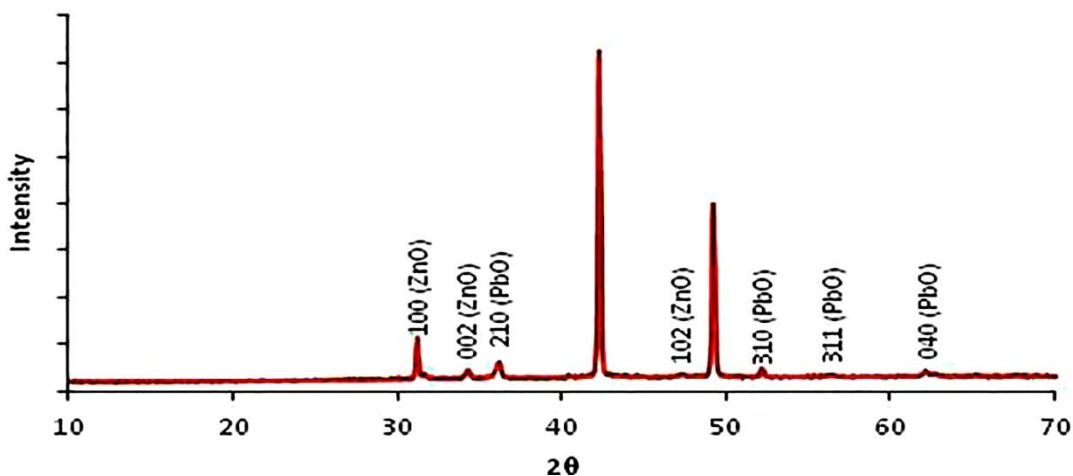


Figure 70: X-ray diffraction pattern of thermally oxidized C36000 brass sample.

The major diffraction peaks observed corresponded to the (100), (002) and (112) planes of ZnO as well as the (210), (310), (311) and (040) planes of PbO. The diffraction peaks for these oxides were in agreement with the PDF file number 36-1451 and PDF file number 38-1477 for ZnO and PbO respectively.

The formations of these oxides are based on their Standard Gibbs free energy, ΔG° as expressed in the equations 19 and 20 respectively for ZnO and PbO formation. At the temperature of 650 °C used for the thermal oxidation process, the standard Gibbs free energy of formation of ZnO is the most negative therefore explaining why the surface of the C36000 substrate is mostly ZnO on thermal oxidation in air.

At the thermal oxidation temperature of 650 °C, the standard Gibbs' free energy of formation of ZnO is -570 563 J which is more negative than the standard Gibbs' free energy of formation of Cu₂O and PbO. This implies that the formation of ZnO is very feasible at the 650 °C used for the thermal oxidation process. However, if the concentration of Zn in a typical brass alloy is below a critical concentration, internal oxidation is expected and both the Cu and Zn alloying elements will be oxidized. If on the other hand, the concentration of Zn is above the critical concentration value, external oxidation of Zn to form ZnO is expected.

The theoretical value of the critical concentration of Zn in these Cu-Zn alloys above which only external oxidation of Zn to ZnO has been estimated at about 15 at.- % of Zn. Based on the alloying composition of the C36000 brass, the formation of ZnO, without CuO formation, is expected as confirmed from the X-ray diffraction analyses. Furthermore, lead has a low melting point compared to the other alloying elements in the C36000 brass. Therefore, at the temperature of the thermal oxidation process, it easily melts and segregates to the sample surfaces and is oxidized to PbO as indicated in the X-ray diffraction analyses.

X-ray diffraction studies were equally carried out on the samples after the reaction of the thermally oxidized surfaces with the 0.005M stearic acid solutions. The X-ray diffraction studies were done at 2θ angles between 2.5 ° and 60 °. The X-ray diffraction pattern of the surfaces of the thermally oxidized samples after the reaction with the 0.005M STA at the elevated temperature for 12 hours, in figure 71, showed the presence of weak diffraction peaks belonging to PbO on the surface. It is believed therefore, that not all the

oxides on the rough surface layer of the samples reacted to form the superhydrophobic surface morphology observed.

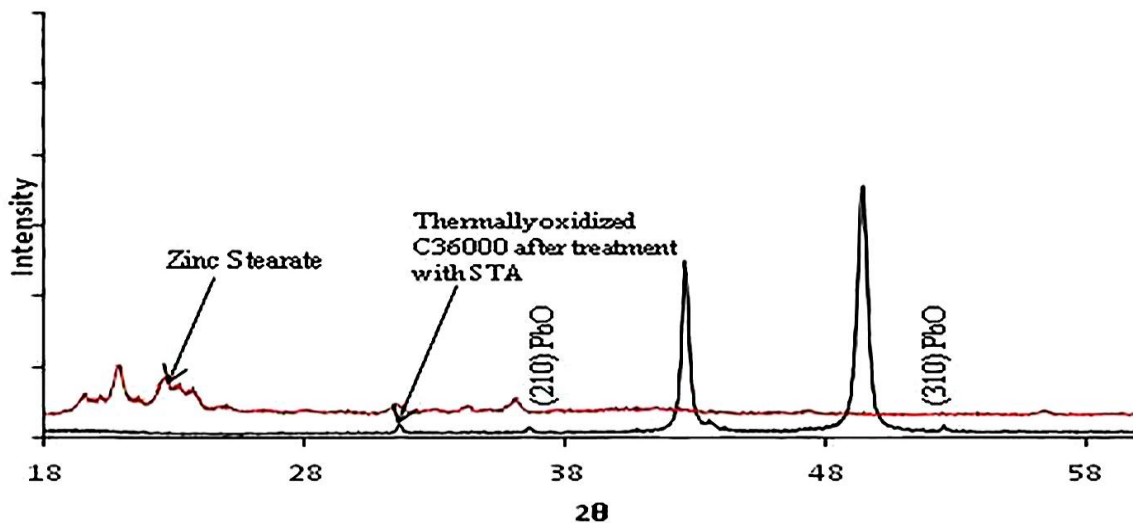


Figure 71: X-ray diffraction pattern of zinc stearate powder and superhydrophobic C36000 Brass sample surface after its reaction with stearic acid at 2θ angles from 18° to 60° .

To this end, the diffraction peaks observed between 2.5° and 18° belongs to the metal stearate formed as a result of the reaction of the oxides with the stearic acid. To confirm the nature of the stearate formed, the comparative analysis of the X-ray diffraction pattern of pure zinc stearate showed corresponding diffraction peaks between 2° and 18° with those obtained for the surface of the sample after the reaction with stearic acid with diffraction peaks at 2θ values of 3.9° , 4.4° , 4.6° , 5.8° , 6.4° , 7.6° , 9.8° , 10.6° .

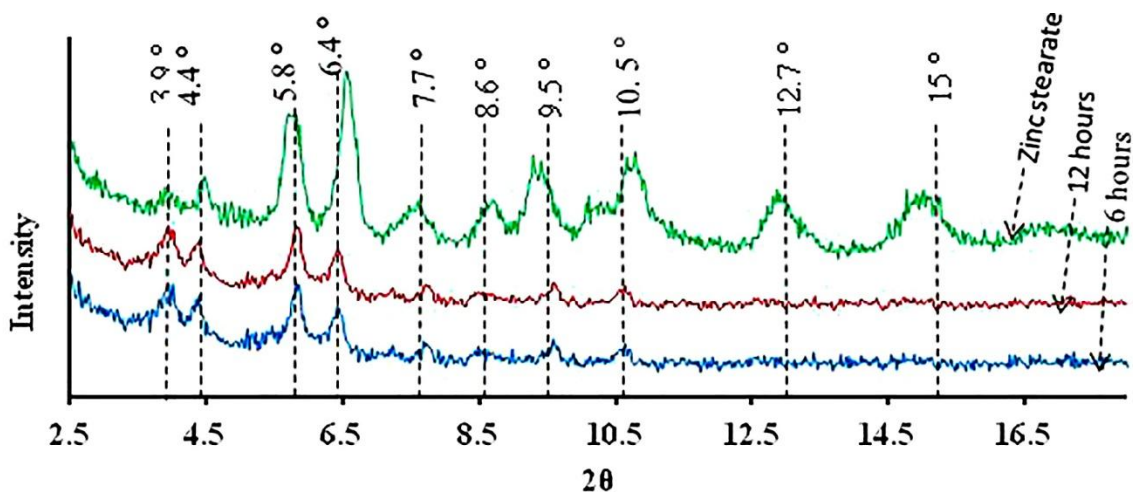


Figure 72: X-ray diffraction pattern of superhydrophobic C36000 Brass sample surface after reaction with stearic acid and zinc stearate at 2θ angles from 2.5° to 18° .

8.2.2 (iii) b. X-ray diffraction analysis of thermally oxidized C84400 treated with 0.005M STA in a chemical reaction process:

The characterization of the C84400 samples treated for 12 hours in 0.005M STA, after an initial 4 hours of thermal oxidation in air was carried out using X-ray diffraction technique both low and high 2θ angles. For low angle X-ray diffraction between, 2° and 18° , diffraction peaks were observed at 4.1° , 5.8° , 7.6° , 9.6° , and 11° with the strongest peak occurring at 5.8° in figure 73.

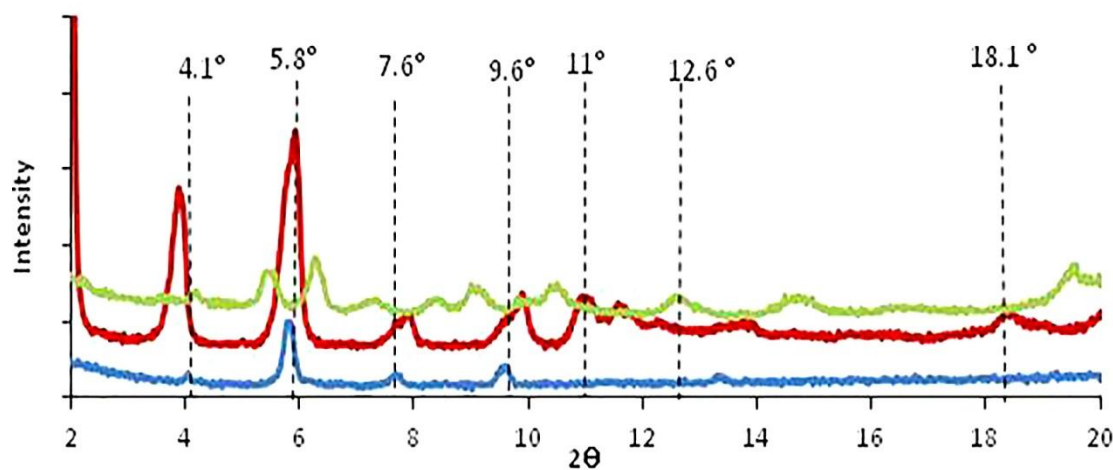


Figure 73: X-ray diffraction pattern of superhydrophobic C84400 brass sample surface after reaction with stearic acid at 2θ angles from 2° to 18° .

The earlier work on zinc and copper metal soaps found that the diffraction patterns of these soaps are very similar in the region below 20° for 2Θ , with their 5 orders of long spacing at similar d-spacing values ^[91]. Due to the presence of CuO and ZnO on the surface of the thermally oxidized sample, the weak diffraction peaks observed are due to a mixture of both copper and zinc stearates for the diffraction peaks observed at 2Θ values of 4.1° , 5.8° , 7.8° , 9.6° and 13.3° . The X-ray diffraction pattern for commercially obtained copper and zinc stearate powders were found to be some correspondence to those that were observed on the surface layer of the treated samples of C84400 copper alloy as shown in figure 73.

The diffraction patterns of the initially oxidized samples and the treated samples were compared in figure 74. The treated sample showed the presence of grains of oxides on the surface, showing that not all of the oxides on the surface reacted with the STA, after 12 hours of the reaction.

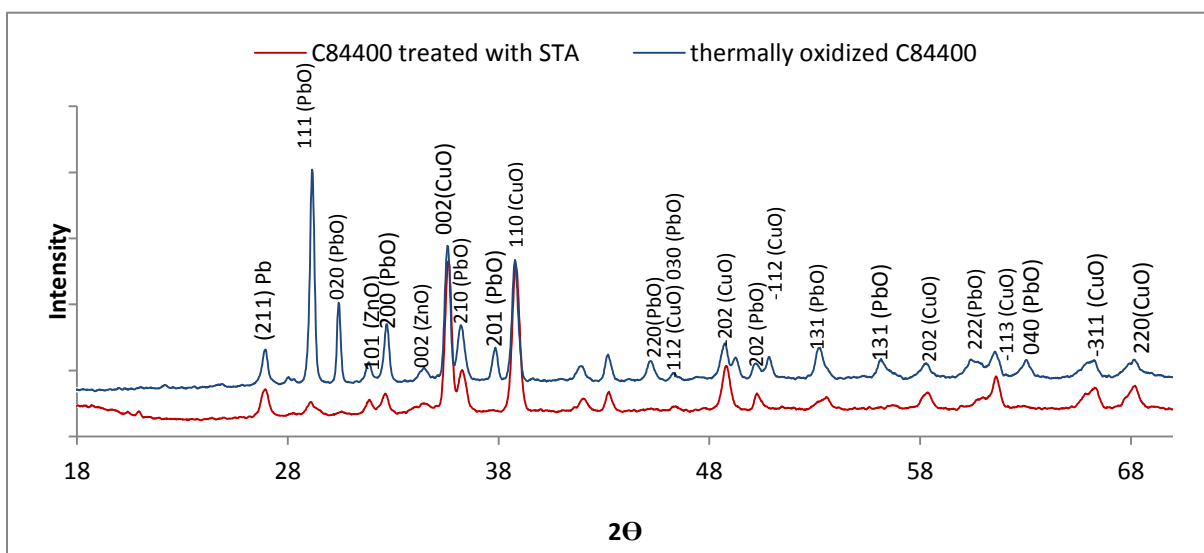


Figure 74: X-ray diffraction pattern of superhydrophobic C84400 Brass sample surface after reaction with stearic acid at 2Θ angles from 18° to 70° .

However, there is attenuation of the intensity of the diffraction peaks and some diffraction peaks of some planes of the oxides of ZnO, PbO and CuO were no longer present after the reaction process. This implied that limited reaction occurred between the oxide grains with the stearic acid. The oxide planes that were no more observed after the reaction with the 0.005M stearic acid included the (002) plane of ZnO; (020), (220), (030) and (131) planes of PbO; (-112), (112) planes of CuO. The attenuation of the oxide peaks can be ascribed partly to the reaction of these planes with the conjugate base anion of the stearic acid as well as the resultant coverage of the sample surfaces by the reaction product of the process.

8.2.2 (iii) c. X-ray diffraction analysis of thermally oxidized C36000 treated with 0.005M ARA in a fusion reaction:

Diffraction peaks were observed in the low 2θ angle range of 2° to 20° . The diffraction angles of the peaks were observed at 2θ corresponding to 3.4° , 5.4° , 5.8° , 6.6° , 8.2° , 9.6° , 11.4° , and 19.7° , in figure 75.

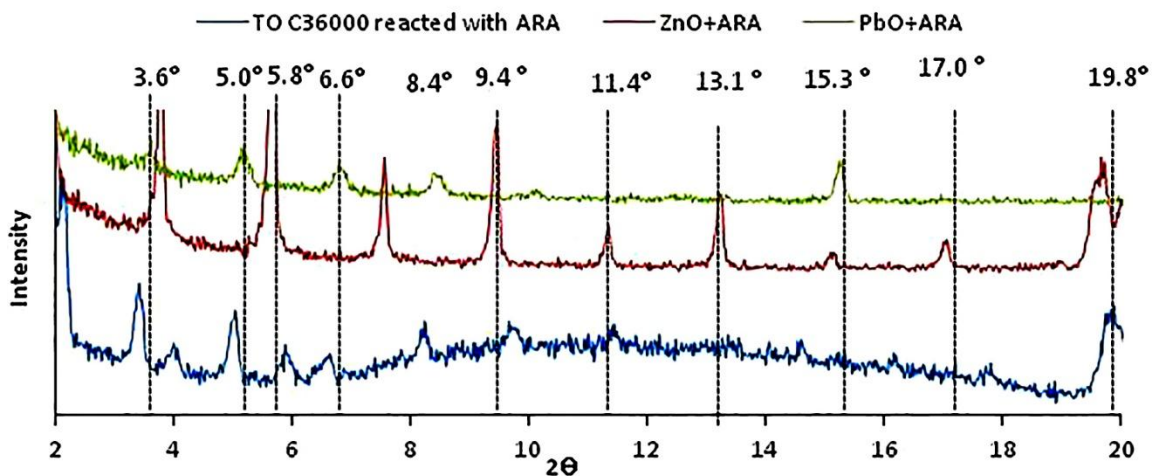


Figure 75: X-ray diffraction pattern of superhydrophobic C36000 brass sample surface after reaction with arachidic acid at 2θ angles from 2° to 18° .

These diffraction pattern observed within this ranged were compared to the diffraction pattern of zinc and lead arachidate, prepared as explained in Appendix A. Also at higher angle of diffraction, peaks hitherto not present in the diffraction pattern of the thermally oxidized C36000 copper alloy were observed. A cluster of peaks were observed between 20° and 30° , 2θ in figure 76.

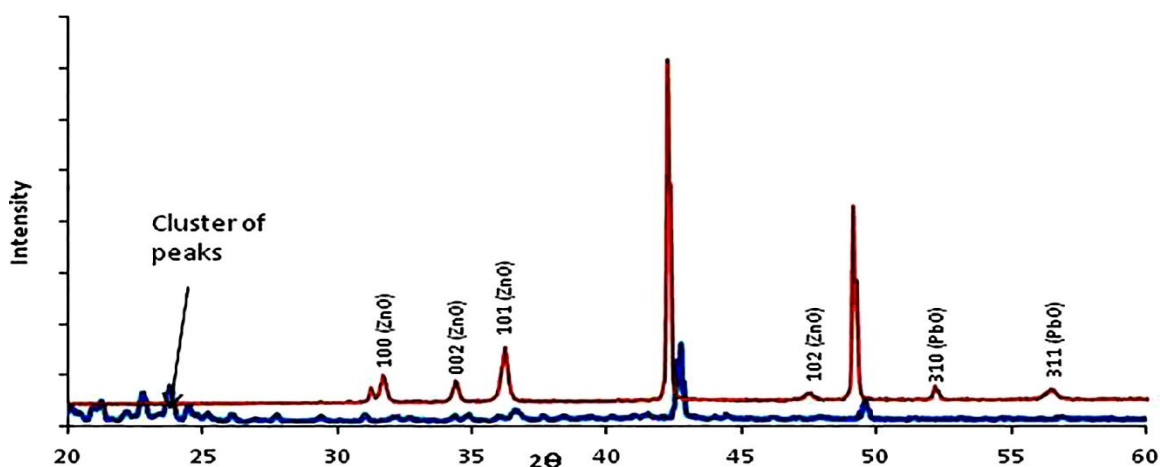


Figure 76: X-ray diffraction pattern of superhydrophobic C36000 brass sample surface after reaction with arachidic acid at 2θ angles from 18° to 60° .

8.2.2 (iii) d. X-ray diffraction analysis of thermally oxidized C84400 copper alloy treated with 0.005M ARA in a thermo-chemical process:

Prior to the chemical reaction process between the oxidized sample surfaces with 0.005 M ARA, the X-ray diffraction pattern of the surface showed the presence of CuO, PbO and ZnO, in figure 70. However, at small angles of 2θ , diffraction peaks were observed after the thermo-chemical reaction.

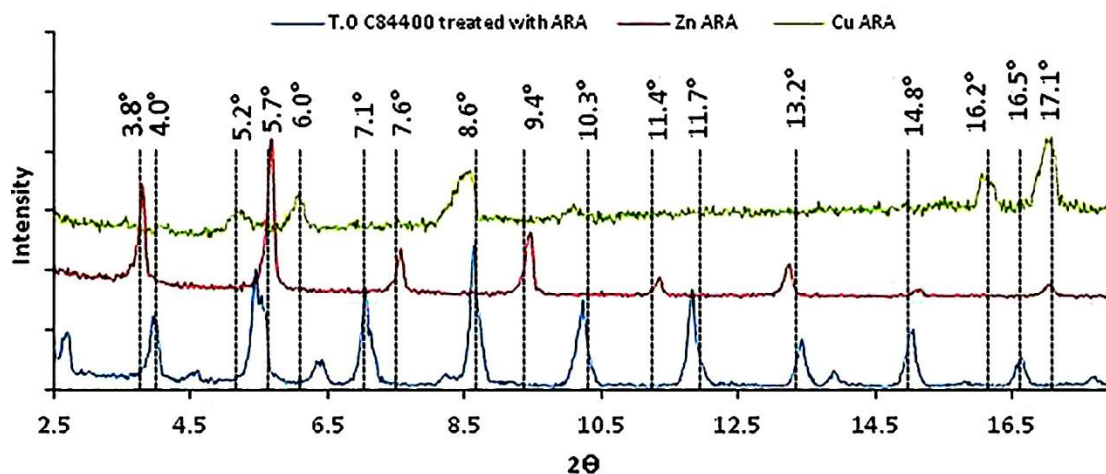


Figure 77: X-ray diffraction pattern of superhydrophobic C84400 Brass sample surface after reaction with arachidic acid at 2θ angles from 2.5° to 20° .

To confirm the type and nature of the arachidates formed, CuO, PbO and ZnO were separately treated through a similar process with 0.005M ARA, as described elsewhere in Appendix A and the X-ray diffraction patterns within the same 2θ range compared in figure 77. In this case, the diffraction peaks at 3.9° , 5.4° , 13.3° and 15.0° corresponded well with those of zinc arachidate observed at 3.8° , 5.6° , 13.2° and 15° .

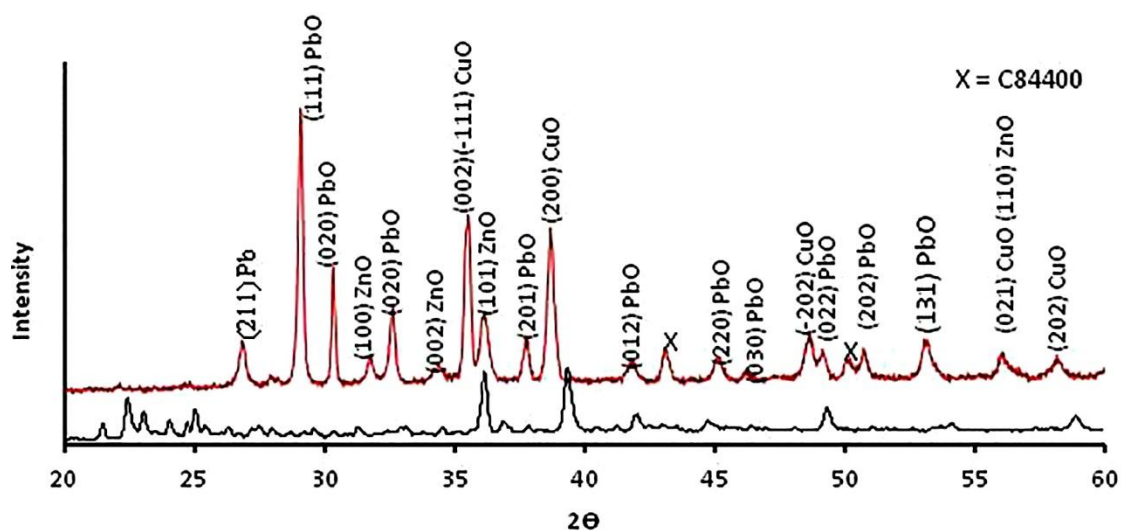


Figure 78: X-ray diffraction pattern of superhydrophobic C84400 brass sample surface after reaction with arachidic acid at 2θ angles from 20° to 60° .

8.3 Contact angle of water and surface roughness evaluation:

The evaluated contact angles of water and the average surface roughness, R_a recorded on the C36000 and C84400 Copper alloys that were used in the thermo-chemical treatment process are stated in the tables below:

Table 26: Table of the average surface roughness, R_a and contact angle of water on polished, thermally oxidized and chemically reacted with 0.005M STA and 0.005 ARA C36000 and C84400 copper alloys.

Sample	0.005M STA				0.005M ARA			
	C36000		C84400		C36000		C84400	
	Θ	R_a	Θ	R_a	Θ	R_a	Θ	R_a
Polished sample	58.1 ± 2.1	0.1	$54.7 \pm$	0.1	58.1 ± 2.1	0.1	54.7 ± 1.2	0.1
4hrs heat treatment	$72.9 \pm$	2.5 ± 0.2	70.3 ± 3.4	0.7 ± 0.1	$72.9 \pm$	2.45 ± 0.2	70.3 ± 0.1	0.7 ± 0.1
6	150.9 ± 4	1.4 ± 0.3	150.3 ± 2.5	1.7 ± 0.2	151.1 ± 2.0	0.8 ± 0.2	153.5 ± 2.3	0.5 ± 0.3
12	150.2 ± 1.5	1.2 ± 0.1	153.8 ± 3.5	1.4 ± 0.1	150.5 ± 1.5	0.4 ± 0.1	152.9 ± 2.1	0.6 ± 0.2
18	133.3 ± 4.1	0.3 ± 0.1	137.9 ± 9.1	1.0 ± 0.3	144.1 ± 3.7	4.3 ± 0.3	130.6 ± 2.8	0.5 ± 0.1

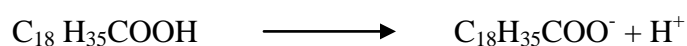
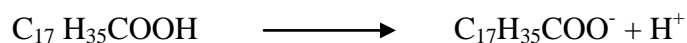
From the experiments, the polished as well as the thermally oxidized samples of both the C36000 and C84400 copper alloys were essentially hydrophilic surfaces, showing contact angles of water below 90° . Though some workers have reported hydrophobicity of metal surfaces with oxides⁹², the thermally oxidized samples in this case were hydrophilic.

Therefore, the superhydrophobicity is achieved by the reaction of the oxide with the STA and ARA; where the hydrophobic terminal groups from these organic acids are chemically bonded to the surfaces through the $-\text{COO}^-$ group. During the reaction, the degrees of reactivity of these oxides present on the thermally oxidized surfaces with the stearic and arachidic acids used in the process depends on the bond strengths of the metal-oxygen bonds of the oxides. To this end, the bond strength of Zn-O, Pb-O and Cu-O, which have been previously identified on the surfaces of the thermally oxidized

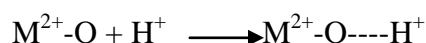
samples through X-ray diffraction, are 284.1kJ mol^{-1} , 378kJ mol^{-1} and 343kJ mol^{-1} , respectively.

The stearic and arachidic acid solution reacts with the oxides, preferentially through a mechanism of dissolution which proceeds via two steps:

(i) The acid ionization step:



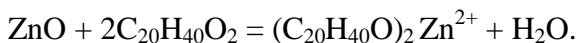
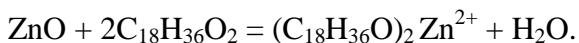
(ii) Protonation of the metal oxide:



The above pathway plays an important role in the oxide dissolution and reaction with the stearic and arachidic acids. The metal-oxygen bond is loosened, depending on the bond strength, through the protonation process. To this end, the Zn-O bonds breaks faster and the Zn^{2+} ions reacts preferentially with the stearate and arachidate ions to form the zinc stearate and zinc arachidate respectively on the surfaces of the thermally oxidized C36000 copper alloys. However, traces of lead arachidate were noted in the X- ray diffraction of the thermally oxidized C36000 brass that was reacted in the 0.005 M ARA solution for 12 hours.

Thus, in the 0.005M STA and 0.005 M ARA at the temperature used for the process, the reaction of the ZnO present on the surfaces of the thermally oxidized C36000 copper alloy is highly feasible and more favored because of the lower bond strength of Zn-O bonds compared to the other Pb-O bonds of the PbO found on the surfaces. In this acidic

media at the elevated reaction temperature, the ZnO bonds breaks easily, showing more labiality and reacts with the organic acids on the basis of the equations below:



However, in the C84400 thermally oxidized samples, a mixed stearate and arachidate products of Zn, Cu and Pb are formed. This is due to the percentage composition of the alloying elements which resulted in considerable amount of CuO, ZnO and PbO forming on the sample surfaces on thermal oxidation. Therefore, the reaction was not only influenced by the bond strengths but also by the relative availability of the other oxides beyond ZnO.

Wettability involves interaction between the water drops and the solid surfaces. For the polished and the thermally oxidized surfaces, the water contact angle shows the Wenzel State with the water drop totally wetting the surface and penetrating the rough cavities of the thermally oxidized surfaces.

However, after the treatment in both the 0.005M STA and 0.005M ARA, the modified surfaces showed superhydrophobicity with the water contact angles well above 150° for samples of the copper alloys treated for 6 and 12 hours respectively. This is essentially due to some reasons namely; the increase in the trapped air fraction leading to the suspension of water droplet on top of the rough hierarchical surface and a sharp reduction in surface energy due to the immobilization of the long carbon chains from the organic acids on the surface. Though there is a reduction of the average roughness value after the

reaction of the oxidized surfaces with STA and ARA in figure 79 (a and b)], the nature of the rough surface generated can sustain a Cassie-Baxter wetting state.

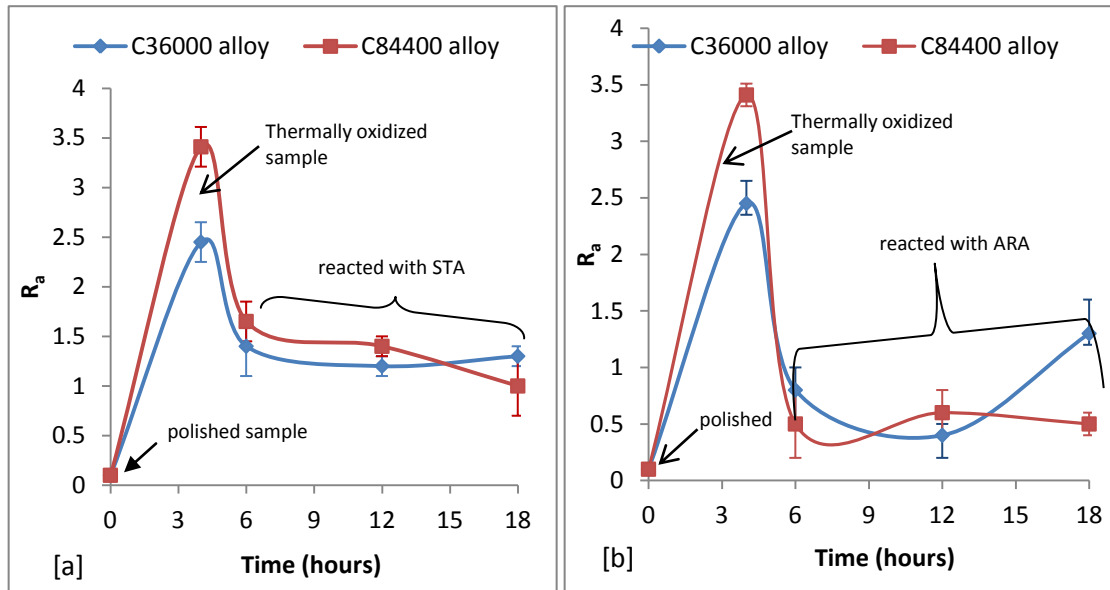


Figure 79: Plot average surface roughness of polished, thermally oxidized and reacted with (a) 0.005M STA and (b) 0.005M ARA with time.

The relationship between the surface wettability and the roughness of the surface morphological features can therefore be described by the Cassie-Baxter equation (5). Using this relationship, the fractional area of the solid surfaces of the treated samples f_{sw} were evaluated as follows:

Table 27: Size distribution and calculated fractional surface area for wetting of surface with water drops.

Time (hrs)	0.005M STA				0.005M ARA			
	C36000		C84400		C36000		C84400	
	Size	f_{sw}	Size	f_{sw}	Size	f_{sw}	Size	f_{sw}
6	----	0.082	3.29	0.083	0.25	0.082	0.82	0.065
12	2.28	0.086	-----	0.065	-----	0.085	-----	0.069
18	3.18	0.21	-----	0.165	2.77	0.124	0.56	0.22

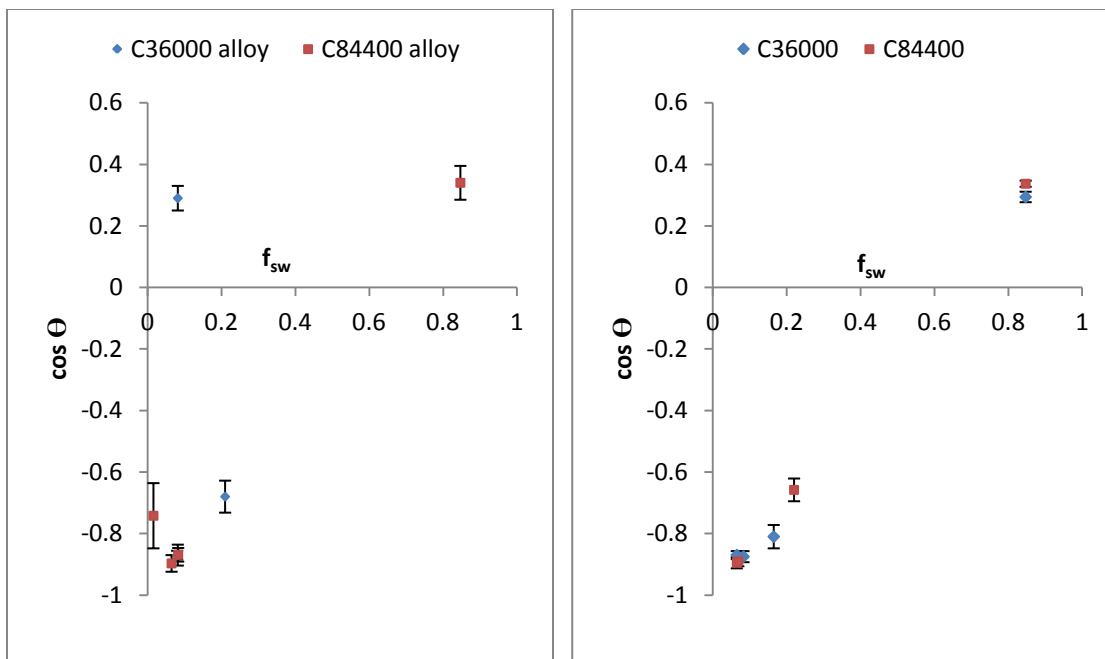


Figure 80: Plot of $\cos \Theta$ against the fractional surface area (f_{sw}) available for contact with water drop.

A plot of the fractional area of the surface available for wetting were very small for the surfaces that exhibited superhydrophobicity, as shown in figure 80. Therefore, the primary driver of the superhydrophobicity beyond the chemical composition is the hierarchical surface structure, as seen in the SEM pictures, which provides roughened surfaces where air can be trapped within the spaces of the micro/nanostructure.

CHAPTER NINE

SUPERHYDROPHOBICITY OF C36000 AND C84400 GENERATED BY THE THERMO-CHEMICAL TREATMENT WITH STEARIC AND ARACHIDIC ACID

9.0 Introduction: A direct chemical oxidation treatment of C36000 and C84400 copper alloys was used to achieve superhydrophobicity of the surfaces. Stearic and arachidic acids are used directly as oxidizing agents to grow nanostructures on the surfaces of the C36000 and C84400 copper alloy samples in order to achieve superhydrophobicity on these sample surfaces. The process involved a slow oxidative approach at very low concentrations of the oxidizing acidic ethanolic solutions at various oxidizing temperatures and on surfaces with different average roughness achieved through mechanical abrasion.

9.1 Experimental:

9.1.1 Materials: The C36000 and C84400 copper alloys were used in these experiments and were obtained from Baker Manufacturing, LLC (Evansville, WI) and have their chemical compositions given in Table 1, and 2. Other reagents used include ethanol solution, stearic acid and arachidic acid, all obtained from Sigma-Aldrich chemicals; of 99.9% grade purity. All the reagents were used without further purification.

9.1.2 Method: The direct oxidation processes were carried out by direct immersion in different concentrations of the STA [0.005M, 0.010M, 0.015M] for the time durations of one to five days, at room temperature and in 0.005M ARA solutions at 30 °C and 40 °C for the time duration of one to five days. The process of direct chemical oxidation of these copper alloy samples was done in a parr pressure reaction apparatus (model no.

4601Q). Also, copper alloy surfaces of the samples with various average roughness values of the surfaces, achieved through mechanical abrasion of the surfaces with 50 grit size SiC paper of various grades were equally chemically oxidized at room temperature in 0.015M STA, in a combination of mechanical abrasion and chemical oxidation.

9.2 Characterization:

The characterization of the sample surfaces involved the use of scanning electron microscope (S-4000 Hitachi model), the X-ray diffraction technique (with the Scintag 2000 XRD machine), 2-D surface profilometer and the atomic force microscope, for the surface roughness characterization as well as the goniometer for water contact angle and hysteresis measurement.

9.3 Results and discussion:

9.3.1 Characterization of surface morphology of the C36000 and C84400 copper alloys directly oxidized in STA at room temperature and in ARA at 30 °C and 40 °C.

To appraise the changes in the surface morphologies, samples of the copper alloys treated in 0.005M STA at room temperature was studied. The scanning electron microscope was used to study the surface morphologies of the samples after the chemical oxidation processes under the above stated conditions. The S-4800 Hitachi scanning electron microscope was used for the surface morphology studies.

9.3.1 [a] Surface morphologies of samples treated in 0.005M STA at room temperature:

The observed surface morphologies on the C36000 and C84400 surfaces after their direct chemical oxidation on 0.005M STA at room temperature is shown in figures 81 and 82.

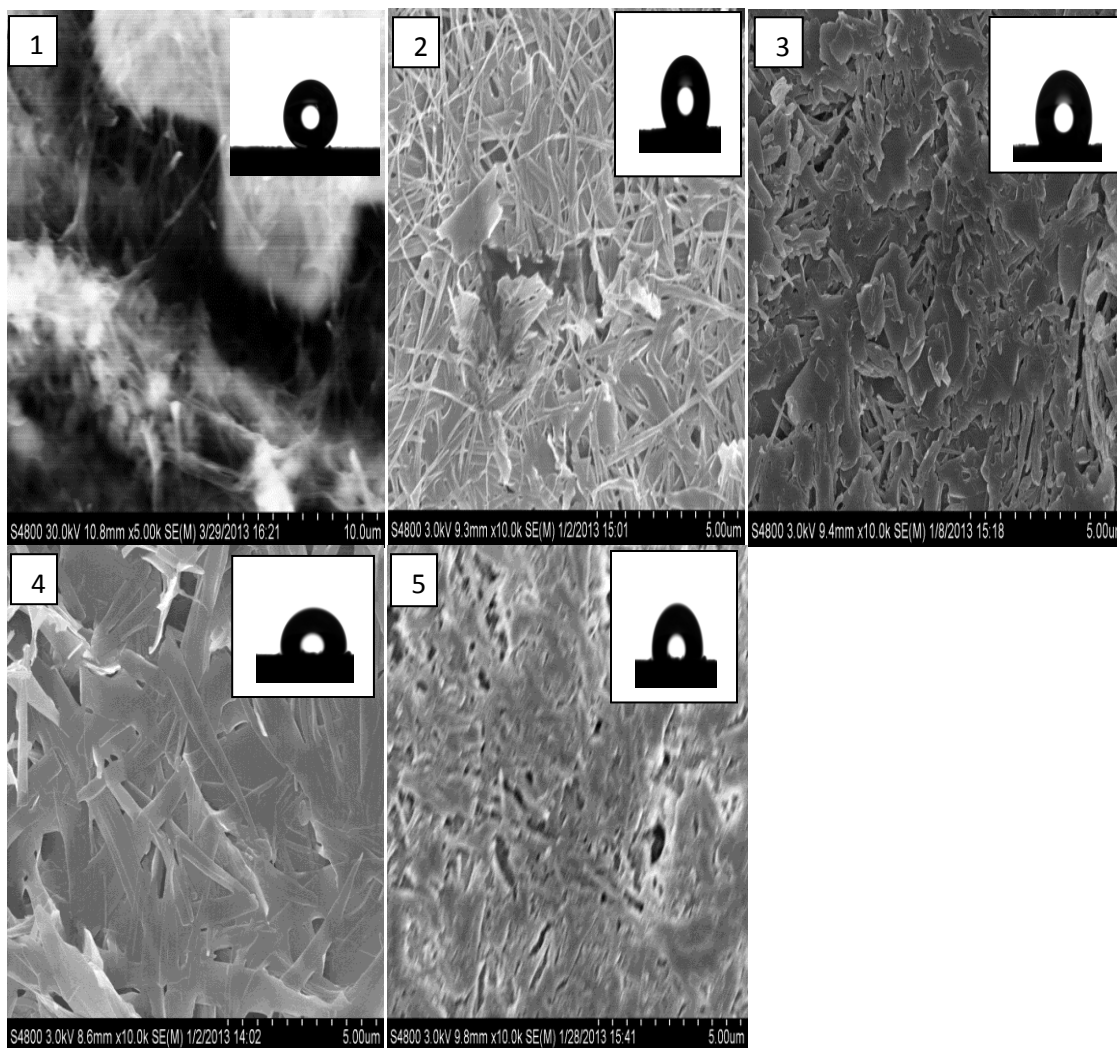


Figure 81: Scanning electron microscopic images of C36000 after chemical oxidative surface modification in 0.005M STA at room temp. 1, 2, 3, 4, 5- C36000 for 1-5 days in 0.005M STA

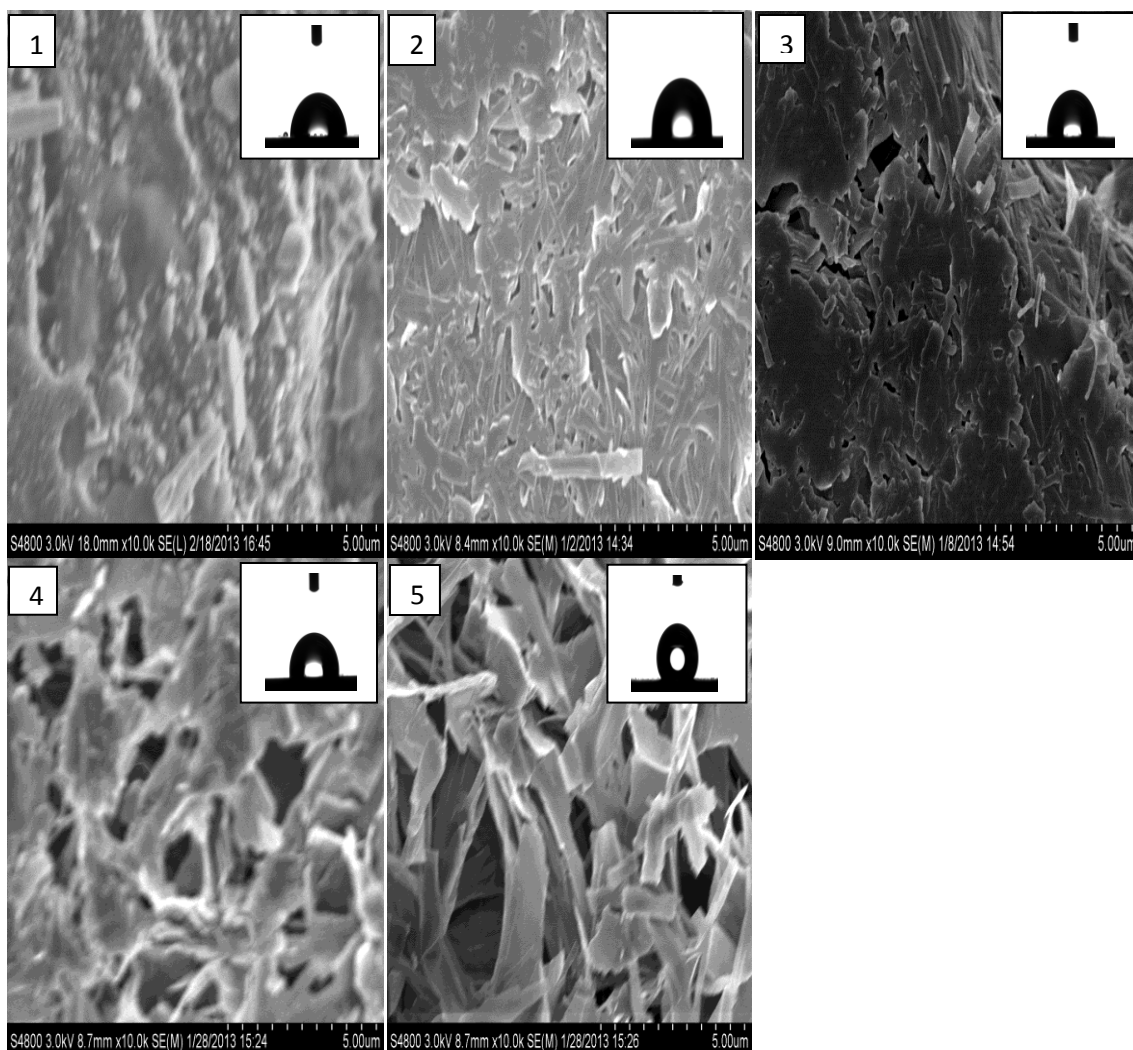


Figure 82: Scanning electron microscopic images of C84400 after chemical oxidative surface modification in 0.005M STA at room temp. 1, 2, 3, 4, 5- C84400 for 1-5 days in 0.005M STA

The treated surfaces showed a lot of diverse features. As can be seen from the SEM images evaluated for the various copper alloys depending on the time the samples were exposed to the 0.005M STA solutions.

In C36000 copper alloy, [1, 2, 3, 4, 5 and 6 in figure 81], the size of the surface features observed ranged from 110 ± 40 nanometers after 1 day of chemical oxidative process in 0.005M STA to 250 ± 80 nanometer after 5 days of the process, with a maximum size of 530 ± 28 nanometers observed at 4 days of the process. In C84400 copper alloy samples

[1, 2, 3, 4 and 5 in figure 82], the surface morphology changed with the time the samples were chemically oxidized. The sizes of the features increased with time of treatment of the samples. The observed sizes of the microstructure of the surface features ranged from 360 ± 80 nanometers for the sample, after the first day of treatment, to 780 ± 30 nanometers observed on the sample that was treated for 5 days.

9.3.1 [b] Surface morphologies of samples treated in 0.005M ARA at 30°C and 40 C:

The observed surface morphologies on the C36000 and C84400 surfaces after their direct chemical oxidation on 0.005M STA at 30 °C and 40 °C are shown in figures 83 and 84 as well as figures 85 and 86 respectively.

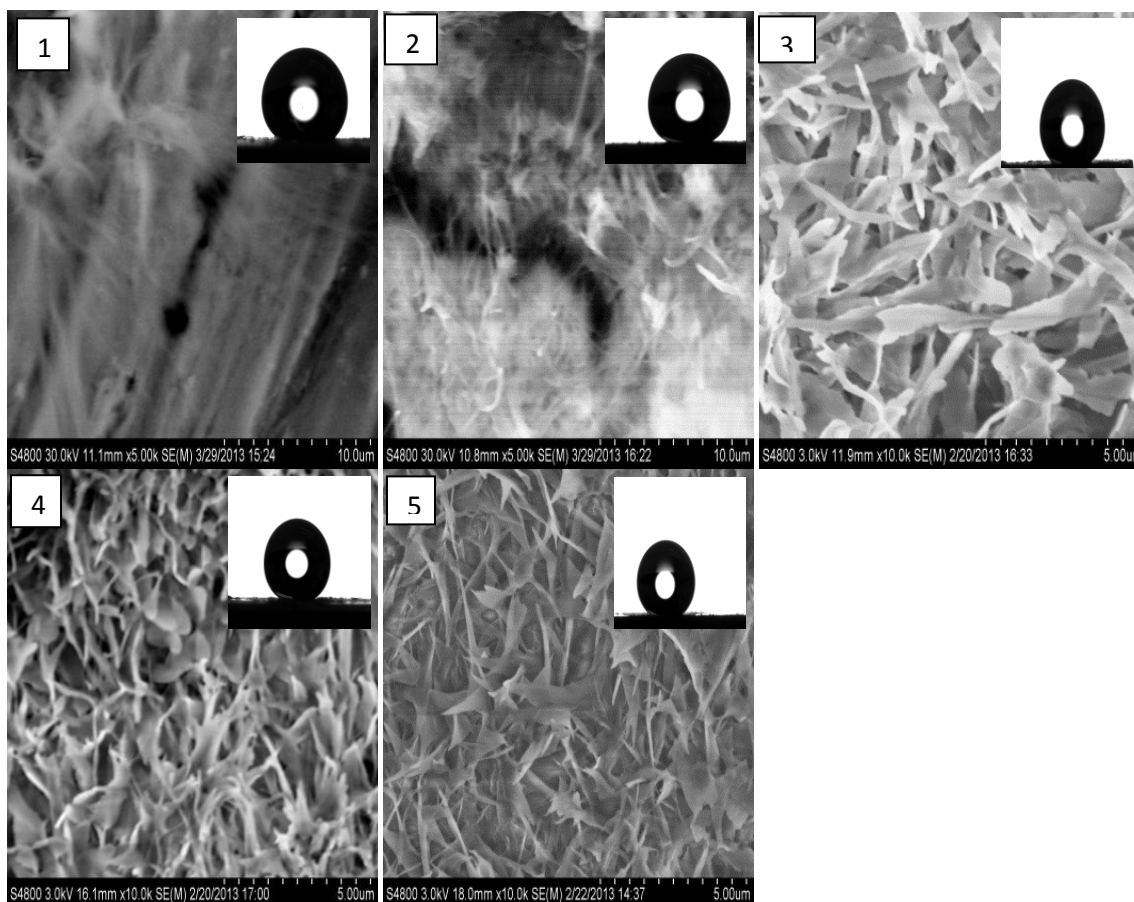


Figure 83: Scanning electron microscopic images of C36000 after chemical oxidative surface modification in 0.005M ARA at 30 °C. 1, 2, 3, 4, 5- C36000 for 1-5 days in 0.005M ARA

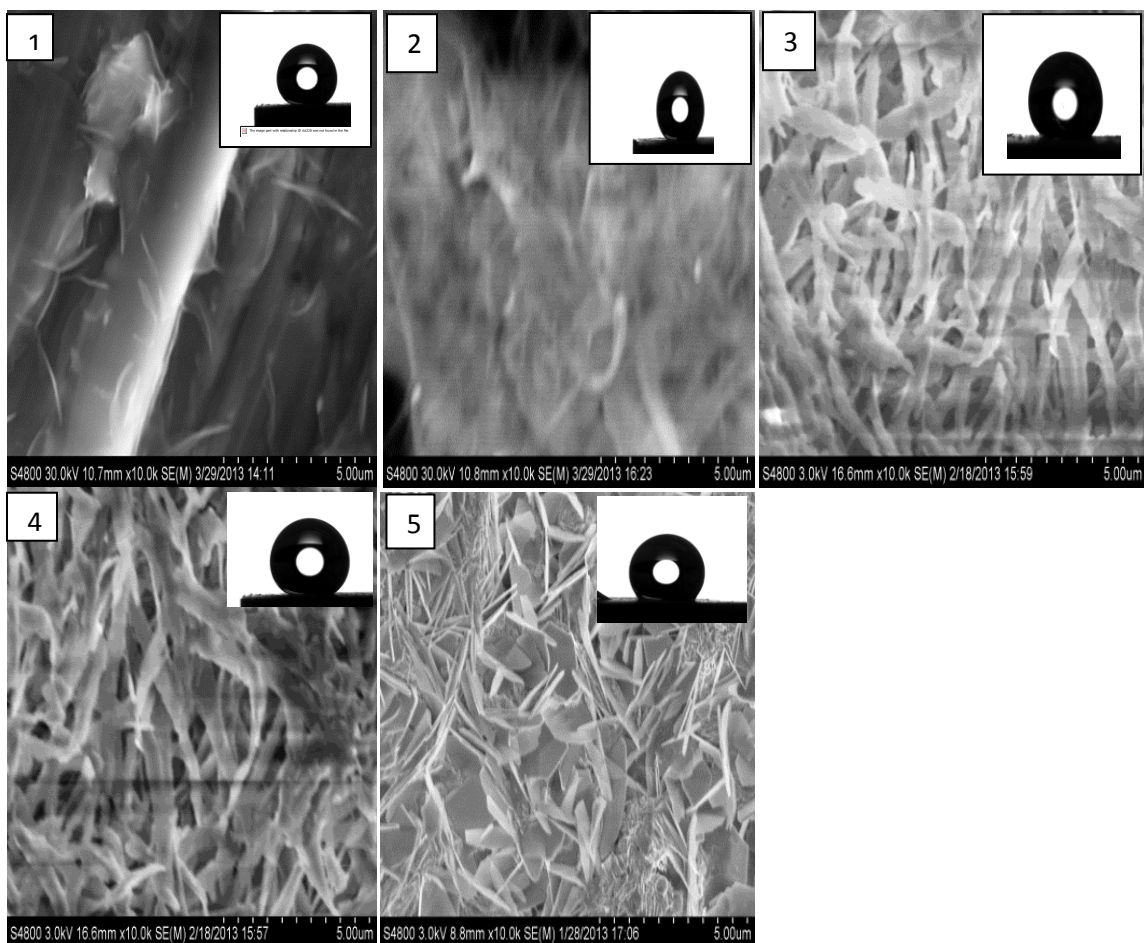


Figure 84: Scanning electron microscopic images of C84400 after chemical oxidative surface modification in 0.005M ARA at 30 °C. 1, 2, 3, 4, 5- C84400 for 1-5 days in 0.005M ARA

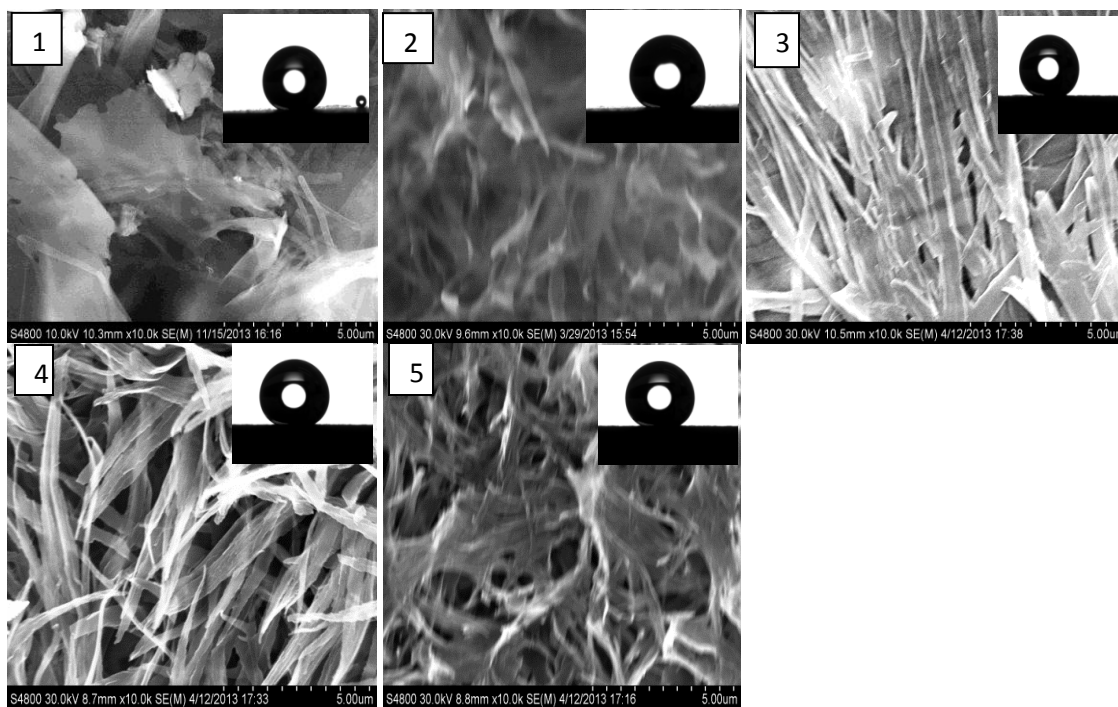


Figure 85: Scanning electron microscopic images of C36000 after chemical oxidative surface modification in 0.005M ARA AT 40 °C. 1, 2, 3, 4, 5- C36000 for 1-5 days in 0.005MARA

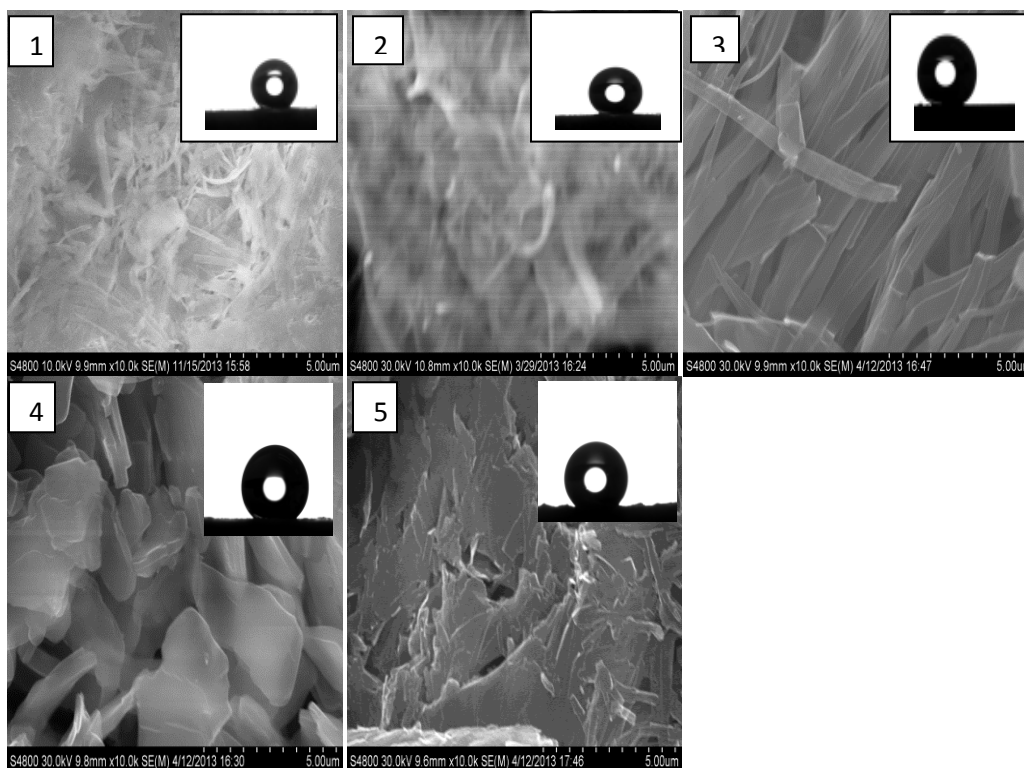


Figure 86: Scanning electron microscopic images of C84400 after chemical oxidative surface modification in 0.005M ARA AT 40 °C. 1, 2, 3, 4, 5- C84400 after 1-5 days in 0.005M ARA.

The SEM images reveal a lot of details on the nature of the surfaces formed after the chemical oxidative processes in arachidic acids at these temperatures. Most of the surfaces features ranged from very thin nanobelts to larger nanobelts and sometimes coarsened surface features at extensive times of the oxidation.

9.4 Energy Dispersive X-ray analyses of the chemically oxidized surfaces:

The chemical compositions of the surface products due to the nanostructures formed after the oxidative chemical treatment were evaluated using energy dispersive X-ray analyses (EDX). From the elemental analyses of these structures on the copper alloys treated with 0.005 M STA and 0.005M ARA, considerable percentage weight of carbon (%C) and oxygen (%O) were found on the surfaces as shown in figure 87.

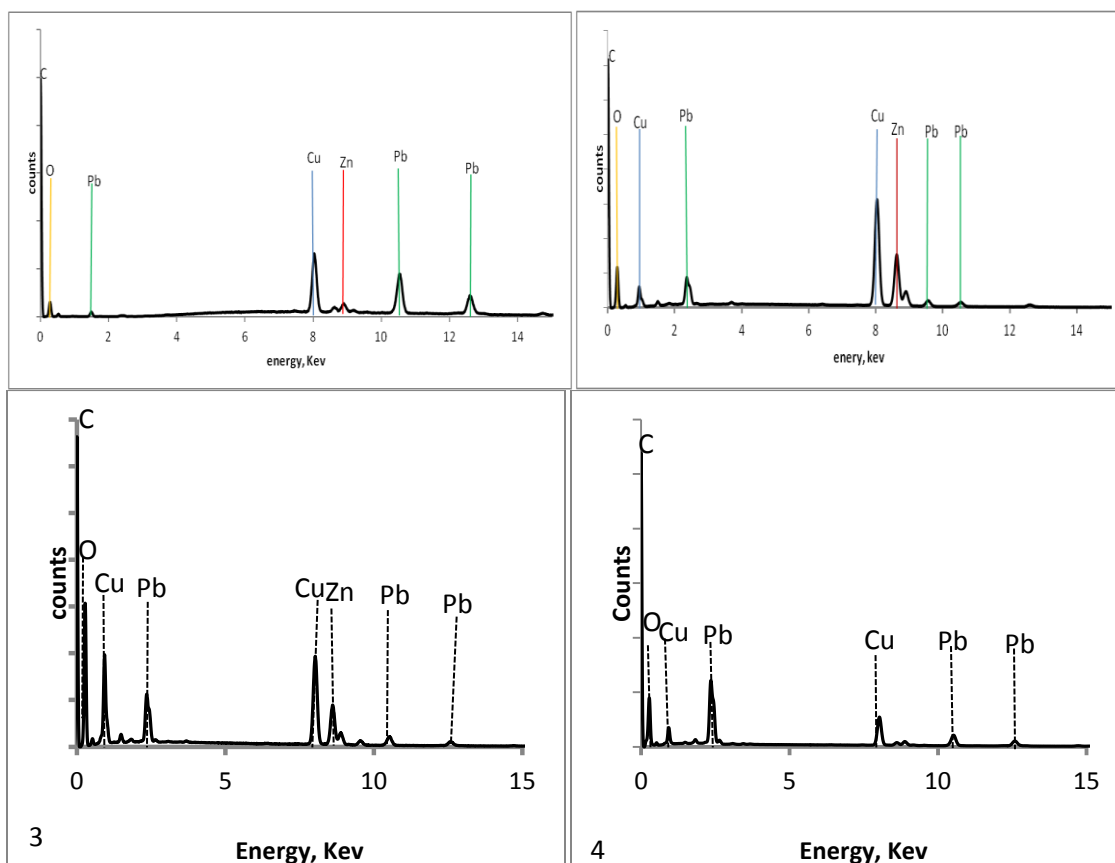


Figure 87: Elemental composition of surfaces of (1) C36000 copper alloy oxidized in 0.005M STA for 5 days (2) C84400 copper alloy chemically oxidized in 0.005M STA for 5 days (3) C36000 copper alloy oxidized in 0.005M ARA for 5 days (4) C84400 copper alloy chemically oxidized in 0.005M STA for 5 days (3) C36000 copper alloy oxidized in 0.005M ARA for 5 days.

The localized chemical composition of the surfaces showed that these surfaces were composed of carbon and oxygen as well as copper, zinc and lead based on the alloy composition. The presence of carbon on the surfaces implies a change in the chemical composition of the surfaces due to the oxidization reaction. The elemental maps of the surfaces showed that carbon and oxygen were distributed all over the surfaces of the oxidized copper alloys in the form of clusters with zinc as the predominant element prevailing around and within such clusters as shown in Appendix C.

9.5 X-ray diffraction analysis of chemically oxidized C36000 treated with 0.005M STA and ARA.

The surfaces of the chemically oxidized samples as well as the unoxidized C36000 and C84400 copper alloys were characterized by X-ray diffraction and examined at low and high 2θ angles as stated in figure 88. The X-ray diffraction was carried out between 3° and 60° for 2θ .

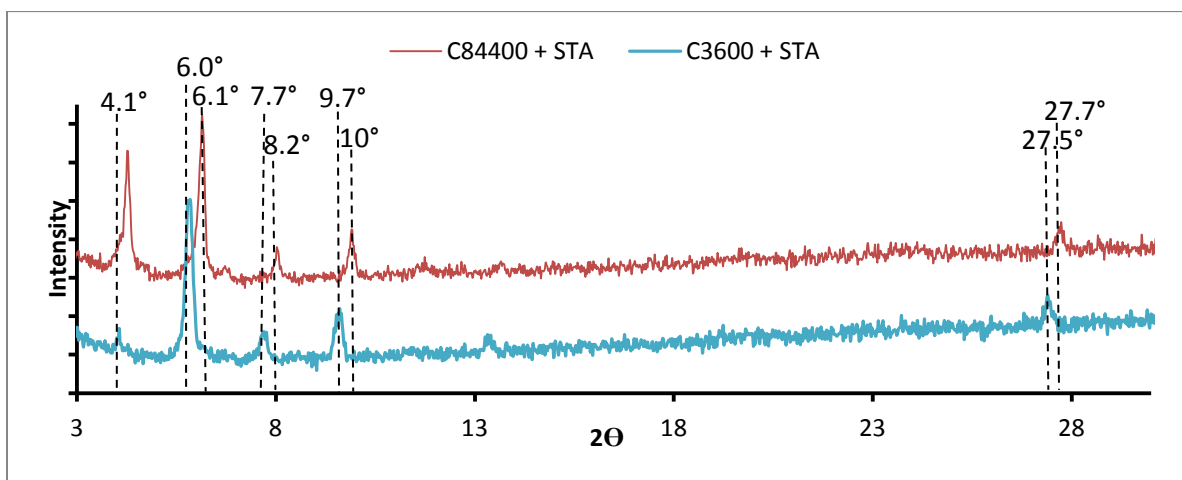


Figure 88: X-ray diffraction pattern of C36000 and C84400 copper alloys after treatment in 0.005M STA for 5 days.

The diffraction pattern obtained for the chemically oxidized surfaces of C36000 showed diffraction peaks occurring at 4.1° , 6.0° , 7.7° and 9.7° respectively. In the case of

C84400 samples that were chemically oxidized in STA, the low 2θ angle diffraction analysis between 3° and 18° showed diffraction peaks at 4.1° , 6.1° , 8.2° , 10° and 27.7° . The 2θ values of the diffraction peaks from the surfaces of the C36000 and C84400 copper alloys confirm the formation of zinc stearate. These diffraction peaks are similar to those observed for the long-spacing diffraction peaks for zinc stearate in PDF card number 00-55-1618.

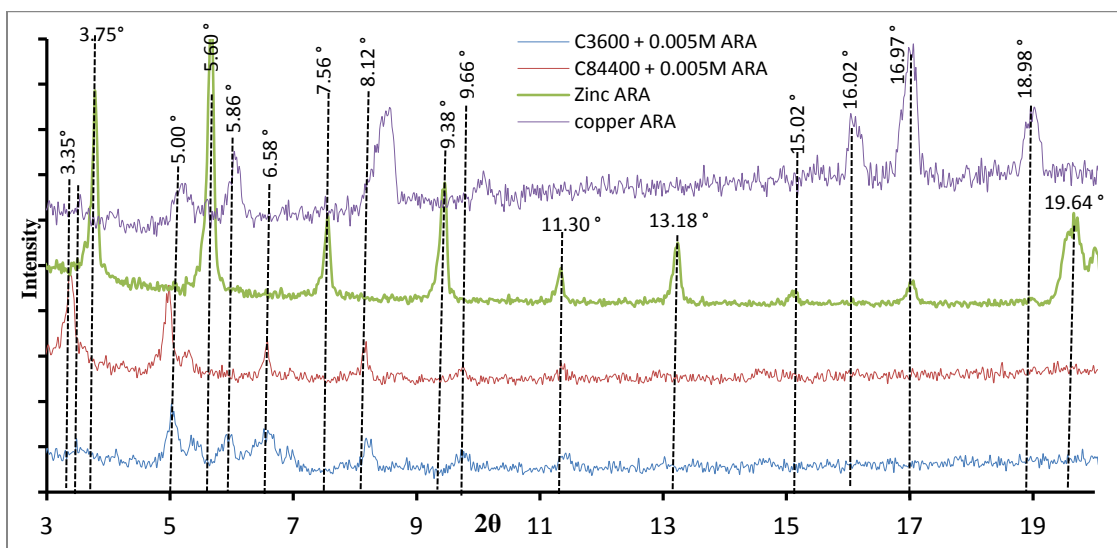


Figure 89: X-ray diffraction pattern of C36000 and C84400 copper alloys after treatment in 0.005M ARA for 5 days at 40°C .

These diffraction peaks for the C36000 copper alloys were observed at 2θ angles of 3.37° , 5.0° , 5.86° , 6.58° , 8.12° , 9.66° and 11.30° between 3° and 20° . Diffraction peaks of the C84400 copper alloys that were oxidized chemically at 40°C in 0.005M ARA were quite similar to those stated for the C36000 copper alloys chemically oxidized under the same conditions in the same conditions. The peaks for the X-ray diffraction were observed at 2θ angles of 3.35° , 5.0° , 6.58° , 8.12° , 9.66° , 11.30° between 2° and 20° .

Comparatively, the X-ray analyses of zinc and copper arachidate powders showed peaks at these low 2θ angles between 3° and 20° that were similar to those stated above for the C36000 and C84400 copper alloys stated above. This confirmed a mix of the zinc and copper arachidate on the sample surfaces as products of the chemical oxidation.

9.6 Contact angle of water on C36000 and C84400 copper alloys after chemical oxidation in different concentrations of STA and in ARA at different temperatures:

The contact angle behavior of water on these surfaces of the copper alloys as a function of the time, and concentration of the stearic acid and as well as at different temperatures in arachidic acid were studied. These are discussed as follow:

9.6 (a) Effect of concentration of stearic acid on the contact angle of water:

The effect of the change in the concentration of stearic acid on the contact angle of water on the surfaces of the C36000 and C84400 copper alloys were investigated in 0.005M STA, 0.010M STA and 0.015M STA. The contact angles measured on these surfaces are shown in Tables 28, 29 and 30.

Table 28: Contact angles of water on copper alloys immersed in 0.005M STA for different time duration

Time (hrs)	0.005M STA			
	C36000		C84400	
	Θ_{AV}	STD	Θ_{AV}	STD
24	90.6	± 6.1	96.2	± 3.7
48	93.1	± 11.9	94.7	± 4.8
72	93.5	± 3.8	95.7	± 4.9
96	88.5	± 1.5	85.6	± 5.2
120	95.4	± 3.3	100.8	± 4.5

Table 29: Contact angles of water on copper alloys immersed in 0.010M STA for different time duration

Time (hrs)	0.015M STA			
	C36000		C84400	
	Θ_{AV}	STD	Θ_{AV}	STD
24	107.2	± 4.9	85.0	± 11.1
48	111.9	± 2.4	95.7	± 4.2
72	116.6	± 7.7	84.9	± 3.9
96	115.7	± 3.9	96.4	± 1.9
120	109.0	± 3.0	121.9	± 5.2

Table 30: Contact angles of water on copper alloys immersed in 0.015M STA for different time duration

Time (hrs)	0.010M STA			
	C36000		C84400	
	Θ_{AV}	STD	Θ_{AV}	STD
24	96.9	± 7.0	109.1	± 11.2
48	85.8	± 5.9	95.7	± 2.5
72	122.2	± 1.0	99.3	± 5.0
96	114.3	± 6.6	109.5	± 6.4
120	113.7	± 5.9	109.9	± 11.0

Using the line of best fit method, as shown in figure 89 the change in the contact angles in these various concentrations showed that higher contact angles of water were obtained at higher stearic acid concentrations. The increase in the contact angles is attributed a higher extent of surface coverage by the zinc stearate formed at higher concentrations within the time of the process.

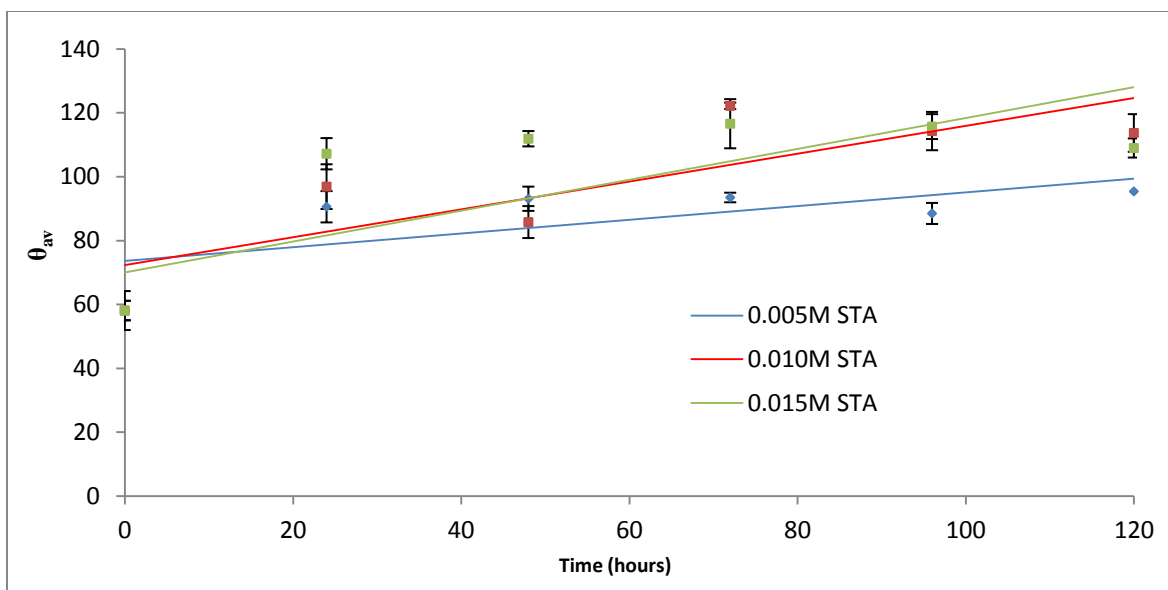


Figure 90: Plot showing the relationship of contact angle of water with time on C36000 treated in various concentrations of STA at room temperature

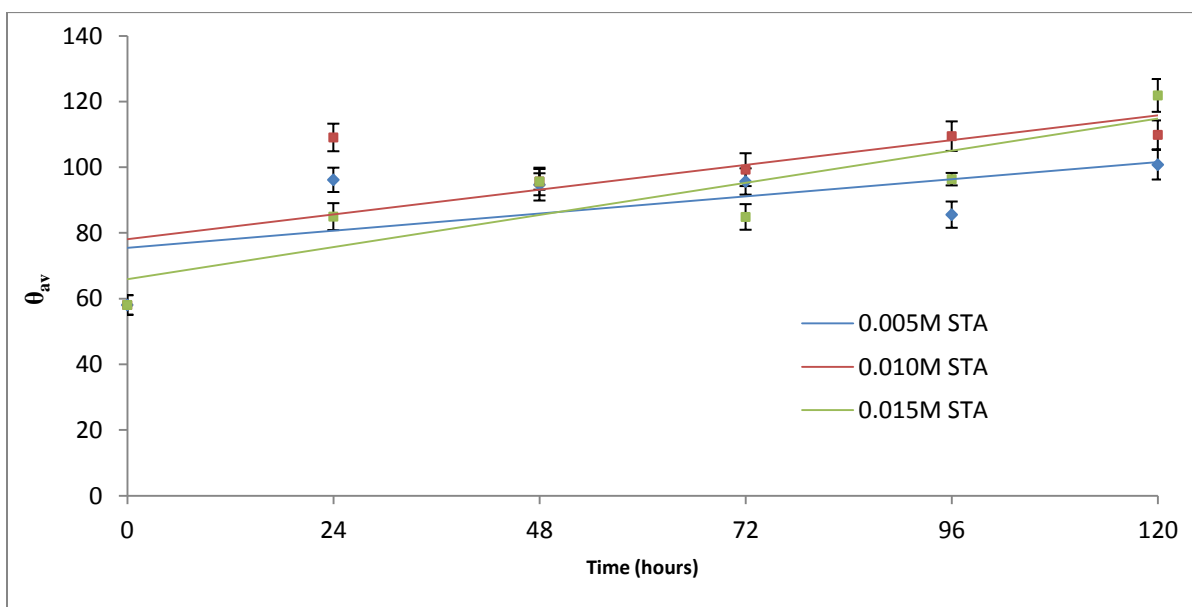


Figure 91: Plot showing the relationship of contact angle of water with time on C84400 treated in various concentrations of STA at room temperature.

Also, the contact angles increased with time used in the chemical oxidation of the copper alloys. This was understood through the analyses of the SEM images for the surface nanostructures of the zinc stearate that was formed on the C36000 and C84400 copper

alloy samples after chemical oxidative process in 0.005 STA at room temperature. The sizes of the zinc stearate surface features increased with increasing reaction time. This increase in the sizes dues to continuous surface deposition of the reaction products within the time of the process contributed to the surface coverage.

Also, the contact angle values obtained from a combination of the mechanical abrasion and chemical oxidation methods on the surfaces of the different copper alloys used in this work with the chemical oxidative process are stated in Table 31.

Table 31: Contact angles of water on abraded Copper alloys immersed in 0.015M STA for different time durations

Time (hrs)	0.015M STA/ abrasion with 50grit SiC paper					
	C36000			C84400		
	Θ_{AV}	STD	Θ_H	Θ_{AV}	STD	Θ_H
24	110.2	± 2.1	114.3	109.1	± 4.2	116.3
48	118.3	± 6.7	133.0	117.6	± 2.9	121.9
72	115.4	± 4.4	123.7	120.3	± 7.3	131.4
96	103.2	± 4.4	115.4	104.2	± 2.6	113.4
0	101.0	± 5.8	112.4	112.6	± 9.1	127.3

The combination of the mechanical abrasion with chemical oxidation in 0.015M STA did not generate significantly different contact angles of water when compared to the contact angles of water obtained from the direct oxidation of polished copper alloy samples.

9.6 (b) Effect of temperature on the contact angle of water chemically oxidized in 0.005M ARA:

For the effect of temperature, the process temperature was increased further to 30 °C to 40 °C for the chemical oxidation of the C36000 and C84400 copper alloys in 0.005M ARA. The values of the contact angles, surface roughness values of R_a as well as the

estimated sizes (D_s) of the zinc arachidate nano-features formed on the surfaces are stated in Tables 32 and 33.

Table 32: Contact angles of water on copper alloys immersed in 0.005M ARA for different time duration at 30 °C

Time (hrs)	0.005M ARA							
	C36000				C84400			
	Θ_{AV}	D_s (nm)	f_{sl}	R_a (μ m)	Θ_{AV}	D_s (nm)	f_{sl}	R_a (μ m)
24	152.3 $^{\circ}$ \pm 2.1	0.209 \pm 0.05	0.46	312.3	148.3 $^{\circ}$ \pm 2.6	0.170 \pm 0.03	0.59	205.13
48	155.4 $^{\circ}$ \pm 5.1	0.265 \pm 0.11	0.36	502.1	145.8 $^{\circ}$ \pm 4.3	0.201 \pm 0.08	0.69	510.24
72	153.0 $^{\circ}$ \pm 7.0	0.360 \pm 0.06	0.44	263.04	144.9 $^{\circ}$ \pm 7.8	0.471 \pm 0.06	0.71	1084
96	146.5 $^{\circ}$ \pm 8.3	0.464 \pm 0.04	0.66	232.24	141.4 $^{\circ}$ \pm 2.9	0.544 \pm 0.09	0.86	839.68
120	137.6 $^{\circ}$ \pm 6.5	0.571 \pm 0.07	-----	460.30	115.0 $^{\circ}$ \pm 3.4	0.566 \pm 0.05	-----	2251.6

Table 33: Contact angles of water on copper alloys immersed in 0.005M ARA for different time duration at 40 °C.

Time (hrs)	0.005M ARA							
	C36000				C84400			
	Θ_{AV}	D_s (nm)	f_{sl}	R_a	Θ_{AV}	D_s (nm)		R_a
24	150.0 $^{\circ}$ \pm 1.8 $^{\circ}$	0.275 \pm 0.05	0.54	911.1	149.4 $^{\circ}$ \pm 0.68 $^{\circ}$	0.178 \pm 0.04	0.61	959.54
48	151.8 $^{\circ}$ \pm 8.2 $^{\circ}$	0.322 \pm 0.04	0.47	213.	150.5 $^{\circ}$ \pm 3.6 $^{\circ}$	0.217 \pm 0.10	0.77	2892.2
72	149.6 $^{\circ}$ \pm 2.9 $^{\circ}$	0.504 \pm 0.07	0.57	235.	150.8 $^{\circ}$ \pm 7.9 $^{\circ}$	0.672 \pm 0.13	0.51	1872.4
96	150.3 $^{\circ}$ \pm 3.3 $^{\circ}$	0.479 \pm 0.03	0.53	1931	148.6 $^{\circ}$ \pm 2.8 $^{\circ}$	0.792 \pm 0.09	0.59	1383.3
120	146.3 $^{\circ}$ \pm 6.7 $^{\circ}$	0.686 \pm 0.08	0.67	2488.8	136.3 $^{\circ}$ \pm 3.2 $^{\circ}$	0.842 \pm 0.14	-----	1431.1

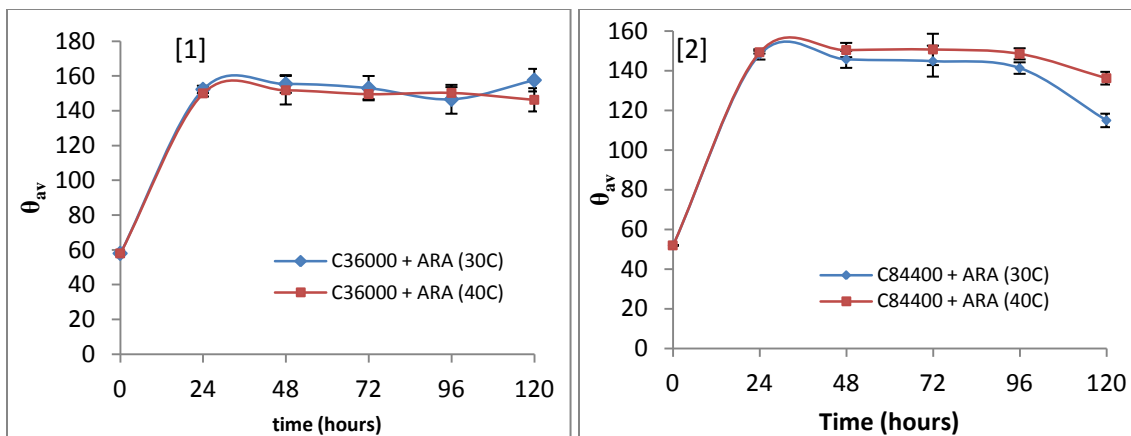


Figure 92: Plot showing the relationship of contact angle of water with time in various concentrations of STA [1] C36000 in 0.005M ARA at 30 °C and 40 °C [2] C84400 in 0.005M ARA at 30 °C and at 40 °C.

The thin nanobelts and other nano-sized surface features of zinc arachidate were formed on the surfaces of the copper alloys after the chemical oxidation in 0.005M ARA solution at 30 °C and 40 °C. A shift in the temperature from 30 °C to 40 °C caused a shift to higher values of the sizes of the zinc arachidate nanobelts that are formed and effective surface coverage of the samples. The growth of the zinc arachidates as nanobelts on the samples surfaces was enhanced by the temperature increase and the accumulation of the zinc arachidate increased with reaction time. Superhydrophobicity in water contact angles were achieved on these surfaces at both temperatures.

The variation of the estimated sizes of the nano-features wetted by the water drops formed at 30 °C and 40 °C are shown in figures 94.

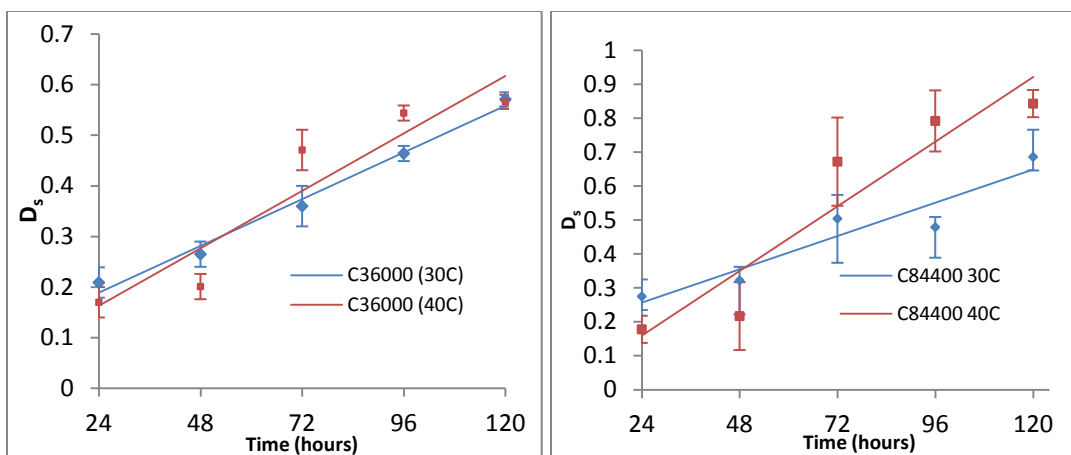


Figure 93: Plot of the variation of D_s with the time of chemical oxidation of copper alloys in 0.005M ARA.

The sizes of the nanobelts and other features on the surfaces after the chemical oxidative treatment in 0.005M ARA at 30 °C and 40 °C showed a linear relationship with the reaction time.

The copper alloys treated in 0.005M ARA at different temperatures achieved superhydrophobicity and are used in this case to properly explain the contact angle behavior of water on these surfaces with consideration to the chemical composition as well as the surface morphology. For this purpose, the contact angle of water on compacted, flat and smooth surface of zinc arachidate powder was measured. The surface showed hydrophobicity with water contact angle of $138.6^\circ \pm 0.5^\circ$. The method of preparing the zinc arachidate is stated in the Appendix A(b).

Generally, the surface energy is a surface property that affects wettability of surfaces. To this end, the chemistry of the surface of the copper alloys that were oxidized in the 0.005M ARA solutions at these increased temperatures affects the surface energy hence the contact angles of water. The surface energy of the zinc arachidate in this case is determined using the Fowkes method⁹³. This method is used to empirically estimate the

surface energy of the zinc arachidate based on the contact angle evaluated on its smooth and flat surface ($138.6^{\circ} \pm 0.5^{\circ} = \theta_f$).

The Fowkes method is based on the equation (31).

$$\gamma_s = \gamma_l^2 (1 + \cos\theta)^2 / 4\gamma_l^d \quad [31]$$

with water having a dominant polar component, γ_l^p as well as a dispersive component γ_l^d ($\gamma_l^p = 51.0 \text{ mJ/m}^2$ and $\gamma_l^d = 21.8 \text{ mJ/m}^2$). Using this relationship, the surface energy for the smooth surface of the zinc arachidate based on the water contact angle was evaluated as 1.13 mN/m .

Therefore, the formation of the zinc arachidate on the surface of the samples after the chemical oxidation of the samples at 30°C and 40°C resulted in a considerable reduction in the surface energy. It is this reduction in the surface energy that resulted in the shift of the water contact angles on the copper alloys from hydrophilicity, prior to the chemical oxidation process, to hydrophobicity.

The surface morphology of the zinc arachidate formed on the copper alloys samples after the chemical oxidation process equally contributed to the further increase in the contact angles of water, as seen in the superhydrophobicity noted on the surfaces. Based on the Cassie-Baxter model, a reduced surface area of contact with the water drop, f_{sl} , as well as a hierarchically rough surface will cause a hydrophobic surface to become superhydrophobic.

The growth of the zinc arachidate in the form of the nanobelts on the surfaces caused a reduction in the fractional surface area that is in contact with water. The sizes of the nanobelts formed on the chemical oxidation of the copper alloys at 30°C and 40°C are stated in tables 32 and 33. The sizes of the nanobelts and other features on the surface

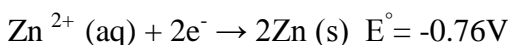
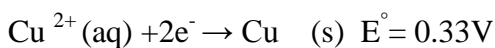
after the chemical oxidation at 30 °C in 0.005M ARA where in the range of 0.295 nm to 0.571 nm for the C36000 copper alloy and 0.170nm to 0.566 nm for the C84400 copper alloy respectively. For the chemical oxidation at 40 °C the sizes ranged from 0.275 nm to 0.686 nm for the C36000 copper alloy and 0.178nm to 0.842 nm for the C84400 copper alloy respectively. From the values of the estimated sizes of the zinc arachidate nanobelts, D_s ; the fractional surface area available for water wetting will be very small. As stated earlier, low values of f_{sl} is needed to sustain superhydrophobicity on these low energy surfaces. Using 138.6 ° for the smooth surface consisting of zinc arachidate, the f_{sl} values were evaluated using the Cassie-Baxter equation (4). The calculated values of the fractional surfaces of the nanobelts at the interface with the water drop were quite low. These values of the calculated f_{sl} are stated in tables 32 and 33.

The zinc arachidate nanobelts formed on the surfaces showed randomness in the growth direction and affected the roughness of the surfaces. The roughness parameter, R_a , which is the average surface roughness examined with the Atomic force microscope increased with increasing values of the D_s . This increase in the values of R_a is seen markedly in the C84400 copper alloys that were chemically oxidized in 0.005M ARA in 0.005M ARA at 30 °C and 40 °C.

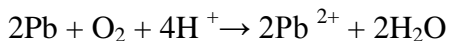
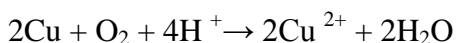
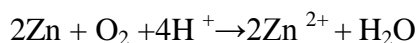
The increase in the reaction rate and accumulation of reaction products of the chemical oxidation process in the 0.005M ARA as seen in increasing values D_s is the reason for the increase R_a . However, at early times of the chemical oxidation process, the R_a values measured were close to that of the polished samples (0.1 microns). Therefore, at early stages of the chemical oxidative processes, the average surface roughness measured is

more reflective of the polished surface of the samples than for coating from the oxidation products.

The relative ease of formation of the zinc arachidate nano-size surface features on oxidation of these copper alloys depends on the oxidation potential of these alloying elements in the different copper alloy samples. Zinc is expected to oxidize relatively more quickly to the Zn^{2+} ions compared to Cu and Pb, which are all elements that are found in the C36000 and C84400 copper alloy samples. This oxidation is spontaneous resulting in the formation of Zn^{2+} , Pb^{2+} and Cu^{2+} ions. This follows simple electrochemical half-cell reactions described as follows:



Oxygen present in the solution is also reduced by the alloying elements in the samples based on these reactions:



The zinc ions substitute for the hydrogen atom in the carboxyl group in the stearic acid and arachidic acids, providing an ionic portion for the molecule which sticks to the samples' surfaces. The introduction of these different hierarchical structures such as the nanobelts of various dimensions and their alteration through process parameters such as time and reaction temperature all affected the contact angles.

Such an increase in the contact angle into the superhydrophobic range is therefore due to the combination of the low surface energy due to the zinc arachidate chemistry of the surface and the hierarchical rough surfaces as well as a low f_{sl} induced by the nanobelts and other nano-sized features formed on the surfaces.

CHAPTER TEN

CONCLUSION

The wetting properties of water and oil on surfaces of the C36000 and C84400 copper alloys were effectively altered using mechanical abrasion, thermal oxidation, chemical oxidation and a combination of these methods.

The following conclusions are drawn from these various experimental approaches:

1. Mechanical abrasion of the C36000 and C84400 copper alloys: The mechanical abrasion of the C36000 and C84400 copper alloys caused an abrupt increase of the contact angles for the oil underwater system. This change in the oil contact angle in the underwater system was dependent on the surface roughness, R_a as a result of the mechanical abrasion. This was consistent with a transition in the wetting regimes, from the Wenzel to the Cassie-Baxter state. Such wetting transitions are known for superhydrophobic surfaces, and this represents the first instance of this transition observed in underwater system for oil. The underwater transition phenomenon did not depend on the applied force used during the mechanical abrasion process. The underwater contact angle of oil was not influenced by the variation in the applied force with time.

2. Wetting behavior of thermally oxidized C36000 and C84400 copper alloys: The thermal oxidation of C36000 copper alloys resulted in the growth of convoluted oxide layers of varying thicknesses. XRD analyses of the oxidized surfaces confirmed the presence of ZnO and PbO. Nanowires grew on the oxide layers after thermal oxidation in the different N_2 - O_2 gas mixtures. EDX spot analyses of the nanowires confirmed them to be composed of ZnO. The ZnO nanowires affected the fractional surface area available

for wetting by water and oil drops. The calculated f_{so} were all low in values with the maximum being 0.52. The combination of the change in the f_{so} , the oxide layer thickness and the surface roughness caused high water contact angles, which reached a maximum of 142 °. These same factors affected the underwater oil contact angles, resulting in oleophobicity. The oleophobicity was however not observed on surfaces with contact angles above 130 ° as the Cassie-Baxter state could not be sustained on these surfaces that were too hydrophobic to trap water.

In the C84400 copper alloys, the thermal oxidation process involving varying amount of oxygen caused the growth of oxide layers following the parabolic law. The growth and the thickness of the oxide layer depended on the temperature, time, and oxygen weight per cent. The contact angle of oil was affected by surface tension factor and the porosity of the oxide layer thickness. In the C84400 samples oxidized at 550 °C, the increase in the contact angle of oil was induced by the surface tension.

As the oxide layers grew on thermal oxidation at 650 °C in thickness, the uneven packing of the grains caused the generation of pore spaces which caused porosity. Superoleophobicity with oil contact angle of 150 ° underwater was therefore achieved in samples oxidized in the N₂-5wt.-%O₂ for 3 hours at 650 °C. The increase in porosity as a function of the oxide layer thickness ensured a stable Cassie-Baxter state that caused the underwater superoleophobicity.

3. Combination of thermal oxidation of C36000 and C84400 copper alloys with chemical reaction with stearic acid and arachidic acid.

Thermal oxidation of the C36000 and C84400 copper alloy in air at 650 °C generated oxide grains in the nanosize range. The hydrophilic surface due to the oxide grains

changed on reaction with the low concentration stearic and arachidic acids. The reaction created a rough surface with hierarchical surface features. The chemical composition of the surfaces as evaluated through the FT-IR spectroscopic technique and X-ray diffraction analysis proved that reactions occurred between the oxidized surface layer composed of the oxide grains with of ZnO, CuO, and PbO. Zinc stearate was confirmed, through comparative XRD analysis with the diffraction pattern of zinc stearate powder, to be formed on the surfaces of C36000 copper alloy after reaction in 0.005M stearic acid. The strength of the oxide bonds was reflected in the ease of formation of the zinc stearate instead of lead stearate from the limited PbO found on the surface.

The FT-IR and XRD analyses showed that mixed stearates were formed on the oxidized surface layers of the C84400 copper alloys after reaction with stearic acid. Equally, mixed arachidates of zinc and lead as well as those of zinc, lead and copper were confirmed on the surfaces of the thermally oxidized samples of C36000 and C84400 copper alloys after the reaction with the low concentration arachidic acid.

The increased average surface roughness, low surface energy stearates and arachidates formed on the surfaces caused superhydrophobicity. However, the superhydrophobicity depended on the reaction time. Prolonged reaction time above 12 hours caused a drop in the contact angle of water. The reduction in the contact angle of water from the superhydrophobic range can be further investigated.

4. Chemical oxidation of C36000 and C84400 copper alloys in different concentrations of stearic and arachidic acids:

The chemical oxidative route showed that the nanobelts of zinc stearate and zinc arachidates formed due the chemical oxidation of the C36000 and C84400 copper alloys

affected the water contact angles. The chemical oxidation of the C36000 and C84400 copper alloys showed that the sizes of the nanobelts and other nano-sized features of zinc stearates formed on the sample surfaces depended on the reaction time and the temperature used for the process. The size of the surface features increased with the reaction time as the reaction product is accumulated. The effect of temperature on the surface features, formed on chemical oxidation with arachidic acid, resulted in bigger and longer nanobelts than those formed when the reaction was carried out at a lower temperature. The chemical nature of the surface products were confirmed through X-ray diffraction analysis. The surface was composed of zinc stearates.

A combination of mechanical abrasion with chemical oxidation did not alter the contact angle trend in any remarkable manner. The abraded surface were effectively covered by the reaction products when the samples were oxidized in 0.015M of stearic acid and the contact angle therefore the wetting behavior was not influenced by the initial average surface roughness induced by the abrasion.

In terms of recommendation for the development of self cleaning surfaces for the use in the water industry, the use of mechanical abrasion of the surfaces of the copper alloy will be effective in reducing surface fouling due to the transition of oil wetting behavior to higher contact angles that showed oleophobicity. This can serve as a simple and effective check against surface fouling by organic contaminants when these copper alloys are used in under water conditions. Beyond a simply surface roughening scheme, a combination of thermal oxidative and chemical reaction, where the oxides of different morphologies can be generated and converted to low energy stearates and arachidates of zinc, copper and lead, can be used on these to generate effective and stable self cleaning surfaces on these

copper alloys for use in the water industry. The advantage of such an approach lies in the cheapness of the process and reproducibility.

From this research we have established for the first time the occurrence of a wetting transition for the contact angle of oil under water. This oleophilic to oleophobic transition occurred as the surface roughness increased. The rougher surfaces of metallic surfaces such as the alloys that were studied in this case were oleophobic under water. Furthermore, the wetting behaviour of thermally oxidized surfaces of C36000 copper alloys has been shown to be dependent on the presence of ZnO nanowires and the thickness of the oxide layer on which the nanowires grow. Equally, by varying the thickness of the oxide layer, superoleophobicity underwater can be induced due to changes in the porosity of the oxide layer. Therefore, thicker oxide layers are suitable for underwater superoleophobic surfaces. Finally, the X-ray diffraction patterns of zinc, copper and lead arachidates have been generated. Prior to now, these diffraction patterns have not been listed in any database.

References

- [1] P. Forbes, "Self Cleaning Materials", *Scientific America*, vol. 299, no. 2, pp 67-75, 2005.
- [2] A. Lafuma, D. Quere, "Superhydrophobic states", *Nature Materials*, vol. 2, pp 457-460, 2003
- [3] C. R. Crick, P. I. Parkin, "Preparation and characterization of superhydrophobic surfaces". *Chemistry- A European Journal*, vol. 16, pp 3568-3588, 2010.
- [4] A. Pavel, S. Frankisek, J.M.J, Frechet. "Porous polymer coatings: a versatile approach to superhydrophobic surfaces", *Advanced Functional materials*, vol. 19, no. 12, pp 1993-1998, 2009.
- [5] P. Roach, N. J. Shirtcliffe, M. I. Newton, "Progress in superhydrophobic surface development", *Soft Matter*, vol. 4, pp 224-240, 2008.
- [6] M. Nosonovsky, B. Bhushan, *Multiscale Dissipative Mechanisms and Hierarchical Surfaces*. New York: Springer, (2008).
- [7] M. Ma, R. M. Hill, "Superhydrophobic surfaces", *Current Opinion in Colloid and Interface Science*, vol. 11, no. 4, pp 193-202, 2006.
- [8] N. J. Shirtcliffe, G. Mcttale, M. Newton, "The superhydrophobicity of polymer surfaces: recent developments", *Journal of Polymer Science, Part B: Polymer Physics*, vol. 49, no. 17, pp 1203-1217, 2011.
- [9] J. Kim, B. Lew, W.S Kim, "Facile fabrication of superhydrophobic nano-needle arrays via breath figures method" *Nanoscale Research Letters*, vol. 6, no. 1, pp 616-624, 2011.
- [10] L. Feng, S. Li, S. Li, J. Zhai, Y. Song, L. Jiang, "Superhydrophobic surface of aligned Polyacrylonitrile nanofibers" *Agewandte Chemie International edition*, vol. 41, no. 7, pp 1221-1223, 2002.
- [11] A. Nakajima, K. Hashimoto, T. Watanabe, "Recent studies on Superhydrophobic films", *Monatshefte fur chemie*, vol. 132, pp 31-41, 2001.
- [12] J. Bico, U. Thiele, D. Quere, "Wetting of textured surfaces" *Colloids surfaces, A. Physicochemical and Engineering Aspects*, vol. 206, pp 41-46, 2002.
- [13] M. Nosonovsky, B. Bushan, "Roughness-induced superhydrophobicity: a way to design non-adhesive surfaces", *Journal of Physics: Condensed Matter*, vol. 20, no. 22, pp 225009-, 2008.
- [14] J. R Davies, *ASM Specialty Handbook: Copper and Copper alloys*, ASM International, 2011.

- [15] W. Ozgonicz, E. Kalinowska-Ozgowicz, B. Graegorczyk, "The Microstructure and Mechanical properties of the alloy Cu₇₀Zn₃₀ after recrystallization annealing", *Journal of Achievement in materials and Manufacturing Engineering*, vol. 40, 79-82, 2010.
- [16] X. Zhang, F. Shi, J. Niu, Y. Jiang, W. Zhiqiang, "Superhydrophobic surfaces: from structural control to functional application", *Journal of Material Chemistry*, vol. 18, pp 621-633, 2008.
- [17] S. Palraj, G. Venkatachari, G. Subramanian, "Bio-fouling and corrosion of 60/40 brass in Mandapam waters", *Anti-corrosion Methods and Materials*, vol. 49, No. 3, pp 194-198, 2002.
- [18] S. Choopun, N. Hongsith, E. Wongrat, "Metal oxide nanowires by thermal oxidation reaction technique", *Nanowires*, INTECH: Croatia, pp 414-434, 2010.
- [19] Y. Xia, P. Yang, Y. Sun, Y. Wu, B. Mayers, B. Gates, Y. Yin, F. Kim, H. Yan, "One-dimensional nanostructures: synthesis, characterization and applications", *Advanced Materials*, vol. 15, no. 5, pp 353-389, 2003.
- [20] G. M Raynaud, R. A Rapp, "In situ observation of whiskers, pyramids and pits during the high temperature oxidation of metals", *Oxidation of Metals*, vol. 21, pp 89-102, 1984.
- [21] M. W Barsoum, *Fundamentals of Ceramics*, IOP Publishing: Philadelphia, 2003.
- [22] D. R. Gaskell, *Introduction to the Thermodynamics of Materials*, Taylor and Francis, 4th ed., 2003.
- [23] P. Kofstad, *High Temperature Oxidation of Metals*, John Wiley and Sons: New York, 1966.
- [24] B. H Tytell, I. Geld, H. S Preiser, *Theory of corrosion and protection of metals: The science of corrosion*, Macmillan Co.: NewYork, 1966.
- [25] H. Y, Dang, J. Wang, S.S, Fang, "The synthesis of metal oxide nanowires by directly heating metal samples in appropriate oxygen atmosphere", *Nanotechnology*, vol. 14, no. 7, pp 738-741, 2003.
- [26] Rosendo, A (2011, Febuary 11).Corrosion: Chemical Oxidation. Control Engineering. Retrieved from <http://www.controleng.com>.
- [27] B. J. Hansen, G. Lu, J. Chen, "Direct oxidation Groowth of CuO Nanowires from Copper-containing Substrate", *Journal of Nanomaterials*, vol. 2008, pp 1-7.
- [28] X. Jiang, T. Henricks, Y. Xia, "CuO nanowires can be synthesized by heating copper substrates in Air", *Nano Letters*, vol. 2, no. 12, pp 1333-1338, 2002.

- [29] M. Kaur, K. P. Muthe, S. K. Deshpande, S. Choudhury, J. B. Singh, N. Versa, S. K. Gupta, J. V. Yakhim, "Growth and branching of CuO nanowires by thermal oxidation of Copper", *Journal of Crystal Growth*, vol. 289, pp 670-675,
- [30] S. Ren, Y.F. Bai, J. Chen, S.Z. Deng, N.S. Xu, Q. B. Wu, S. Yang, "Catalyst-Free synthesis of ZnO nanowire arrays on Zinc substrate by low temperature thermal oxidation", *Materials Letters*, vol. 61, no. 3, pp 666-670, 2007.
- [31] M. R. Khankary, V. Vahed, A. Reyhani, "Synthesis and characterization of ZnO nanowires by thermal oxidation of Zn Thin Films at various Temperatures", *Molecules*, vol. 17, pp 5021-5029, 2012.
- [32] A. V. Maciel, W. D. Mussel, V. M. D. Pasa, "A Novel synthesis of Nanostructured ZnO via Thermal Oxidation of Zn Nanowires obtained by a Green Route" *Materials Science and Applications*, vol. 1, pp 279-284, 2010.
- [33] A. Sekar, S.H. Kim, A. Umar, Y.B. Hahn, "Catalyst-free synthesis of ZnO nanowires on Si by oxidation of Zn powders" *Journal of Crystal Growth*, vol. 277, no. 1-4, pp 471-478, 2005.
- [34] B.D. Yao, Y.F. Chan, N. Wang, "Formation of ZnO nanostructures by a simple way of thermal evaporation", *Applied Physics Letters*, vol. 81, no. 4, pp 757-759, 2002.
- [35] K. Saulig-Wenger, D. Cornu, F. Chassagneux, T. Epicier, P. Miele, "Direct synthesis of amorphous silicon dioxide nanowires and helical self-assembled nanostructures derived there from", *Journal of Materials Chemistry*, vol. 13, pp 3058-3061, 2003.
- [36] N. Verplanck, Y. Coffinier, V. Thorny, R. Boukheroub, "Wettability switching Techniques on superhydrophobic surfaces" *Nanoscale Research Letters*, vol. 2, pp 577-596, 2007.
- [37] S. Daotong, N. Songmee, S. Thongtem, P. Singjai, "Size-controlled growth of TiO₂ nanowires by oxidation of titanium substrates in the presence of ethanol vapor" *Scripta Materialia*, vol. 57, pp 567-570, 2007.
- [38] C. Yu, J. Park, "Thermal annealing synthesis of Titanium-dioxide nanowire-nanoparticle hetero-structures", *Journal of Solid State Chemistry*, vol. 183, no 10, pp 2268-2273, 2010.
- [39] A.M.B. Gonclaves, L. C. Campos, A.S. Ferlanto, R.G. Lacerda "On the growth and electrical characterization of CuO nanowires by thermal oxidation", *Journal of Applied Physics*, vol. 106, no. 3, pp 034303-034305.
- [40] N. Chopra, B. Hu, B.J. Hinds, "Selective growth and kinetic study of copper oxide nanowires from patterned thin-film multilayer structures", *Journal of Materials Research*, vol. 22, no 10, pp 2691-2699, 2007.

- [41] L. Yuan, Y. Wang, R. Mema, G. Zhou, "Driving force and growth mechanism for spontaneous oxide nanowire formation during the thermal oxidation of metals", *Acta Materialia*, vol. 59, no. 6, pp 2491-2500, 2011.
- [42] G. Zhou, J. C. Yang, "Temperature effect on the Cu₂O oxide morphology created by oxidation of Cu(001) as investigated by in situ UHV TEM", *Applied Surface Science*, vol. 210, pp 165-170, 2003.
- [43] L. Luo, Y. Kang, J.C. Yang, G. Zhou, "Influence of the surface morphology on the early stages of Cu oxidation", *Applied Surface Science*, vol. 259, pp 791-798, 2012.
- [44] Z. W. Li, W. Guo, R. J. Reeves, "Zinc Oxide films by thermal oxidation of Zinc thin films", *Surface and Coatings Technology*, vol. 198, no. 1-3, pp 319-323, 2005.
- [45] R. Hangsrud, "The Influence of water vapour on the oxidation of copper at intermediate Temperatures", *Journal of the Electrochemical Society*, vol. 149, no. 1, pp B14-B21, 2002.
- [46] J. E. Samad, J. A. Nychka, "Wettability of biomimetic thermally grown aluminum oxide coatings", *Bioinspiration and Biomimetics*, vol. 6, pp 1-9, 2010.
- [47] S. M Lee, K. S Kim, C. Pippel, S. Kim, J. H Kim, H. J Lee, "Facile Route Toward Mechanically stable Superhydrophobic Copper using Oxidation-Reduction induced morphology changes", *Journal of Physical Chemistry C*, vol. 116, no. 4, pp 2781 – 2790.
- [48] X. Liu, Y. Liang, F. Zhou, W. Liu, "Extreme wettability and turnable adhesion: biomimicking beyond nature", *Soft Matter*, vol. 8, pp 2070-2086, 2012.
- [49] L. Ling, L. Mingjie, C. Peipei, J. Ma, D. Han, L. Jiang, "Bio-Inspired Hierarchical Macromolecule- Nanoclay Hydrogels for Robust underwater superoleophobicity", *Advanced Materials*, vol. 22, no. 43, pp 4826-4830, 2010.
- [50] B. A Starkweather, R. M Counce, "An experimental study of the change in the contact angle of oil on a solid surface", *Industrial and Engineering Chemistry Research*, vol. 39, no. 2, pp 362-366, 2000.
- [51] Y.C Jung, B. Bhushan, "Wetting behaviour of water and oil Droplets in Three-phase interfaces for Hydrophobicity/philicity and Oleophobicity/philicity", *Langmuir*, vol.25, no. 24, pp 14165-14173.
- [52] P. G de Gennes, F Brochard-Wyrat, D. Quere Capillarity and wetting phenomena: Drops, Bubbles, Pearls, Waves, Springer: New York, 2003.
- [53] A. Lafuma, D. Quere, "Superhydrophobic states", *Nature Materials*, vol. 2, pp 457-460, 2003.

[54] L. Gao, T. J. McCarthy, "The 'Lotus Effect' Explained: Two Reasons why two length scales of Topography are important", *Langmuir*, vol. 22, no. 7, pp 2966-2967.

[55] Z. Yoshimitsu, A. Nakajima, T. Watanabe, K. Hashimoto, "Effect of surface structure on hydrophobicity and sliding behaviour of water droplets", *Langmuir*, vol. 18, no. 15, pp 5818-5822.

[56] Michael Nosonovsky, Bharat Bhushan "Superhydrophobic surfaces and emerging applications: Non-adhesion, energy, green engineering" *Current Opinion in Colloids and Interface Science*, vol. 14, no. 4, pp 270-280, 2009.

[57] M. Liu, S. Wang, A. Wei, Y. Song, L. Jiang, "Bioinspired Design of a superoleophobic and Low Adhesive water/solid Interface", *Advanced Materials*, vol. 21, no. 6, pp 665-669, 2009.

[58] Z. Guo, W. Liu, B. L. Su, "Fabrication of Co_3O_4 hierarchically Superhydrophobic boat-like hollow cages at the silicon surface", *Nanotechnology*, vol. 19, no. 14, pp 445608-445613, 2008.

[59] T.C Lee, W. J Wang, T. Y Han, "Preparation of a superhydrophobic ZnO Film on ITO Glass via Electrodeposition followed by oxidation. Effect of deposition time", *Journal of Adhesion Science and Technology*, vol. 23, no. 13, 13-14, 2009.

[60] S. Wang, L. Feng, L. Jiang, "One step solution-immersion process for the fabrication of stable bionic superhydrophobic surfaces", *Advanced Materials*, vol. 18, pp 767-, 2006.

[61] T. Liu, Y. Yin, S. Chen, X. Cheng, S. Cheng, "Superhydrophobic surfaces improve corrosion resistance of copper in seawater", *Electrochimica Acta*, vol. 52, no. 11, pp 3709-3713, 2007.

[62] M. Qu, B. Zhang, S. Song, L. Chen, J. Zhang, X. Cao, "Fabrication of superhydrophobic surfaces on engineering Materials by a solution-immersion process", *Advanced Functional Materials*, vol. 17, no. 4, pp 593-596, 2007.

[63] N. Saleema, D.K. Sarkar, R.W. Paynter, X.G. Chen, "Superhydrophobic Aluminium Alloy surfaces by a Novel one-step Process", *Applied Materials and Interfaces*, vol. 2, no. 9, pp 2500-2502.

[64] W. Kuan, Li. Chen, "The preparation of superhydrophobic surfaces of hierarchical silicon nanowire structures", *Nanotechnology*, vol. 20, pp 035605-1-035605-8, 2009.

[65] Z. Guo, W. Liu, B. Su, "A stable lotus-leaf-like water-repellent Copper", *Applied Physics Letters*, vol. 92, no. 6, pp 063104-1-063104-3, 2008.

[66] Q. Pan, H. Jin, H. Wang, "Fabrication of superhydrophobic surfaces on interconnected $\text{Cu}(\text{OH})_2$ nanowires via solution-immersion", *Nanotechnology*, vol. 18, no. 35, pp 3555605-355609, 2007.

- [67] L. Hao, Z. Chen, R. Wang, C. Guo, P. Zhang, S. Pang, "A non-aqueous electrodeposition process for fabrication of superhydrophobic surface with hierarchical micro/nano structure", *Applied Surface Science*, vol. 258, no. 22, pp 8970-8973, 2012.
- [68] X. D Zhao, H. M Fan, X. Y Liu, H. Pan, H. Y Xu, "Pattern-Dependent Tunable Adhesion of superhydrophobic MnO₂ Nanostructured film", *Langmuir*, vol. 27, no. 7, pp 3224-3228, 2011.
- [69] R. P. S Chakradhar, V. D Kumar, "Water-repellent coatings prepared by modification of ZnO nanoparticles", *Spectrochimica Acta part A: Molecular and Biomolecular Spectroscopy*, vol. 94, pp 352-356, 2012.
- [70] Y. Wan, Z. Wang, Y. Liu, C. Qi, J. Zheng, "Reducing Friction and Wear of a Zinc substrate by combining a stearic acid overcoat with a Nanostructured Zinc Oxide underlying Film: perspectives to Super-hydrophobicity", *Tribology Letters*, vol. 44, pp 327-333, 2011.
- [71] X. Hou, F. Zhou, B. Yu, W. Liu, "Superhydrophobic Zinc Oxide surface by differential etching and hydrophobic modification", *Materials Science and Engineering: A* vol. 452-453, pp 732-736, 2007.
- [72] Y. Wan, Y. Wang, Q. Zhang, Z. Wang, "Low-Friction performance of stearic acid modification of Nano-Textured ZnO coating", *Nanoscience and Nanotechnology Letters*, vol. 4, No. 9, pp 910-913, 2012.
- [73] Y. Wang, B. Li, C. Xu, "Fabrication of Superhydrophobic surface of hierarchical ZnO thin films by using stearic acid", *Superlattices and Microstructures*, vol. 51, no. 1, pp 128-134, 2012.
- [74] Y. Wang, W. Wang, L. Zhong, J. Wang, Q. Jian, X. Guo, "Super-hydrophobic surface on pure magnesium substrate by wet chemical method", *Applied Surface Science*, vol. 256, no. 38, pp 3837-3840, 2011.
- [75] Z. Wang, Q. Li, Z. She, F. Chen, L. Li, "Low-cost and Large-Scale fabrication method for an environmentally- friendly superhydrophobic coating on magnesium alloy", *Journal of Material Chemistry*, vol. 22, pp 4097-4105, 2012.
- [76] O. Çakır, "Review of Etchants for Copper and its Alloys in Wet Etching Processes", *Key Engineering Materials*, Vol. 364 – 366, pp 460-465, 2007.
- [77] C. H. Xu, Y. L. Liu, S. Q. Shi "Isothermal Oxidation Behavior of Cu-38at.%Zn Alloy at High Temperature" *High Temperature Material Processing*, vol. 30, pp 267-272, 2011.
- [78] C. H. Xu, Z. B. Zhu, H. F. Lui, C. Surya, S. Q. Shi, "The effect of Oxygen partial pressure on the growth of ZnO nanostructure on Cu_{0.62}Zn_{0.38} brass during thermal oxidation", *Superlattices and microstructures*, vol. 49, no 4, pp 408-415, 2011.

- [79] B. Birks, "Introduction to High Temperature Oxidation of Metals", 2nd edition, Cambridge University Press, Cambridge, 2006.
- [80] A. Lafuma, D. Quéré, "Superhydrophobic states", *Nature Materials*, vol. 2, pp 457 – 460, 2003.
- [81] G. Osmond, J. J. Boon, L. Puskar, J. Drennan, "Metal stearate distributions in modern artists' oil paints: surface and cross-sectional investigation of reference paint films using conventional and synchrotron infrared microspectroscopy", *Applied Spectroscopy*, vol. 66, no. 10, pp 1136-1144, 2012.
- [82] B. C. Smith, *Infrared Spectral Interpretation: A Systematic Approach*, CRC Press, Florida, USA, 1999.
- [83] M. C. Corbeil, L. Robinet, "X-ray powder diffraction data for selected metal soaps", *Powder Diffraction*, vol. 17, no. 1, pp 52-60, 2002.
- [84] R. D. Sun , A. Nakajima, A. Fujishima, T. Watanabe, K. Hashimoto, "Photoinduced Surface Wettability Conversion of ZnO and TiO₂ Thin Films", *Journal of Physical Chemistry B*, vol. 105, no. 10, pp 1984-1990, 2001.

Appendix A: Preparation of solutions and powders of zinc and copper arachidates

a. Preparation of Standard solutions of Stearic acid and Arachidic acid for reaction with C36000 and C84400 copper alloys

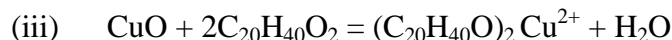
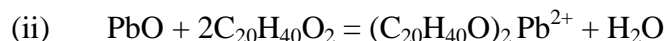
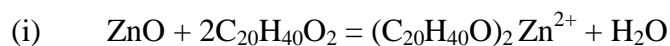
Molar mass of stearic acid: 284.48g/mol

Molar mass of arachidic acid: 312.53 g/mol

0.005M of stearic acid is prepared by dissolving 1.4g of stearic acid in 1000ml of ethanol solution. In the case of arachidic acid, 0.005M of ethanol solution of the acid was prepared by dissolving 1.6 g of arachidic acid in 1000ml of ethanol solution.

b. Preparation of zinc arachidate, lead arachidate and copper arachidate from oxide powders:

The equations for the reactions of ZnO, PbO and CuO with arachidic acid solution are:



The mole ratio of the reaction between the oxides and the acid is 1: 2 implying that 1 mole of the oxide will react with 2 moles of arachidic acid. 0.34 grams of ZnO is dispersed by stirring in 0.005M solution of arachidic acid made by dissolving 2.4 grams of the acid in ethanolic solution contained in a reactor. This is placed in the oven at 115 °C for 6 hours. The excess acid solution is decanted and the reaction product washed in ethanol solution and distilled water and dried in air. This process is repeated for PbO and CuO with 0.84 grams and 0.29 grams respectively with 2.4 grams of arachidic acid.

Appendix B: Chemical composition analyses by EDX

- a. Chemical composition and EDX analysis of the nano-features formed after the thermal oxidation of C84400 in N_2 -0.75wt.-% O_2 gas mixture for 1 and 2 hours.

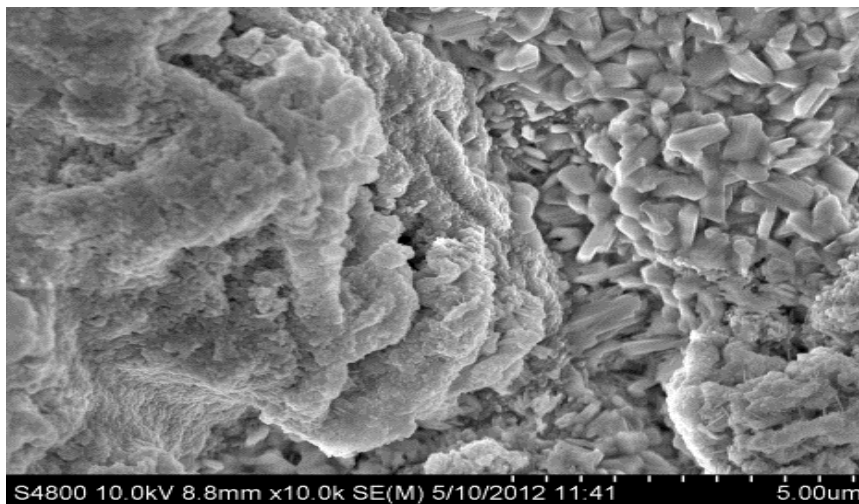


Figure AB (a) : SEM image for EDX sport analysis of oxide granules formed after 1 hour thermal oxidation in N_2 -0.75wt.-% O_2 gas mixture.

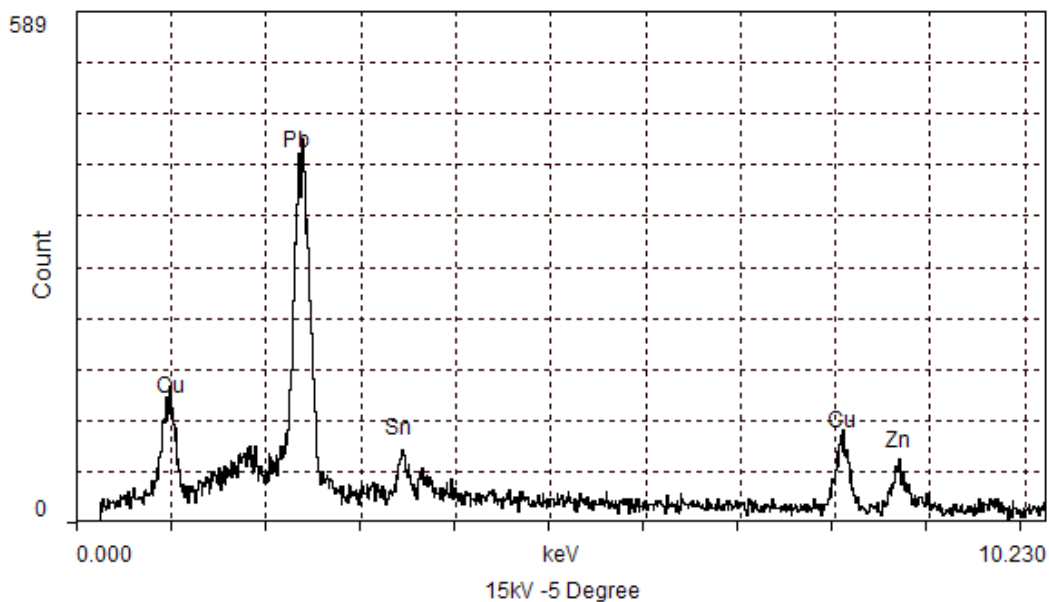


Figure AB (b): EDX plot of the chemical composition of the oxide granule formed after 1 hour thermal oxidation in N_2 -0.75wt.-% O_2 gas mixture.

The long grains formed after just 1 hour of thermal oxidation in N_2 -0.75wt.-% O_2 gas mixture showed the presence of a high quantity of lead and shown in the EDX plot above.

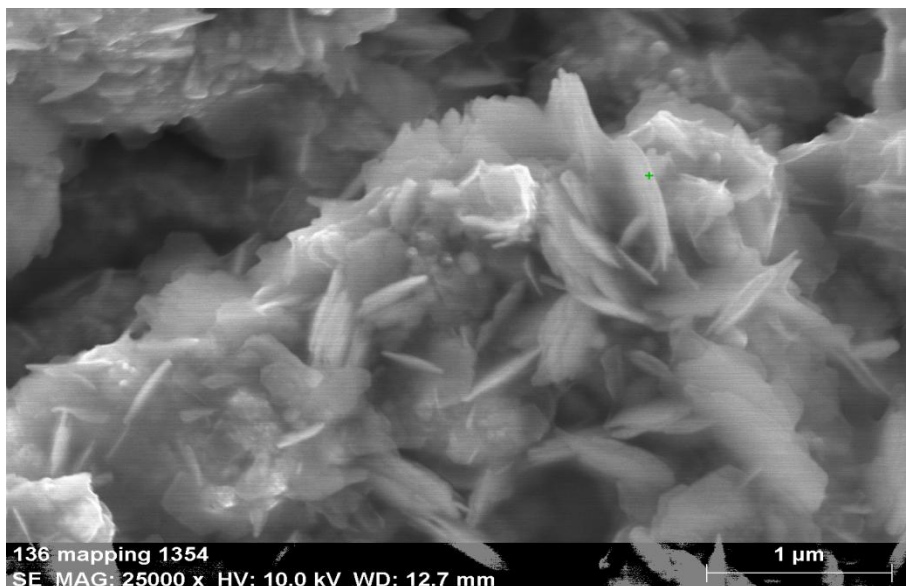


Figure AB (c) : SEM image for EDX sport analysis of oxide granules formed after 2 hour thermal oxidation in N_2 -0.75wt.-% O_2 gas mixture.

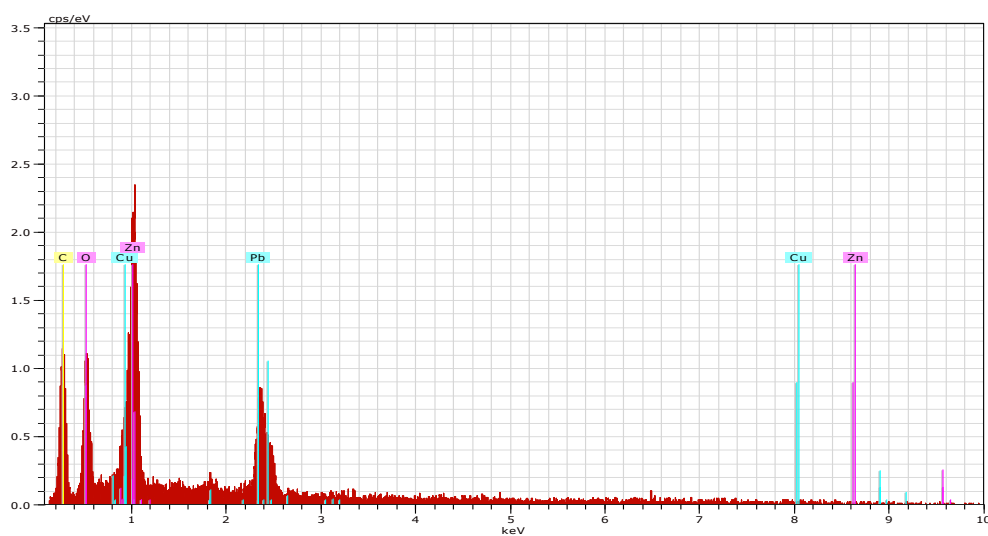


Figure AB (d): EDX plot of the chemical composition of the oxide granule formed after 2 hour thermal oxidation in N_2 -0.75wt.-% O_2 gas mixture.

The spot analysis of these flowery petals showed that they consisted of zinc, lead, copper and oxygen in the weight percentage of 34.75 wt.-%, 33.38 wt.-%, 6.40 wt.-% and 11.78 wt.-% respectively. To this end, these flowery oxide features can be regarded as formed from a merger of thin oxides of zinc, copper and lead.

Appendix C: Chemical composition analyses by elemental mapping

a. The elemental mapping of chemically oxidized C36000 and C84400 copper alloys

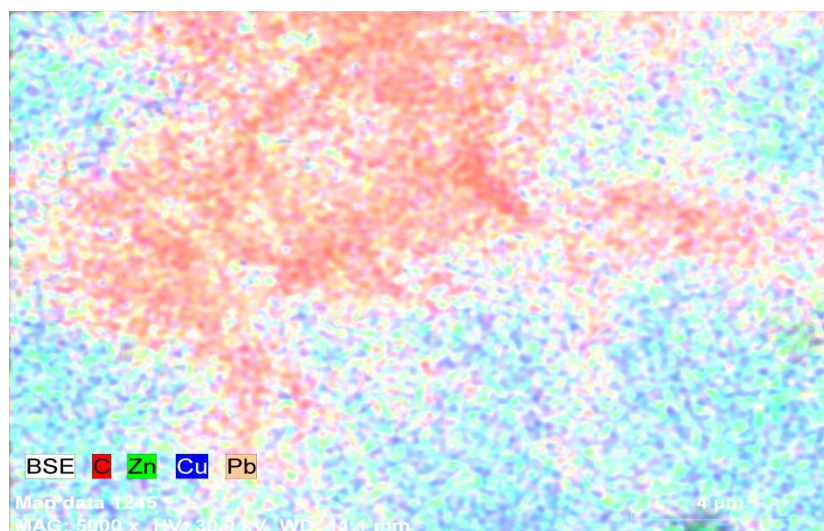


Figure AC (a): Elemental mapping of the distribution of the different elements after the chemical oxidation of C36000 copper alloy in 0.005M ARA at 40 °C.

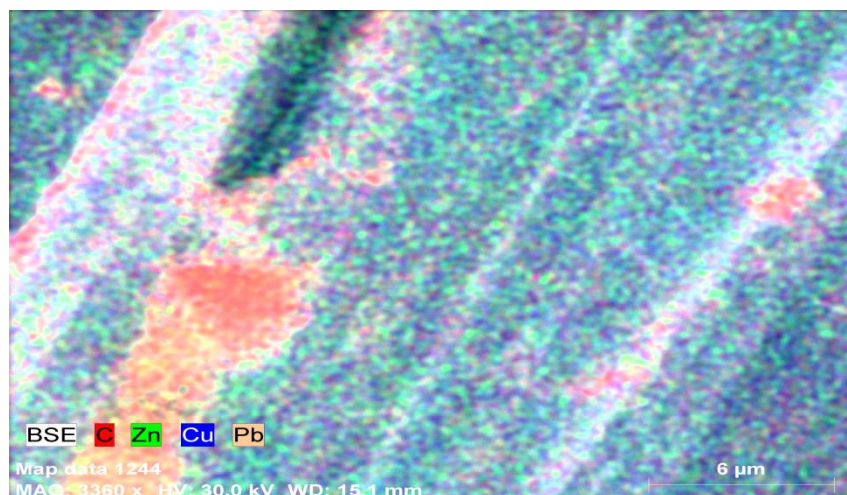


Figure AC(b): Elemental mapping of the distribution of the different elements after the chemical oxidation of C84400 copper alloy in 0.005M ARA at 40 °C.

The elemental map showed the wide presence of carbon on the surface on the surface of the oxidized samples.

Appendix D: Contact angle evaluation of smooth surfaces

a. Evaluation of the contact angle of water on a smooth compact surface of Zinc Arachidate:

The zinc arachidate that was formed, as stated in Appendix B, was place in a steel cap and pressed into a compact and smooth powder. The contact angle of water of the compound was achieved by placing drops of about 5ml of water on the surface of the compact and smooth zinc arachidate powder.

The contact angles were evaluated with the goniometer from which the average value was 138.6° was achieved.

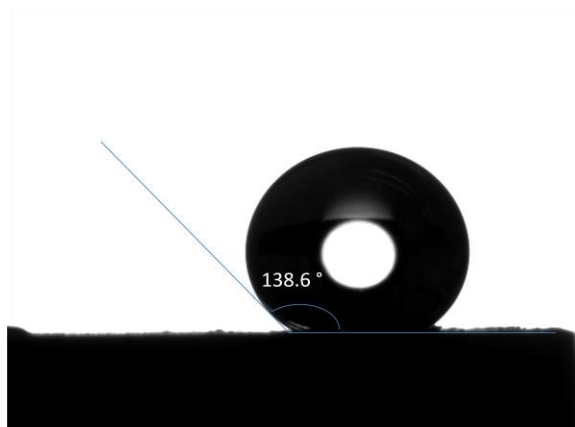


Figure AD (a) Contact angle of water on smooth surface of zinc arachidate powder.

CURRICULUM VITAE

Name: Aniedi E. Nyong

Place of birth: Uyo, Akwa Ibom State, Nigeria

Education:

University of Calabar, Nigeria- Bsc Chemistry (2000)

University of Ibadan, Nigeria- Post Graduate Dipl. In Engineering (2002)

University of Port Harcourt, Nigeria- Mineral Processing/Metallurgy (2006)

Awards:

Post Graduate Scholarship, Akwa Ibom State Government Foreign Scholarship Program (2007).

Chancellor's Award, University of Wisconsin-Milwaukee (2009).

Publications:

[1] M. Nosonovsky, V. Hejazi , A. E. Nyong , and P. K. Rohatgi, Metal Matrix Composites for Sustainable Lotus-Effect Surfaces, *Langmuir*, vol. 27 no. 23, pp 14419–14424, 2011.

[2] V. Hejazi, A. E. Nyong, P. K. Rohatgi, M. Nosonovsky, Wetting Transitions in Underwater Oleophobic Surface of Brass, *Advanced Materials*, Vol. 24, no. 44, pp 5963–5966, 2012.

[3] A. Nyong , P. Rohatgi, Underwater Superoleophobicity induced by the thickness of the thermally grown porous oxide layer on C84400 copper alloy, *Applied Sciences*, 3, 2013, (under review).

[4] A. Nyong, P. Rohatgi, Wetting of thermally oxidized C36000 copper alloy surfaces, *Journal of Engineering and Applied Sciences*, 2013 (under review)

